RECEPTIVITY OF HYPERSONIC BOUNDARY LAYER TO ACOUSTIC DISTURBANCES SCATTERED BY SURFACE ROUGHNESS

Alexander V. Fedorov

Moscow Institute of Physics and Technology
16 Gagarin Street, Zhukovki, Moscow Region, 140160
Russia

July 1999

19990903 073

AQF99-11-2177

REPORT DOCUMENTATION PAGE

Form Approved OMB No. 0704-0188

1. AGENCY USE ONLY (Leave blank)	2. REPORT DATE July 1999	3. REPORT TYPE AND DATES COVERED Final Report

4. TITLE AND SUBTITLE

Receptivity of Hypersonic Boundary Layer to Acoustic Disturbances Scattered by Surface Roughness

5. FUNDING NUMBERS

F61775-98-WE115

6. AUTHOR(S)

Dr. Alexander Fedorov

7. PERFORMING ORGANIZATION NAME(S) AND ADDRESS(ES)

Moscow Institute of Physics and Technology
16 Gagarin St
Zhukovsky 140160
Russia

8. PERFORMING ORGANIZATION REPORT NUMBER

N/A

9. SPONSORING/MONITORING AGENCY NAME(S) AND ADDRESS(ES)

EOARD
PSC 802 BOX 14
FPO 09499-0200

10. SPONSORING/MONITORING AGENCY REPORT NUMBER

SPC 98-4071

11. SUPPLEMENTARY NOTES

12a. DISTRIBUTION/AVAILABILITY STATEMENT

Approved for public release; distribution is unlimited.

12b. DISTRIBUTION CODE

A

13. ABSTRACT (Maximum 200 words)

This report results from a contract tasking Moscow Institute of Physics and Technology as follows: The contractor will perform theoretical analysis on the receptivity of hypersonic boundary-layer to acoustic disturbances as outlined in his proposal submitted in May '98.

14. SUBJECT TERMS

EOARD, Boundary Layer transition, Hypersonic Flow

15. NUMBER OF PAGES

81

16. PRICE CODE

N/A

17. SECURITY CLASSIFICATION OF REPORT UNCLASSIFIED	18. SECURITY CLASSIFICATION OF THIS PAGE UNCLASSIFIED	19. SECURITY CLASSIFICATION OF ABSTRACT UNCLASSIFIED	20. LIMITATION OF ABSTRACT UL

NSN 7540-01-280-5500

Standard Form 298 (Rev. 2-89)
Prescribed by ANSI Std. 239-18
298-102

Abstract

Theoretical study of hypersonic boundary-layer receptivity to acoustic waves scattered by a wall waviness (distributed roughness) and hump (local roughness) is performed using a combination of asymptotic and numerical techniques. Analytical results have been obtained for the normal-wave excitation by any combination of external disturbances (sound, vortical and entropy waves) and wall perturbations (roughness, suction/blowing, temperature irregularities *etc.*). It is shown that a strong excitation occurs in local regions where the flow disturbance, which is due to nonlinear interaction of external waves with wall-induced disturbances, is in resonance with normal waves. Analytical results are integrated into the computational module predicting the normal-wave amplitude generated in the resonance regions. Calculations of the second-mode excitation by acoustic waves of different frequency and incidence angle were conducted for two-dimensional disturbances in the boundary layer on a flat plate at Mach 6. Receptivity functions are presented for the case of both distributed and local roughness. The theoretical model can be used to predict initial amplitudes of unstable normal waves as well as estimate a tolerable roughness size associated with transition.

2

Table of contents

Acknowledgments

Nomenclature

Latin symbols

$\vec{A}_k$	eigenfunction vector (direct problem)
$\vec{B}_k$	eigenfunction vector (conjugate problem)
c	phase speed
$F = \omega^* v_e^* / U_e^{*2}$	frequency parameter
f	streamwise component of mass-flux disturbance
G	receptivity function
g	roughness shape-function
L	streamwise scale
M	Mach number
$\widetilde{p} = p^* / (\rho_e^* U_e^{*2})$	pressure disturbance
$p = p^* / P_e^* = \gamma M^2 \widetilde{p}$	pressure disturbance
q	receptivity factor
$R = \sqrt{U_e^* x^* / v_e^*}$	Reynolds number
t	time
T	mean flow temperature
U	mean flow streamwise velocity
V	mean flow vertical velocity
u, v, w	velocity disturbance
x, y, z	Cartesian coordinates
$x_1 = x^* / L^* = \varepsilon x$	slow variable

Greek symbols

α, β	wavevector components in x- and z-direction respectively
γ	specific heats ratio

$\varepsilon = \delta^* / L^*$	small parameter
Δ^*	boundary-layer thickness, $U^*(\Delta^*) = 0.99 U_e^*$
$\delta^* = \sqrt{\nu_e^* L^* / U_e^*}$	boundary layer scale
ν	kinematic viscosity
$\rho(\alpha, \beta)$	Fourier component of the shape-function $g(x', z')$
ω	angular frequency
Θ	incidence angle
θ	temperature disturbance
$\bar{\Psi}$	disturbance vector-function
$\vec{F}(x, y)$	disturbance amplitude vector-function

Subscripts

0	resonance point
a	acoustic
ad	adiabatic wall
b	branch point
dis	distributed
e	upper boundary-layer edge
loc	local
w	wall

Superscripts

bar	complex conjugate value
asterisk	dimensional value

Abbreviations

Im	imaginary part
Re	real part

List of figures

$$F = 6. \times 10^{-5}.$$

$$F = 6. \times 10^{-5}.$$

1. Introduction

This report summarizes the third phase of our theoretical studies on hypersonic boundary-layer receptivity. The first phase [1] addressed receptivity of two-dimensional boundary layer on a flat plate or sharp cone to entropy/vorticity disturbances. It was found that the first and second modes are synchronized with these freestream disturbances near lower neutral branch. Due to nonparallel effects entropy/vorticity waves are partially swallowed by the boundary layer and effectively generate the boundary-layer instability in the synchronism region. This mechanism can compete with the leading edge receptivity to acoustic disturbances [2, 3] in cases of "quiet" freestream and conical body configurations.

In the second phase [4], we analyzed receptivity to wall-induced disturbances such as vibrations, periodic suction-blowing through holes and slots and wall-temperature perturbations. This receptivity mechanism is associated with active (ascend) flights of a hypersonic vehicle, when propulsion system generates skin vibrations. The latter can propagate upstream and excite boundary-layer instabilities on the forebody surface. Receptivity to wall-induced disturbances is also important in developing active techniques providing dynamic control of initial instability amplitude. In these techniques, wall actuators generate disturbances in counter-phase with "natural" unstable waves in order to cancel the existing instability. The theoretical analysis [4] showed that hypersonic boundary layer is extremely receptive to wall vibrations of resonance frequency and wavelength. It was found that the receptivity function is maximal near the lower neutral branch of the second mode. This maximum is associated with the disturbance spectrum branch point at which characteristics of the first and second modes are identical. Near this point, both excitation and propagation of unstable normal waves are singular. With the help of asymptotic analysis we resolved singularities and evaluated the receptivity function in the branch-point vicinity. This study showed that a straightforward extrapolation of the receptivity and stability procedures from moderate supersonic to hypersonic regimes may lead to wrong predictions.

Another important mechanism of hypersonic boundary-layer receptivity is relevant to the interaction of external unsteady disturbances (acoustic, entropy and vorticity waves) with steady disturbances induced by spatial variations in surface boundary conditions (roughness/waviness, local heating/cooling, suction/blowing *etc.*). Early experimental [5] and theoretical [6-8] studies of this mechanism have been conducted in Russia for subsonic flows. Their results have been summarized in [9]. Asymptotic theory of the Tollmien-Schlichting wave excitation by acoustic wave interacting with surface irregularities has been developed in [10-12] and reviewed in [12-14]. In the last decade, detailed parametrical studies of this receptivity mechanism have been represented in [15-18]. Theoretical predictions are in a good agreement with the experiment [19] conducted on a flat plate in low-speed wind tunnel.

Receptivity of high-speed boundary layers (in the Mach number range from 1.15 to 4.5) to freestream disturbances scattering by the surface irregularities has been analyzed by Choudhari and Streett in [20]. They considered generation of inflectional and higher modes instability (the first and second modes) at Mach 4.5. Choudhari and Streett [20] reported that, although the Mach=4.5 boundary layer is nearly 6 times thicker than in the Mach=0 case, the instability amplitudes generated by a wall hump of fixed height are only marginally smaller than those at low speeds. This example indicates that receptivity of hypersonic boundary layer to acoustic plus roughness disturbances may play important role in the initial phase of transition.

In this report, we perform theoretical analysis of hypersonic boundary-layer receptivity to acoustic waves scattered by surface waviness (distributed excitation) or hump (local excitation) on a flat plate. In Section 2, we formulate the problem and show that main features of its analysis are similar to the case of receptivity to wall disturbances considered in [4]. In Section 3, we discuss the numerical results obtained for the second-mode excitation by fast and slow acoustic waves of various incidence angles in the boundary layer at Mach 6. In Section 4, we conclude the report and discuss future effort.

2. Problem formulation and analysis

In this chapter, we consider the excitation of boundary-layer normal waves by an acoustic wave which incidents on a flat plate and interacts with its wavy surface (distributed receptivity) or hump (local receptivity). In our analysis, we use the method developed in [4] for receptivity to wall-induced disturbances.

2.1 Distributed receptivity on wavy surface

We consider two-dimensional laminar boundary layer of a perfect gas on a hypersonic flat plate. The global streamwise length L^* is assumed to be much larger that the boundary layer thickness scale $\delta^* = \sqrt{v_e^* L^* / U_e^*}$; i.e. the ratio $\varepsilon = \delta^* / L^*$ is small and the Reynolds number $R_L = \sqrt{U_e^* L / v_e^*} = \varepsilon^{-1}$ is large. The longitudinal x^*, normal y^*, transversal z^* coordinates and time t^* are made nondimensional using δ^* and U_e^* as

$$(x, y, z) = (x^*, y^*, z^*) / \delta^*, \ t = t^* U_e^* / \delta^*.$$

Introducing the slow variable $x_1 = x^* / L^* = \varepsilon x$ we can specify the nondimensional mean-flow velocity components (U, V), temperature T, and pressure P as

$$U \equiv U^* / U_e^* = U(x_1, y), \ V \equiv V^* / U_e^* = \varepsilon V_0(x_1, y), \ T \equiv T^* / T_e^* = T(x_1, y), \qquad (2.1)$$
$$P \equiv P^* / (\rho_e^* U_e^{*2}) = P(x_1).$$

The wall waviness is represented in the form

$$y_w(x, y, z) = h \exp(i\alpha_w x + i\beta_w z) + (c.c), \qquad (2.2)$$

where $h = h^* / \delta^*$ is nondimensional amplitude, $\kappa_w = (\alpha_w, \beta_w)$ is wavenumber vector. It is assumed that the wavelength, $\lambda_w = 2\pi / \kappa_w = O(1)$, is of the order of boundary layer

thickness Δ^* ($U^* = 0.99U_e^*$ at $y^* = \Delta^*$). The waviness amplitude h^* is smaller than the viscous sublayer thickness; *i.e.* $h^* < \Delta^* R^{-1/2}$. In this case, the wavy wall generates small steady disturbances, which are governed by linearized Navier-Stokes equations [21].

An external acoustic wave of prescribed angular frequency $\omega = \omega^* \delta^* / U_e^*$ and wave-numbers $\alpha_a = \alpha_a^* U_e^* / \delta^*$, $\beta_a = \beta_a^* U_e^* / \delta^*$ incidents upon the plate as schematically shown in Fig. 1. Its physical quantities can be represented in a traveling-wave form. For example, the incident wave pressure is expressed as

$$p = p_{a,inc} \exp(i\alpha_a x + i\beta_a z + ik_{a,inc} y - i\omega t) + (c.c).$$

(2.3)

The vertical wave-number component, $k_{a,inc}$, is determined from the acoustic dispersion relation $k_{a,inc} = k_{a,inc}(\alpha_a, \omega, M)$, where M is freestream Mach number. The incident wave is refracted by the boundary layer, reflected by the wall and scattered by the wall waviness. Interacting with the waviness-induced disturbance the acoustic wave generates boundary-layer normal waves including the second mode. Our objective is to determine the receptivity function coupling characteristics of the incident acoustic wave and the wall waviness with the normal-wave amplitude.

Using the approach of [4] we represent the unsteady flow field as the vector function

$$\vec{\Psi}(x, y, t) = (u, \frac{\partial u}{\partial y}, v, \tilde{p}, \theta, \frac{\partial \theta}{\partial y}, w, \frac{\partial w}{\partial y})^T,$$

(2.4)

where u, v and w are velocity components; $\tilde{p} = p^* / (\rho_e^* U_e^{*2})$ is pressure and θ is temperature. In the following analysis we will also use the nondimensional pressure $p = p^* / P_e^* = \gamma M^2 \tilde{p}$. The vector-function (2.4) is expressed in the form

$$\vec{\Psi} = \vec{Q}(x_1, y) + h\vec{F}_w(x_1, y)\exp(i\alpha_w x + i\beta_w z) +$$

$$+ \varepsilon_a \vec{F}_a(x_1, y)\exp(i\alpha_a x + i\beta_a z - i\omega t) + \vec{F}(x, y, z)\exp(-i\omega t) + (c.c) \qquad (2.5)$$

Here the first term describes the boundary-layer mean flow on smooth surface; the second term corresponds to the stationary disturbance induced by the wall waviness. The third term corresponds to the acoustic disturbance, which is a combination of incident and reflected waves plus viscous components (vorticity and entropy waves) associated with the interaction of the acoustic component with the boundary-layer flow. Definition of the amplitude ε_a depends on the acoustic wave normalization. Hereafter we normalize the vector-function $\vec{F}_a(y)$ by the condition: (pressure amplitude p of the incident acoustic wave)=1 at the upper boundary-layer edge; then $\varepsilon_a = p^*_{a,inc} / P^*_e$.

The fourth term in Eq. (2.5) represent disturbances generated in the boundary layer due to nonlinear interaction between the acoustic wave and the waviness-induced perturbation. It is assumed that disturbance amplitudes are small, $\varepsilon_a \ll 1$ and $h \ll 1$, and the higher order terms such as $\varepsilon_a^2 h$, $\varepsilon_a h^2$ are neglected; *i.e.* the nonlinear interaction is considered to be weak.

Substituting (2.5) into Navier-Stokes equations we obtain the following problems, which can be written in the matrix-operator form.

For stationary disturbances induced by wall waviness:

$$H(y, \partial_y, x_1, \omega = 0, \alpha_w, \beta_w)\vec{F}_w = 0, \qquad (2.6a)$$

$$F_{w1}(x_1, 0) = -\frac{\partial U}{\partial y}(x_1, 0), \; F_{w3}(x_1, 0) = 0, \; F_{w5}(x_1, 0) = -\frac{\partial T}{\partial y}(x_1, 0), \; F_{w7}(x_1, 0) = 0, \; (2.6b)$$

$$|\vec{F}_w| < \infty, \; y \to \infty. \qquad (2.6c)$$

Boundary conditions (2.6b) have been obtained by the Taylor series expansion of the no-slip conditions, $u = v = w = 0$, and the wall-temperature condition, $\theta = T_w$, at $y = y_w$. In a similar way we can consider a wide class of inhomogeneous boundary conditions on the wall surface such as suction/blowing and heating/cooling. These variations do not affect the analysis.

For acoustic disturbances:

$$H(y, \partial_y, x_1, \omega, \alpha_a, \beta_a)\vec{F}_a = 0, \tag{2.7a}$$

$$F_{a1}(x_1, 0) = F_{a3}(x_1, 0) = F_{a5}(x_1, 0) = F_{a7}(x_1, 0) = 0, \tag{2.7b}$$

$$\text{(pressure amplitude of incident-wave component)} = 1, \ y \to \infty. \tag{2.7c}$$

For boundary-layer disturbances:

$$H(y, \partial_y, x_1, \varepsilon\partial_{x_1}, z, \partial_z, \omega)\vec{F} =$$

$$= h\varepsilon_a G(y, x_1, \vec{F}_w; \omega, \alpha_w, \beta_w, \alpha_a, \beta_a)\vec{F}_a \exp[i(\alpha_w + \alpha_a)x + i(\beta_w + \beta_a)z], \tag{2.8a}$$

$$F_1(x_1, 0) = F_3(x_1, 0) = F_5(x_1, 0) = F_7(x_1, 0) = 0, \tag{2.8b}$$

$$|\vec{F}| < \infty, \ y \to \infty. \tag{2.8c}$$

The right-hand side of Eq. (2.8a) describes nonlinear (quadratic) interaction of the wall-induced steady disturbance with the acoustic wave.

In Eqs. (2.6a) and (2.7a), the operator H can be expressed in the standard form

$$H = \frac{\partial}{\partial y} - H_0(y, x_1; R, \omega, \alpha, \beta), \tag{2.9}$$

where the matrix H_0 has dimension 8×8. Its elements depend on the mean-flow profiles (2.1), disturbance parameters α, β, ω and Reynolds number $R = \sqrt{U_e^* x^* / v_e^*}$. Explicit form of the matrix H_0 is given in Appendix.

16

We consider a partial solution of the problem (2.8a)-(2.8c) as a decomposition of the discrete modes $\vec{F}_k(x_1, y)$ with eigenvalues $\alpha_k(x_1, \beta, \omega)$

$$\vec{F} = h\varepsilon_a \sum_k [\vec{F}_{k0}(x_1, y) + \varepsilon\vec{F}_{k1}(x_1, y) + \cdots]\exp(i\varepsilon^{-1}S_k + i\beta z), \qquad (2.10a)$$

$$S_k = \int_{x_{1s}}^{x_1} \alpha_k(x_1, \omega, \beta)dx_1. \qquad (2.10b)$$

If the nonlinear term of Eq. (2.8a) *is not in resonance* with the normal waves; *i.e.* $\alpha_k(x_1, \omega, \beta_k) \neq \alpha_w + \alpha_a$ and/or $\beta \neq \beta_w + \beta_a$, then the normal-wave excitation is exponentially small and can be neglected. In this case, we obtain the standard eigenvalue problem

$$\left(\frac{\partial}{\partial y} - H_0\right)\vec{F}_{k0} = 0, \qquad (2.10a)$$

$$(F_{k0})_{1,3,5,7} = 0 \text{ at } y = 0, \qquad (2.10b)$$

$$\left|\vec{F}_{k0}\right| \to 0 \text{ at } y \to \infty. \qquad (2.10c)$$

Its solution describes propagation of normal waves in the boundary layer far from resonance regions and can be expressed as

$$\vec{F}_{k0} = c_k(x_1)\vec{A}_k(x_1, y, \alpha_k), \qquad (2.11)$$

where $\vec{A}_k$ are eigenfunctions normalized by a certain condition. For example, the pressure disturbance amplitude is constant on the wall: $\vec{A}_{k4}(x_1, 0, \alpha_k) = 1$. The amplitude functions $c_k(x_1)$ are unknown on this stage.

If the nonlinear term *is in resonance* with one of the normal waves (say the wave with eigenvalue α_n) at some point $x_1 = x_{10}$,

$$\alpha_n(x_{10}, \omega, \beta) = \alpha_w + \alpha_a \text{ and } \beta = \beta_w + \beta_a, \qquad (2.12)$$

then this normal wave is effectively generated by the acoustic wave due to relatively strong sound-waviness interaction near the resonance point x_{10}. We consider the case when the normal wave is unstable and the resonance point is close to the lower neutral branch. Scheme of the resonant excitation region is shown in Fig. 2. Analysis of governing terms in Eq. (2.8a) indicates that the resonance excitation occurs in the relatively small region $|x_1 - x_{10}| = O(\varepsilon^{1/2})$, where we can introduce the inner variable

$$\xi = \varepsilon^{-1/2}(x_1 - x_{10}) = O(1). \qquad (2.13)$$

We assume that

$$\beta = \beta_w + \beta_a \text{ and } \alpha_w + \alpha_a = \alpha_0 + \gamma \varepsilon^{1/2}, \qquad (2.14)$$

where $\alpha_0 \equiv \alpha_n(x_{10}, \omega, \beta)$, and the real parameter γ characterizes resonance detuning. Now the inner solution of the problem (2.8a)-(2.8c) can be expressed in the form

$$\vec{F} = \varepsilon_a h[\varepsilon^{-1/2} c(\xi) \vec{A}_0(y) + \vec{A}_1(\xi, y) \ldots] \exp(i\varepsilon^{-1/2} \alpha_0 \xi + i\beta z), \qquad (2.15)$$

where $\vec{A}_0(y) = \vec{A}_n(x_{10}, y, \alpha_0)$ is normal-wave eigenfunction at the resonance point. Expanding the operator H_0 in the vicinity of $x = x_{10}$ we obtain the following problem for the vector-function $\vec{A}_1$

$$\left(\frac{\partial}{\partial y} - H_0(x_{10}, \alpha_0) \right) \vec{A}_1 = -i \frac{dc}{d\xi} \frac{\partial H_0}{\partial \alpha}(x_{10}, \alpha_0) \vec{A}_0 + c\xi \frac{\partial H_0}{\partial x_1}(x_{10}, \alpha_0) \vec{A}_0 + G\vec{F}_a \exp(i\gamma\xi),$$

$$(2.16a)$$

$$(A_1)_{1,3,5,7} = 0 \text{ at } y = 0, \qquad (2.16b)$$

18

$$\left| \vec{A}_1 \right| \rightarrow 0 \ \text{at} \ y \rightarrow \infty. \tag{2.16c}$$

This problem is similar to the problem (2.20) in [4]. It has non-trivial solution, if its right-hand side is orthogonal to the eigenfunction $\vec{B}_0 = \vec{B}_n(x_{10}, y, \alpha_0)$ of the conjugate problem. This condition leads to the following equation for the amplitude coefficient $c(\xi)$

$$\frac{dc}{d\xi} - ib\xi c = q\exp(i\gamma\xi), \tag{2.17a}$$

$$b = \frac{d\alpha_n}{dx_1}(x_{10}), \tag{2.17b}$$

$$q = i\frac{<\vec{B}_0, G(x_{10})\vec{F}_a>}{<\vec{B}_0, \dfrac{\partial H_0}{\partial \alpha}(x_{10}, \alpha_0)\vec{A}_0>}, \tag{2.17c}$$

where the scalar product is defined as

$$<\vec{B}, \vec{A}> = \int_0^\infty \sum_{j=1}^8 \overline{B}_j A_j dy, \tag{2.18}$$

the upper bar denotes complex conjugate values. Nonzero elements of the nonlinear interaction matrix G are represented in Apendix. If the normal wave has zero amplitude upstream from the resonance region, then the boundary condition for Eq. (2.17a) is specified as

$$c(\xi) \rightarrow 0 \ \text{at} \ \xi \rightarrow -\infty. \tag{2.19}$$

Problem (2.17a)-(2.19) coincides with the problem (2.21a)-(2.22) of [4], if we replace the numerator $(\vec{B}_0, \vec{\Phi}_0)$ in Eq. (2.21c) by the scalar product $<\vec{B}_0, G(x_{10})\vec{F}_a>$. Using this similarity we obtain the normal-wave amplitude downstream from the resonance region

$$\vec{F}_n = \varepsilon_a h \varepsilon^{-1/2} q \sqrt{\frac{2\pi i}{b}} \exp\left(\frac{i\gamma^2}{2b}\right) \vec{A}_n(x_1, y) \exp\left[i\varepsilon^{-1}\int_{x_{10}}^{x_1} \alpha_n(x_1)dx_1\right], \text{ for } x_1 > x_{10}. \quad (2.20)$$

This equation shows that the normal-wave amplitude is proportional to $(L^*/\delta^*)^{1/2} = R_L^{1/2}$, whereas the resonant region length is $l^* = R_L^{1/2}\delta^*$. As the Reynolds number increases, nonparallel effects (which disturb the resonance condition) decrease and the relative length l^*/δ^* increases. In the parallel mean-flow limit, $R_L \to \infty$, the resonance region is infinitely large and the normal wave amplitude tends to infinity. In this case, the upper limit of the disturbance amplitude is determined by nonlinear effects of the higher order approximation. These conclusions are similar to those formulated in [4] for receptivity to wall disturbances.

Note that nonparallel effects make the receptivity mechanism to be local in units of L^* even for distributed roughness. However it can be treated as a distributed mechanism in units of δ^*. Our choice of the term "distributed receptivity" is a matter of convention.

2.2 Local receptivity on hump

We consider a spanwise row of local humps on a flat plate surface. For brevity we analyze one spanwise harmonic of this periodic structure, and specify its shape as

$$y_w(x, y, z) = hg(x')\exp(i\beta_w z) + (c.c), \quad x' = x - x_0 \equiv \varepsilon^{-1}(x_1 - x_{10}). \quad (2.21)$$

The shape-function is represented by the Fourier integral

$$g(x') = \frac{1}{2\pi}\int_{-\infty}^{+\infty} \rho(\alpha_w)\exp(i\alpha_w x')d\alpha_w, \quad (2.22)$$

which can be expressed in the form

$$g = \frac{1}{2\pi} \varepsilon^{1/2} \exp(i\alpha_{w0}x') \int_{-\infty}^{+\infty} \rho(\alpha_{w0} + \varepsilon^{1/2}\gamma) \exp(i\gamma\xi) d\gamma . \qquad (2.23)$$

Here $\alpha_{w0} = \alpha_n(x_{10}, \omega, \beta) - \alpha_a$ is wavenumber component fitting to the resonance condition (2.12), and γ characterizes resonance detuning in accordance with Eq. (2.14). Using the relation (2.20) for the normal-wave amplitude excited by one harmonic and integrating over γ we obtain

$$\vec{F}_n = \varepsilon_a hq\rho(\alpha_{w0})\vec{A}_n(x', y)\exp\left(i\int_0^{x'} \alpha_n(x')dx' + i\beta z \right). \qquad (2.24)$$

This expression is similar to Eq. (2.33) of [4] for a local wall forcing. Important that the function $q(x_{10}, \alpha_0, \alpha_a, \beta_a)$ does not depend on the hump shape $g(x')$. If this function is calculated once and for all, then we can evaluate the normal wave amplitude generated by the sound wave interacting with a wall hump of arbitrary shape (within the limit of our assumptions).

The acoustic wave interacting with a local hump generates the boundary-layer normal wave of a finite amplitude even in the parallel mean flow. This is due to the fact that only a small portion of the hump spectrum, $(\alpha_w - \alpha_{w0}) = O(\varepsilon^{1/2})$, is involved into the resonance mechanism. As $\varepsilon \to 0$, the resonant excitation increases proportionally to $\varepsilon^{-1/2}$, whereas the active spectrum region is narrowed down proportionally to $\varepsilon^{1/2}$. Because both trends compensate each other, the normal-wave amplitude tends to a finite value.

Note that Eqs. (2.20) and (2.24) hold for any combinations of freestream disturbances and wall perturbations. For example, if we replace the acoustic wave by vortical (entropy) wave, then these expressions provide the normal wave amplitude generated by vortical (entropy) wave interacting with a surface irregularity. The normal wave can also be of

21

different nature such as Tollmien-Schlichting wave, second mode, cross-flow vortices, Görtler vortices *etc.* All these cases can be treated using the same computational module, which

1. solves Problem (2.6a)-(2.6c) for wall-induced disturbance;
2. solves Problem (2.7a)-(2.7c) for external (freestream) disturbance;
3. solves the eigenvalue problem (2.10a)-(2.10c) and its conjugate problem to obtain the normal-wave eigenfunctions $\vec{A}_n(x_1, y)$ and $\vec{B}_n(x_1, y)$;
4. evaluates the scalar products of Eqs. (2.17c);
5. predicts the normal-wave amplitude using Eq. (2.20) for distributed receptivity or Eq. (2.24) for local receptivity.

Such a module was developed and coupled with our stability solver.

2.3 Receptivity near spectrum branch points

Foregoing analysis is valid for "simple" discrete spectrums; *i.e.* eigenvalues of the boundary-layer modes are assumed to be different. This is typical for subsonic and moderate supersonic boundary layers as well as hypersonic boundary layers on adiabatic walls. The analysis of [1, 2, 4] showed that the first and second modes have branch points which are close to the real parameter space in the case of low wall temperature ratios. The upstream branch point, $x_1 = x_{1b}$, is located near the lower neutral branch of the second mode whereas the downstream branch point is close to the upper neutral branch. In the branch-point vicinity (say for the upstream point x_{1b}), the eigenvalues behave as

$$\alpha_{1,2} = \alpha_b \pm i\lambda\sqrt{x_1 - x_{1b}} + \ldots, \tag{2.25}$$

where $\alpha_b \equiv \alpha_1(x_{1b}, \omega) = \alpha_2(x_{1b}, \omega)$.

The following analysis is focused on the upstream branch point. The receptivity factor q in Eq. (2.17c) tends to infinity as the resonance point tends to the branch point, $x_{10} \to x_{1b}$. This singularity is due to the fact that the scalar product

$$\left\langle \frac{\partial H_0}{\partial \alpha}(x_{10}, \alpha_0)\vec{A}_0, \vec{B}_0 \right\rangle \to 0, \text{ as } x_{10} \to x_{b1}.$$ (2.26)

The eigenvalue derivative, which is involved into Eq. (2.20) for distributed receptivity, behaves as

$$b = \frac{d\alpha_n}{dx_1}(x_{10}) \to \infty, \text{ as } x_{10} \to x_{b1}.$$ (2.27)

This singularity has been studied in [4] for the case of receptivity to wall-induced perturbations. Since the analysis of [4] is easily extended to the problem considered in this report, we will briefly indicate key points of this extension and summarize the results. For brevity, we consider two-dimensional normal waves with $\beta = 0$.

Near the branch point, Mode 1 (with the eigenvalue $\alpha_1(x_1, \omega)$) strongly interacts with Mode 2 (with the eigenvalue $\alpha_2(x_1, \omega)$) due to nonparallel effects. This interaction can be described by the two-mode approximation; *i.e.* the disturbance amplitude from Eq. (2.5) is expressed in the form

$$\vec{F}(x_1, y) = c_1(x_1)\vec{A}_1(x_1, y)\exp(\varepsilon^{-1}iS_1) + c_2(x_1)\vec{A}_2(x_1, y)\exp(\varepsilon^{-1}iS_2).$$ (2.28)

Far from the resonance regions, the amplitude coefficients $c_{1,2}(x_1)$ are solutions of the ODE problem

$$\frac{dc_1}{dx_1} = c_1W_{11} + c_2W_{12}\exp[\varepsilon^{-1}i(S_2 - S_1)],$$ (2.29a)

23

$$\frac{dc_2}{dx_1} = c_2 W_{22} + c_1 W_{21} \exp[\varepsilon^{-1} i(S_1 - S_2)], \qquad (2,29b)$$

$$c_1(x_{1s}) = c_{1s}, \quad c_2(x_{1s}) = c_{2s}, \qquad (2.29c)$$

where c_{1s} and c_{2s} are prescribed values at a certain initial point x_{1s}; the matrix elements are defined as

$$W_{jk} = -\frac{\left\langle \vec{B}_j, \dfrac{\partial H_0}{\partial \alpha} \dfrac{\partial \vec{A}_k}{\partial x_1} \right\rangle + i \left\langle \vec{B}_j, H_1 \dfrac{\partial \vec{A}_k}{\partial x_1} \right\rangle}{\left\langle \vec{B}_j, \dfrac{\partial H_0}{\partial \alpha} \dfrac{\partial \vec{A}_j}{\partial x_1} \right\rangle}, \quad j = 1, 2, \ k = 1, 2; \qquad (2.30)$$

where the matrix H_1 is relevant to nonparallel effects. Its elements depend on the mean-flow profile derivatives $\partial U / \partial x_1$, $\partial T / \partial x_1$ and vertical velocity V_0. Near the branch point, the matrix elements (2.30) behave as

$$W_{jk} \to \frac{(-1)^{j+k-1}}{4(x_1 - x_{1b})}, \ x_1 \to x_{1b}. \qquad (2.31)$$

That leads to the following singularity of the amplitude coefficients

$$c_{1,2}(x_1) = \frac{C_{1,2}}{(x_1 - x_{1b})^{1/4}} + \ldots, \text{ as } x_1 \to x_{1b}, \qquad (2.32)$$

where constants $C_{1,2}$ depend on the normalization of eigenfunctions $\vec{A}_{1,2}(x_1, y)$.

In the region $x_1 - x_{1b} = O(\varepsilon^{2/3})$, the mode decomposition (2.28) is replaced by the local expansion with the inner variable $\zeta = \varepsilon^{-2/3}(x_1 - x_{1b})$

24

$$\vec{F} = \varepsilon^{-1/6}[c_0(\zeta)\vec{A}_0(y) + \varepsilon^{-1/3}c_{01}(\zeta)\vec{A}_{01}(y) + ...]\exp(i\varepsilon^{-1}S_b + i\varepsilon^{-1/3}\alpha_b\zeta).\quad (2.33)$$

Here $c_0(\zeta)$ is solution of Airy equation

$$\frac{d^2c_0}{d\zeta^2} - \lambda^2\zeta c_0 = 0.\qquad (2.34)$$

Matching the inner and outer solutions we can establish an exchange rule in the branch-point vicinity [2, 4]. The local expansion (2.33) indicates that the disturbance amplitude has a peak in the branch-point influence domain $\zeta = O(1)$, with maximum amplitude being of the order of $\varepsilon^{-1/6}$. To separate this effect from the receptivity mechanism we need to establish a relationship between the constants $C_{1,2}$ (instead of the amplitude functions $c_{1,2}$) and characteristics of incident acoustic wave plus wall disturbance.

Wavy wall

If the incident acoustic wave interacts with the wall waviness, then the unstable normal-wave amplitude is expressed as

$$\vec{F}_n = \varepsilon_a h \varepsilon^{-1/2}\frac{\sqrt{\pi\lambda}}{(x_{10} - x_{1b})^{1/4}}\frac{<\vec{B}_0, G(x_{10})\vec{F}_a>}{\left\langle \vec{B}_0, \frac{\partial H_0}{\partial x_1}(x_{10}, \alpha_0)\vec{A}_0 \right\rangle}\vec{A}_n(x_1, y)\exp\left[i\varepsilon^{-1}\int_{x_{10}}^{x_1}\alpha_n(x_1)dx_1\right], (2.35)$$

$$x_1 > x_{10}.$$

Whereas the local amplitude coefficient of the unstable mode n is

$$C_n = \varepsilon_a h \varepsilon^{-1/2}\sqrt{\pi\lambda}\frac{<\vec{B}_0, G(x_{10})\vec{F}_a>}{\left\langle \vec{B}_0, \frac{\partial H_0}{\partial x_1}(x_{1b}, \alpha_b)\vec{A}_0 \right\rangle}\quad \text{as } x_{10} \to x_{1b}.\qquad (2.36)$$

25

Equation (2.36) shows that *distributed receptivity has no singularity at the spectrum branch point.* In accordance with Eq. (2.32), the disturbance peak is totally due to a singular behavior of the unstable mode itself. If one measures the disturbance amplitude Q_n at a certain fixed point downstream from the branch point for various locations of the resonant point x_{10}, then he will not observe significant changes in the distribution $Q_n(x_{10})$ near the point $x_{10} = x_{1b}$. This conclusion is similar to that formulated in [4] for receptivity to wall-induced disturbances.

Local hump

If the hump is far from the branch point, then the normal-wave amplitude is determined from Eq. (2.24). As the hump approaches the branch point, the receptivity factor behaves as

$$q \to \frac{<\vec{B}_0, G(x_{10})\vec{F}_a>}{\left\langle \vec{B}_0, \dfrac{\partial H_0}{\partial x_1}(x_{10}, \alpha_0)\vec{A}_0 \right\rangle} \frac{\lambda \rho(\alpha_0)}{2(x_{10} - x_{1b})^{1/2}}, \text{ as } x_{10} \to x_{1b}. \tag{2.37}$$

Then the amplitude coefficient from Eq. (2.32) is expressed in the branch point vicinity in the form

$$C_n = \varepsilon_a h \frac{<\vec{B}_0, G(x_{10})\vec{F}_a>}{\left\langle \vec{B}_0, \dfrac{\partial H_0}{\partial x_1}(x_{10}, \alpha_0)\vec{A}_0 \right\rangle} \frac{\lambda \rho(\alpha_0)}{2(x_{10} - x_{1b})^{1/4}}, \text{ as } x_{10} \to x_{1b}. \tag{2.38}$$

Local receptivity increases proportionally to $(x_{10} - x_{1b})^{-1/4}$ as the hump approaches the branch point. This effect is due to the increase of the active wavenumber range of the hump spectrum. If the hump is far from the branch point, then this range is estimated as $(\alpha_w + \alpha_a - \alpha_0) = O(\varepsilon^{1/2})$. If the hump is placed in the region $(x_{10} - x_{1b}) = O(\varepsilon^{2/3})$, then the active wavenumber range becomes of the order of $(\alpha_w + \alpha_a - \alpha_0) = O(\varepsilon^{1/3})$. In this case, the amplitude coefficient is estimated as $C_n = O(\varepsilon_a h \varepsilon^{-1/6})$.

Analysis of the inner solution (2.33) and its matching with the outer solution lead to the following expression for the normal wave amplitude

$$\vec{F}_n = \varepsilon_a h \varepsilon^{-1/6} \frac{\lambda \rho(\alpha_b) \Gamma(1/3)}{2\sqrt{\pi} (x_1 - x_{1b})^{1/4}} \left(\frac{\lambda}{3}\right)^{1/6} \frac{< \vec{B}_b, G(x_{1b}) \vec{F}_a >}{\left\langle \vec{B}_b, \dfrac{\partial H_0}{\partial x_1} \vec{A}_b \right\rangle_b} \vec{A}_n(x_1, y) \exp\left(i \int_{x_{10}}^{x_1} \alpha_n(x_1) dx_1 \right),$$

(2.39)

where $\varepsilon^{2/3} << x_1 - x_{1b} << 1$; subscript "$b$" denotes quantities evaluated at $x_1 = x_{1b}$; Gamma-function $\Gamma(1/3) = 2.678938....$ From this expression and Eq. (2.32) we obtain the amplitude coefficient

$$C_n = \varepsilon_a h \left(\frac{\lambda}{3\varepsilon}\right)^{1/6} \frac{\lambda \rho(\alpha_b) \Gamma(1/3)}{2\sqrt{\pi}} \frac{< \vec{B}_b, G(x_{1b}) \vec{F}_a >}{\left\langle \vec{B}_b, \dfrac{\partial H_0}{\partial x_1} \vec{A}_b \right\rangle_b}.$$

(2.40)

Summarizing we conclude that local receptivity strongly depends on the distance between the hump and branch point. As $x_{10} \to x_{1b}$, the amplitude coefficient C_n increases proportionally to $|x_{10} - x_{1b}|^{-1/4}$ and attains its maximum value of the order of $\varepsilon_a h \varepsilon^{-1/6}$ at the branch point $x_{10} = x_{1b}$. If one measures the disturbance amplitude Q_n at a certain fixed point downstream from the branch point for various hump locations, then he will observe a local peak in the distribution $Q_n(x_{10})$ near the point $x_{10} = x_{1b}$. Because the branch point is close to the lower neutral branch, this peak will be enhanced by the exponential growth of unstable disturbance. This result is consistent with that obtained in [4] for receptivity to wall-induced disturbances.

3. Numerical results

Receptivity calculations were conducted for the boundary layer on a flat plate at local Mach number $M = 6$, stagnation temperature $T_0^* = 390°$ F, and wall temperature $T_w^* = 80°$ F that corresponds to the wall temperature ratio $T_w^* / T_0^* = 0.6356$. Dr. Roger Kimmel indicated this case as a good candidate for the Mach 6 wind tunnel experiment. It is assumed that the fluid is a perfect gas with a constant specific heats ratio $\gamma = 1.4$ and Prandtl number $\mathrm{Pr} = 0.72$. The viscosity-temperature dependency is approximated by Sutherland's law

$$\mu(T) = \frac{(1+S)}{(T+S)} T^{3/2}, \tag{3.1}$$

where $S = 110/T_e^*$ for air temperature measured in degrees Kelvin; $\mu = \mu^* / \mu_e^*$ is nondimensional viscosity. Hereafter the global length scale is $L^* = x^*$, the local scale is self-similar boundary-layer scale $\delta^* = \sqrt{v_e^* x^* / U_e^*}$, the Reynolds number is $R_L = R = \sqrt{U_e^* x^* / v_e^*}$ and $\varepsilon = \delta^* / L^* = R^{-1}$.

3.1 Mean flow

We neglect effects of hypersonic viscous-inviscid interaction and assume that flow characteristics at the upper boundary-layer edge coincide with the freestream characteristics. The laminar boundary-layer flow is approximated by the self-similar profiles $U(y)$ and $T(y)$, with the boundary-layer variable $y = y^* / \sqrt{v_e^* x^* / U_e^*}$. These profiles and their first derivatives are shown in Figs. 3 and 4. In this case, the boundary-layer thickness is $\Delta^* = 16.73 \sqrt{v_e^* x^* / U_e^*}$ (here $U^*(\Delta^*) = 0.99 U_e^*$), and the displacement thickness $\Delta_d^* = 13.64 \sqrt{v_e^* x^* / U_e^*}$. Figure 4 shows that the wall temperature is slightly below the adiabatic-wall temperature.

28

3.2 Second mode

Characteristics of two-dimensional normal waves have been calculated for the second-viscosity coefficient $k = 1.2$ ($k = 0$ corresponds to Stokes). In Figs. 5 and 6, the eigenvalue distributions $\alpha_2(R)$ are shown for various frequency parameters $F = \omega^* v_e^* / U_e^{*2}$. Figures 7 and 8 illustrate the phase-speed distributions $c_2(R) = \mathrm{Re}(\omega / \alpha_2)$ and the branch-point locations respectively. The second-mode phase speed is smaller than the freestream speed and larger than the phase speed $c_a = 1 - 1/M$ of the upper limit for slow acoustic waves. Local maximums (minimums) of $c_2(y)$ correlate with the upstream (downstream) branch point loci. Note that the branch points are close to neutral branches of the second mode. In accordance with the analysis [1, 2], this spectrum topology is typical for hypersonic boundary layers.

Figure 8 shows that the upstream branch points are below the real axis of complex R, and the downstream branch points are above this axis. In what follows, we assume that the branch-point influence domains are far enough from the real axis and use the theoretical model of Section 2 relevant to a simple discrete spectrum.

Distributions of the pressure amplitude, $p_2(y) = \gamma M^2 |A_{24}(y)|$, and streamwise mass-flux amplitude,

$$f_2(y) = \left| A_{21} + \left(\gamma M^2 A_{24} - \frac{A_{25}}{T} \right) U \right| \frac{1}{T}, \tag{3.2}$$

are shown in Fig. 9 for the point $F = 8. \times 10^{-5}$, $R = 1000$ located near the lower neutral branch. The eigenfunction is normalized as $p_2(0) = 1$. The streamwise mass-flux amplitude has a typical sharp maximum in the critical layer, where the disturbance phase speed is close to the mean-flow velocity.

3.3 Waviness-induced perturbations

The pressure contours $\mathrm{Re}[p_w(y,\alpha_w)] \equiv \gamma M^2 \, \mathrm{Re}[F_{w4}(y,\alpha_w)] = const$ are shown in Fig. 10 for the Reynolds number $R = 1000$. It is seen that the wavy wall generates steady Mach waves outside the boundary layer. Disturbances of maximum amplitude are observed at $\alpha_w \approx 0.75$. In the long-wave ($\alpha_w \to 0$) and sort-wave ($\alpha_w \to \infty$) limits, pressure amplitude vanishes. A major portion of the boundary layer is weakly perturbed. The first maximum of pressure fluctuations is located near the upper boundary-layer edge, where the second-mode critical layer is normally observed. Distributions of $\mathrm{Re}[p_w(y)]$ are shown in Fig. 11 for $\alpha_w = 0.001$, 0.05 and 0.1. It is seen that the pressure disturbance amplifies passing through the laminar boundary layer. Their amplitude in external inviscid flow is essentially higher than that within the boundary layer.

Contours of the streamwise mass flux component,

$$\mathrm{Re}[f_w(y,\alpha)] = \mathrm{Re}\left[F_{w1} + \left(\gamma M^2 F_{w4} - \frac{F_{w5}}{T} \right) U \right] \frac{1}{T} = const, \qquad (3.3)$$

are shown in Fig. 12 for the Reynolds number $R = 1000$. This pattern is qualitatively similar to the pressure pattern in Fig. 10 besides a sharp peak (dark blue region) at small wavenumbers. This peak is close to the upper boundary-layer edge.

Distributions $\mathrm{Re}[f_w(y,\alpha)]$ at the wavenumbers $\alpha = 0.001$, 0.05 and 0.1 are shown in Fig. 13. Similar to the case of pressure disturbances, the mass-flux amplitude outside the boundary layer is essentially higher than that observed within the boundary layer.

Contours of the static pressure amplitude, $|p_w(y,\alpha)| = const$, and the streamwise mass-flux amplitude, $|f_w(y,\alpha)| = const$, are represented in Fig. 14 and 15 respectively. These data give another illustration of mentioned above features of the waviness-induced

30

disturbance. In addition, it is seen that both distributions have a flat maximum near $\alpha \approx 0.075$.

3.4 Acoustic waves

Schematic pattern of acoustic waves generated by a cylindrical source in supersonic flow is shown in Fig. 16. The incident wave front is tangent to the flat surface at Point B. Near this point, acoustic waves propagate upstream and downstream with very high phase velocity and have the incidence angle $\Theta \approx 90°$. In Region AB, the phase speed of upstream front rapidly increases from $-\infty$ (at Point B) to 0 (at Point A, where the Mach wave crosses the plate surface). In this relatively short region, acoustic waves propagate upstream. At the turning point A, wave fronts stagnate and form an oscillating Mach wave. Then they turn back and move downsteam as *slow* acoustic waves with the phase speed $0 < c_a < 1 - 1/M$. The downstream fronts propagate with the phase speed decreasing from $+\infty$ (at Point B) to $c_a = 1 + 1/M$ (in far-downstream region). These fronts form *fast* acoustic waves.

To identify incident and reflected waves we consider the acoustic dispersion relation in the inviscid approximation. The pressure disturbance can be expressed as

$$p_a(x, y) = p_+ \exp(i\alpha_a x + ik_a y - i\omega t) + p_- \exp(i\alpha_a x - ik_a y - i\omega t), \qquad (3.4)$$

where

$$k_a = \sqrt{M^2(\alpha_a - \omega)^2 - \alpha_a^2}, \quad \mathrm{Re}(k_a) > 0. \qquad (3.5)$$

Analysis of the acoustic-front kinematics shows that

- for counter-flow waves (propagating upstream in Region AB) and fast waves, p_- corresponds to incident wave and p_+ to reflected wave;
- for slow waves, p_+ corresponds to incident wave and p_- to reflected wave.

31

This switch from one component to another is due to supersonic convection of acoustic fronts as schematically shown in Fig. 16. It is convenient to express the acoustic wavenumber as a function of the incidence angle Θ. From the dispersion relation (3.5) we obtain:

For slow waves

$$\alpha_a = \frac{\omega M \cos\Theta}{M \cos\Theta - 1}, \quad c_a \equiv \frac{\omega}{\alpha_a} = 1 - \frac{1}{M \cos\Theta}, \quad 0 < \Theta < \Theta_{cr}, \qquad (3.6)$$

where $\Theta_{cr} = \arccos(1/M)$ corresponds to the Mach wave incident angle.

For fast waves

$$\alpha_a = \frac{\omega M \cos\Theta}{M \cos\Theta + 1}, \quad c_a = 1 + \frac{1}{M \cos\Theta}, \quad 0 < \Theta < \pi/2. \qquad (3.7)$$

For counter-flow waves

$$\alpha_a = \frac{\omega M \cos\Theta}{M \cos\Theta - 1}, \quad c_a = 1 - \frac{1}{M \cos\Theta}, \quad \Theta_{cr} < \Theta < \pi/2. \qquad (3.8)$$

In all figures, presented hereafter, the acoustic wave incidence angle Θ is measured in degrees.

At hypersonic speeds, Region AB with counter-flow waves is very short and can be treated as a local region concentrated near the line of intersection between the Mach wave and the body surface. In this report, we do not consider receptivity to disturbances of this type. We will focus on the case when the plate is inside the Mach cone and its surface is radiated by slow and/or fast acoustic waves.

A good guidance to the interaction of acoustic waves with a hypersonic boundary layer is provided by the short-wave (WKB) analysis [22, 23]. Schematic picture of this interaction is shown in Fig. 17 for slow waves with the phase speed $a(0) < c_a < U_e - a_e$, where $a(y)$ is local sound speed. In the lower wave-guide, acoustic rays are reflected by the wall and refracted near the lower sonic line, $U(y) = c_a - a(y)$. In the upper half-space, incident acoustic waves are refracted near the upper sonic line, $U(y) = c_a + a(y)$. In the quiet zone between these two lines, the disturbance amplitude decays exponentially with the distance from the sonic lines. These qualitative features of the acoustic field-boundary layer interaction are used in the following discussion of numerical data.

Slow waves

Calculations have been performed for slow acoustic waves with the dispersion relation (3.6) at frequency $F = 8. \times 10^{-5}$ and Reynolds number $R = 1000$. The critical incidence angle is $\Theta_{cr} = 80.4°$ at the Mach number $M = 6$. Figure 18 shows contours of the pressure amplitude, $|p_a(y, \Theta)| = const$. Figure 19 represents the function $|p_a(y)|$ at various incident angles. Pressure waves weakly penetrate into the boundary layer because its major portion is covered by the quiet zone (see Fig. 17). Due to interference between reflected and incident waves, pressure amplitude oscillates from 0 to approximately 2 outside the boundary layer; *i.e.* the reflection coefficient is close to one and the boundary layer is passive with respect to pressure waves. A flat local maximum of the pressure amplitude is observed in the boundary layer at the incident angle $\Theta \approx 40°$. As $\Theta \rightarrow \Theta_{cr}$, the disturbance wavelength decreases, the phase speed $c_a \rightarrow 0$, and the upper sonic line moves toward the wall allowing pressure waves penetrates deeper into the boundary layer.

The streamwise mass-flux contours $|f_a(y, \Theta)| = const$ and the functions $|f_a(y)|$ are shown in Figs. 20 and 21 for various incidence angles. As contrasted to the pressure wave, the mass-flux disturbance has a peak near the upper boundary-layer edge. Its

maximum corresponds to the incident angle $\Theta \approx 40°$. Important that this peak overlaps with the second-mode peak in the critical-layer (see Fig. 9). Such an overlapping can increase the scalar product $< G(x_{10})\vec{F}_a, \vec{B}_0 >$ and enhance receptivity.

Figure 22 shows contours of the maximum streamwise mass-flux, $\max_{y}|f_a(y)|$, in the frequency-Reynolds number plane. It is seen that the mass-flux amplitude monotonically decreases with R and F.

Fast waves

Characteristics of fast acoustic waves were calculated at the same frequency $F = 8.\times10^{-5}$ and Reynolds number $R = 1000$. The pressure amplitude distributions are shown in Figs. 23 and 24. Fast waves have no sonic lines and quiet zone because their phase speed is $c_a > U_e + a$. Acoustic rays can easily penetrate into the boundary layer that changes the pressure amplitude pattern (compare Figs. 18 and 23). Because of this, the maximum of $|p_a(y)|$ is observed near the wall. Its extremum corresponds to the incident angle $\Theta \approx 50°$.

The streamwise mass-flux contours, $|f_a(y,\Theta)| = const$, and the functions, $|f_a(y)|$, are shown in Figs. 25 and 26 at various incidence angles. The mass-flux amplitude has a peak near the upper boundary-layer edge. It is higher and sharper than in the slow-wave case (see Figs. 20 and 21). Figure 27 shows the contours of $\max_{y}|f_a(y)|$ in the frequency-Reynolds number plane. Similar to the case of slow waves (see Fig. 22), the streamwise mass-flux amplitude of fast waves monotonically decreases with R and F.

Foregoing numerical examples indicate that hypersonic boundary layer is more sensitive to fast acoustic waves than to slow ones. That is consistent with the acoustic field topology predicted by the short-wave theory (Fig. 17). However the slow-wave phase speed is closer to the second-mode phase speed that is more preferable for receptivity.

34

The last argument is important for receptivity on smooth surfaces such as the leading-edge receptivity. However, it is not critical for receptivity to sound plus wall roughness, because the roughness shape can be always tuned to meet the synchronism condition (2.12).

Small incidence angles

Figures 18, 20 (for slow waves) and Figures 23, 25 (for fast waves) show that the disturbance amplitude decreases rapidly as the incidence angle tends to zero (phase speed $c_a \rightarrow 1 \pm 1/M$). This is due to the fact that the reflected acoustic wave is almost in counter-phase with the incident wave and they cancel each other in the boundary layer. The limit $\Theta \rightarrow 0$ needs to be analyzed carefully because the length scale of the amplitude variation in vertical direction tends to infinity, $l_y^* = (2\pi/k_a)\delta^* \rightarrow \infty$. According to the analysis of [2] nonparallel effects can change the acoustic field essentially if the length ratio is $l_y^*/\Delta_d^* = O(\Delta_d F^{1/2})$ ($\Delta_d = \Delta_d^*/\sqrt{v_e^* x^*/U_e^*}$ is nondimensional displacement thickness, which is $\Delta_d \approx 14$ in the case considered). Using Eqs. (3.5), (3.6) we obtain that the local-parallel approximation is not valid, if the incident angle $\Theta \leq O(\Delta F^{1/2})$. For the frequency parameter $F = 8. \times 10^{-5}$, this gives the restriction $\Theta \leq 7°$.

The asymptotic analysis [2] indicates that the boundary layer growth (nonparallel effect) causes diffraction of incident acoustic waves. As a result, acoustic field amplitude at the upper boundary-layer edge decreases in downstream direction. The boundary-layer displacement leads to formation of "quiet" zone near the plate surface and far from the leading edge.

For configuration shown in Fig. 16, a major portion of the plate surface is radiated by acoustic waves of small incidence angle. This is typical for acoustic sources to be at rest. Both the diffraction and the counter-phase interference can essentially reduce the sound amplitude in the boundary layer. This, in turn, reduces the normal-wave excitation due to

sound scattering by a roughness element located far downstream from the leading edge. However, in many practical cases, sound waves are generated by sources convected downstream. Their incidence angles are normally large. For example, the measurements of Laufer [24] indicated that a turbulent boundary layer on walls of a conventional wind tunnel radiates sound with the incidence angle larger than $45°$. These arguments indicate that receptivity experiments should cover a wide range of the acoustic-wave incidence angle. Special techniques need to be developed to simulate sound from convective acoustic sources.

3.5 Distributed receptivity on wavy surface

Using Eq. (2.20) we express the initial amplitude of the second-mode wave generated by wavy wall in the resonance region as

$$|p_2(x_{10},0)| = \varepsilon_a h \varepsilon^{-1/2} G_{p,dis}(x_{10}, \omega, \alpha_a), \qquad (3.9)$$

where $|p_2(x_{10},0)|$ is pressure amplitude on the wall surface; the receptivity function is expressed in the form

$$G_{p,dis} = \varepsilon^{-1/2} \left| q \sqrt{\frac{2\pi i}{b}} \gamma M^2 A_{24}(x_{10},0) \right|, \qquad (3.10)$$

$$q = i \frac{< \vec{B}_0, G(x_{10}) \vec{F}_a >}{< \vec{B}_0, \frac{\partial H_0}{\partial \alpha}(x_{10}, \alpha_0) \vec{A}_0 >}, \quad b = \frac{d\alpha_2}{dx_1}(x_{10}). \qquad (3.11)$$

The acoustic-wave vector-function, $\vec{F}_a$, is normalized by the condition (pressure amplitude of the incident wave at the upper boundary-layer edge)=1; *i.e.* $\varepsilon_a = p_{inc}^* / P_e^*$ at $y = y_e$. The waviness amplitude is measured in units of the local scale $\delta^* = \sqrt{v_e^* x_0^* / U_e^*}$, where x_0^* is resonance-point coordinate; *i.e.* $h = h^* / \sqrt{v_e^* x_0^* / U_e^*}$. The receptivity

36

function $G_{p,dis}$ is considered as a function of frequency parameter F, Reynolds number $R = \sqrt{U_e^* x_0^* / v_e^*}$ and acoustic-wave incidence angle Θ.

Because $|\text{Im}(\alpha_2)| \ll |\text{Re}(\alpha_2)|$ for all parameters under consideration, we use the following approximation of the resonance condition (2.12)

$$\alpha_w = \alpha_2(x_{10}, \omega) - \alpha_a \approx \text{Re}[\alpha_2(x_{10}, \omega) - \alpha_a]. \qquad (3.12)$$

Calculations of the distributed receptivity function $G_{p,dis}$ were performed for slow and fast acoustic waves of frequencies $F = 4. \times 10^{-5}, 6. \times 10^{-5}, 8. \times 10^{-5}$ and 10^{-4} in the Reynolds number ranges relevant to the second-mode instability (see Figs. 5 and 6).

For slow acoustic waves, the wavenumber α_a is expressed by Eq. (3.6) as a function of the incident angle Θ. Figures 28a-31a show the receptivity function $G_{p,dis}(\Theta, R)$. Figures 28b-31b represent the contours $G_{p,dis}(\Theta, R) = const$. In all cases, the receptivity function is highly non-uniform with respect to the Reynolds number. It has two sharp maximums: the first is observed near the lower neutral branch and the second near the upper neutral branch. Similar to the case of wall-induced disturbances [4], these maximums correlate with the discrete-spectrum branch points shown in Fig. 8.

The first maximum is of the most interest to the transition prediction methodology because it corresponds to the initial phase of instability amplification. The contour plots indicate that this maximum is observed at relatively high incidence angles, $\Theta \approx 65°$, for all frequencies considered. The second maximum may be of a particular interest to bypass modeling. It is slightly larger than the first maximum and observed at smaller incidence angles $\Theta \approx 40°$. Receptivity to acoustic waves of small Θ is on the order of magnitude lower than its maximum value. This is consistent with the fact that such acoustic waves do not penetrate into the boundary layer due to the counter-phase interference between incident and reflected waves (see Section 3.4).

For fast acoustic waves, the wavenumber α_a is specified by Eq. (3.7). Figures 32a-35a show the receptivity function $G_{p,dis}(\Theta, R)$, and Figures 32b-35b illustrate the contours $G_{p,dis}(\Theta, R) = const$. Receptivity to fast acoustic waves is higher than to slow ones. This is consistent with the fact that the fast-wave amplitude is larger than the correspondent slow-wave amplitude (see Section 3.4). The first and second maximums of the receptivity function merge into one maximum as the frequency increases. For $F > 6.\times 10^{-5}$, they form a relatively flat peak covering the unstable Reynolds number range. The receptivity function maximum is observed at the incidence angle $\Theta \approx 45°$. This maximum is a weak function of the disturbance frequency. As the incidence angle tends to zero, the receptivity function decreases rapidly.

3.6 Local receptivity on hump

Using Eq, (2.24) we can express the second-mode amplitude generated by acoustic waves on a local hump as

$$\left|p_2(x_{10},0)\right| = \varepsilon_a h G_{p,loc}(x_{10}, \omega, \alpha_a)\left|\rho(\alpha_{w0})\right|. \tag{3.13}$$

Here the local receptivity function is

$$G_{p,loc} = \left|q\gamma M^2 A_{24}(x_{10},0)\right|, \tag{3.14}$$

the Fourier component $\rho(\alpha_w)$ is determined as

$$\rho(\alpha_w) = \int_{-\infty}^{+\infty} g(x')\exp(-i\alpha_w x')dx', \tag{3.15}$$

the function q is given by Eq. (3.11). The resonance wavenumber α_{w0} is approximated by Eq. (3.12). Similar to the case of receptivity on a wavy wall, $G_{p,loc}$ is considered as a

38

function of the frequency parameter F, Reynolds number $R = \sqrt{U_e^* x_0^* / \nu_e^*}$ based on the hump center x_0^*, and the acoustic-wave incidence angle Θ.

The receptivity functions $G_{p,loc}(\Theta, R)$ and their contours $G_{p,loc}(\Theta, R) = const$ are shown in Figs. 36-39 for slow acoustic waves and in Figs. 40-43 for fast acoustic waves. Comparing these data with the distributed receptivity data shown in Figs. 28-35 we conclude that the local receptivity function is much lower than the distributed one, $G_{p,loc} \approx 10^{-2} G_{p,dis}$. However, qualitative behavior of $G_{p,loc}$ is similar to that observed for the distributed receptivity. This is due to the fact that the ratio,

$$\frac{G_{p,dis}}{G_{p,loc}} = \varepsilon^{-1/2} \left| \sqrt{\frac{2\pi i}{(d\alpha_2 / dx_1)_{x_1 = x_{10}}}} \right|, \qquad (3.16)$$

does not depend on characteristics of acoustic wave and roughness. In the cases considered, the eigenvalue derivative $d\alpha_2 / dx_1$ is a regular function of x_1 because the spectrum branch points are shifted to the complex R-plane as shown in Fig. 8. For this reason, the ratio (3.16) is a relatively weak function of the streamwise coordinate x_{10} or, what is the same, the Reynolds number R.

Note that in the case of hypersonic boundary layer on a cooled plate [1, 4], the branch points may be close to the real axis. Since the eigenvalue derivative tends to $\pm \infty$ in the branch-point vicinity (see Eq. (2.25)), the local behavior of the functions $G_{p,dis}$ and $G_{p,loc}$ will be different. In this case, we should use the receptivity model of Section 2.3.

4. Summary discussion

In this study, we extended the receptivity model developed in [4] for wall-induced perturbations to the case of freestream disturbances scattered by surface roughness. We considered the second-mode excitation by acoustic waves interacting with the wall waviness (distributed roughness) and hump (local roughness element). This problem includes the following components:

(a) stationary disturbances generated by surface roughness;

(b) acoustic disturbance resulted from the interaction of incident acoustic wave with the boundary-layer mean flow and wall;

(c) unsteady perturbation resulted from the nonlinear interaction of the roughness-induced disturbance with the acoustic wave.

As contrasted to the subsonic case, a 2-D acoustic source in supersonic flow generates slow waves with the phase speed $0 < c_a < 1 - 1/M$, fast waves with $c_a > 1 + 1/M$ and counter-flow waves with $c_a < 0$. The latter stagnate near the Mach line and form a local disturbance with zero phase speed. In this report, we analyzed receptivity to slow and fast acoustic waves only.

It is shown that the receptivity mechanism depends on the discrete spectrum topology. If the spectrum is simple (*i.e.* its branch points are essentially complex and their influence domains do not overlap with the real parameter space), then the receptivity mechanism reveals the following features:

- For distributed roughness, a strong excitation occurs in a local region of the length $l^* = R^{-1/2} L^* = R^{1/2} \delta^*$, where Component (c) is in resonance with the second-mode wave. In this region, the normal-wave amplitude is proportional to $(L^* / \delta^*)^{1/2} = R^{1/2}$. As the Reynolds number increases, the relative length of the resonance region, l^* / δ^*,

increases. As $R \to \infty$, the normal wave amplitude tends to infinity. In this case, the upper limit of the disturbance amplitude is determined by nonlinear effects of the higher-order approximation.

- For local roughness, the normal-wave amplitude is finite even in the parallel flow limit. This is due to the fact that only a small portion of the roughness spectrum, $(\alpha_w - \alpha_{w0}) = O(R^{-1/2})$, is involved into the resonance mechanism. As $R \to \infty$, the resonant excitation increases proportionally to $R^{1/2}$, whereas the active spectrum region is narrowed down proportionally to $R^{-1/2}$. Because both trends compensate each other, the normal-wave amplitude tends to a finite value.

If the branch-point influence domain overlaps with the real parameter space, then both propagation and excitation of normal waves are singular. The receptivity function tends to infinity as the resonance point approaches the spectrum branch point. Asymptotic analysis of this singularity leads us to the following conclusions:

- The second-mode excitation on a wavy wall (distributed roughness) is not singular at the branch point. The receptivity function peak is totally due to a singular behavior of the normal wave itself. If one measures the disturbance amplitude Q at a fixed point downstream from the branch point x_{1b} for various loci of the resonance point x_{10}, then he will not observe essential changes in the distribution $Q(x_{10})$ near the point $x_{10} = x_{1b}$.

- The second-mode excitation over a hump (local roughness) strongly depends on a distance between the hump locus x_{10} and the branch point. As $x_{10} \to x_{1b}$, the normal-wave amplitude increases proportionally to $|x_{10} - x_{1b}|^{-1/4}$ and attains its maximum value of the order of $\varepsilon_a h \varepsilon^{-1/6}$ at $x_{10} = x_{1b}$. If one measures the disturbance amplitude Q at a fixed point downstream from the branch point for various loci of the forcing element, then he will observe a local peak in the distribution $Q(x_{10})$ at the point $x_{10} = x_{1b}$.

41

The analytical results were build in a computational module, which was coupled with our stability solver. Detailed calculations were performed for two-dimensional disturbances interacting with the flat-plate boundary layer at the Mach number $M = 6$, wall temperature $T_w^* = 80°$ F and stagnation temperature $T_0^* = 390°$ F. This case is considered as a good candidate for receptivity experiments in the Mach 6 quiet wind tunnel. The spectrum calculations showed that the branch points are essentially complex. That motivated us to perform receptivity calculations under the assumption that the spectrum is simple. Numerical studies lead us to the following conclusions:

1. In the boundary layer, the pressure amplitude of fast acoustic waves is larger than that of slow waves with the same frequency and incidence angle. The amplitude maximum is observed at the incidence angle $\Theta \approx 40°$ for slow waves and $\Theta \approx 45°$ for fast waves. Due to counter-phase interference between the incident and reflected waves, the disturbance amplitude decreases rapidly as the incidence angle tends to zero. This trend is opposite to the subsonic case when the incident and reflected waves are in phase.

2. *For receptivity on wavy-wall*, the receptivity function is highly non-uniform with respect to the Reynolds number.

   - In the case of slow acoustic waves, it has two maximums: the first is close to the lower neutral branch and the second to the upper neutral branch. These maximums correlate with the spectrum branch points. The boundary layer is the most receptive to acoustic waves of relatively high incidence angles: $\Theta \approx 65°$ near the first maximum and $\Theta \approx 40°$ near the second maximum.

   - In the case of fast acoustic waves, the receptivity maximums merge into one relatively flat maximum covering the instability region. The boundary layer is most receptive to acoustic waves of the incidence angle $\Theta \approx 45°$.

- Receptivity to both slow and fast acoustic waves of small incidence angles is on the order of magnitude lower than its maximum level.

3. *For receptivity on local hump*, the receptivity function has the same qualitative behavior as in the wavy-wall case. However its quantity is essentially smaller: $G_{p,loc} \approx 10^{-2} G_{p,dis}$.

This study does not cover all aspects of the hypersonic boundary-layer receptivity to sound scattered by roughness. The following issues will need to be addressed in future effort:

- For the boundary layers on cooled surfaces, the spectrum branch points may be very close to the real parameter space. Careful studies of the receptivity mechanism in the branch point vicinity should be performed.

- Calculations have been conducted for two-dimensional cases only. Since in the majority of practical cases (including wind-tunnel experiments), acoustic sources and roughness elements are three-dimensional, analysis of 3-D receptivity will be useful.

- Receptivity to acoustic disturbances concentrated near the line of intersection between the Mach cone and body surface may play important role in the instability excitation. This problem seems to be relevant to the boundary-layer interaction with oscillating shocklets.

- Parametric studies of hypersonic receptivity to entropy and vorticity disturbances scattered by surface irregularities are also required.

- It is feasible to compare the results of this study with our previous results relevant to the leading-edge receptivity [1], vorticity/entropy swallowing [2], and receptivity to wall-induced perturbations. This will help to identify the most probable scenarios of the initial transition phase for typical practical cases.

References

1. Fedorov, A.V., "Laminar Turbulent Transition in a Hypersonic Boundary Layer," EOARD Report SPC-96-4024, July 1996.

2. Fedorov, A.V., and Khokhlov, A.P., "Excitation and Evolution of Unstable Disturbances in Supersonic Boundary Layers," in: *Transitional and Turbulent Compressible Flows*, ASME Vol. 151, pp. 1-13, 1993.

3. Maslov, A.A., Shiplyuk, A.A., Sidorenko, A.A., and Arnal, D., "Leading Edge Receptivity of the Hypersonic Boundary Layer," Preprint No. 1-97, Institute of Theoretical and Applied Mechanics SO RAN and Center d'Etudes et de Recherches de Toulouse, Novosibirsk, 1998.

4. Fedorov, A.V., "Receptivity of Hypersonic Boundary Layer to wall Disturbances," EOARD Report SPC-98-4036, MIPT/FALT-1999-010, Moscow Institute of Physics and Technology, May 1999.

5. Aizin, L.B., and Polyakov, M.F., "Acoustic Generation of Tolmien-Schlichting Waves over Local Unevenness of Surface Immersed in Stream," Preprint No. 17, SO AN SSSR, Institute of Theoretical and Applied Mechanics, Novosibirsk, 1979 (in Russian).

6. Fedorov, A.V., "Excitation and Development of Unstable Disturbances in Compressible Boundary Layer," Ph.D. Dissertation, Moscow Institute of Physics and Technology, 1982 (in Russian).

7. Zavol'skii, N.A., Reutov, V.P., Rybushkina, G.V., "Excitation of Tollmien-Schlichting Waves by Acoustic and Vortex Disturbance Scattering in Boundary Layer on a Wavy Surface," *J. Appl. Mech. Tech. Phys.*, Vol. 24, pp. 355-361, 1983.

8. Zhigulev, V.N., and Fedorov, A.V., "Boundary Layer Receptivity to Acoustic Disturbances," *J. Appl. Mech. And Tech. Phys.*, Vol. 28, pp. 28-34, 1987.

9. Zhigulev, V.N., and Tumin, A.M., *Onset of Turbulence*, Nauka, Novosibirsk, 1987.

10. Goldstein, M.E., "Scattering of Acoustic Waves into Tollmien-Schlichting Waves by Small Streamwise Variations in Surface Geometry," *J. Fluid Mech.*, Vol. 154, p. 509, 1985.

11. Ruban, A.I., "On the Generation of Tollmien-Schlichting Waves by Sound," *Fluid Dyn.*, Vol. 19, p. 709, 1985.

12. Goldstein, M.E., and Hultgren, L.S., "Boundary-Layer Receptivity to Long-Wave Free-Stream Disturbances," *Annu. Rev. Fluid Mech.*, Vol. 21, p. 137, 1989.

13. Nishioka, M., and Morkovin, M.V., "Boundary-Layer Receptivity to Unsteady Pressure Gradients: Experiments and Overview," *J. Fluid Mech.*, Vol. 171, p. 219, 1989.

14. Kerschen, E.J., "Boundary Layer Receptivity Theory," AIAA Paper No. 89-1109, 1989.

15. Wiegel, M., and Wlezein, R.W., "Acoustic Receptivity of Laminar Boundary Layers over Wavy Walls," AIAA Paper No. 93-3280, 1993.

16. Choudhari, M., Street, C.L., "A Finite Reynolds-Number Approach for the Prediction of Boundary-Layer Receptivity in Localized Regions," *Phys. Fluids*, A Vol. 4 (11), pp. 2495-2514, 1992.

17. Choudhari, M., Streett, C.L., "Theoretical Prediction of Boundary-Layer Receptivity," AIAA Paper No. 94-2223, 1994.

18. Crouch, J.D., "Theoretical Studies on the Receptivity of Boundary Layers," AIAA Paper No. 94-2224, 1994.

19. Saric, W.S., Hoos, J.A., and Radeztsky, R.H., "Boundary-Layer Receptivity of Sound with Roughness," in: Boundary Layer Stability and Transition to Turbulence, ASME FED-Vol. 114, pp. 17-22, 1991

20. Choudhari, M., and Streett, C., Boundary Layer Receptivity Phenomena in Three-Dimensional and High-Speed Boundary Layers," AIAA Paper No. 90-5258, 1990.

21. Bogolepov, V.V., and Neiland, V.Ya., "Viscous Flow over Small Irregularities on Supersonic Body Surface," *Trudy TsAGI*, vyp. 1363, 1971.

22. Mack, L.M., "Boundary-Layer Stability Theory," JPL Rep. No. 900-277, Rev. B, Passadena, California, 1969.

23. Guschin V.R., and Fedorov, A.V., "Asymptotic Analysis of Inviscid Perturbations in a Supersonic Boundary Layer," *Zhurnal Prilk. Mekh. I Tekh. Fiz.*, No. 1, pp. 69-75, 1989 (translated in English).

24. Laufer, J., "Some Statistical Properties of the Pressure Field Radiated by a Turbulent Boundary Layer," *Phys. Fluids*, Vol. 7, pp. 1191-1197, 1964.
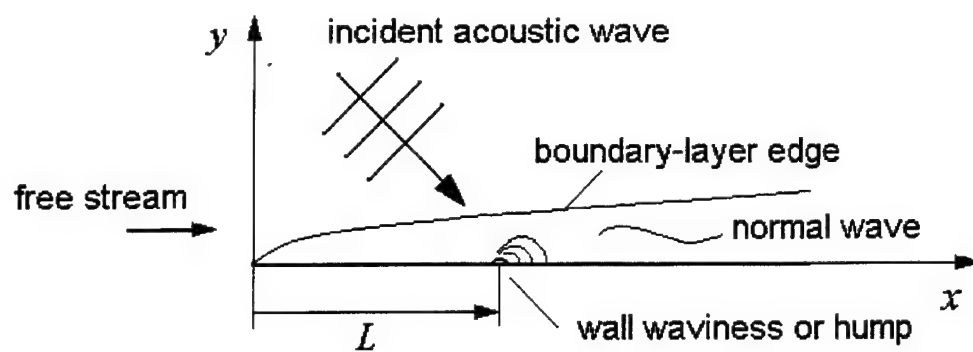
Fig. 1 Flow scheme.
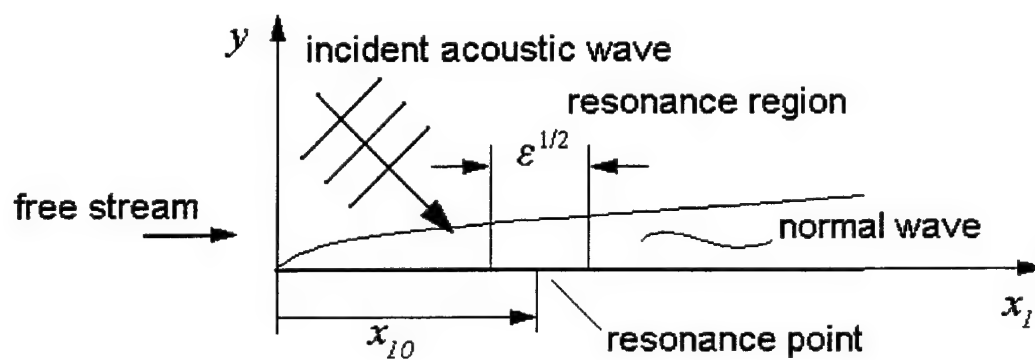
Fig. 2 Flow scheme for resonant excitation.
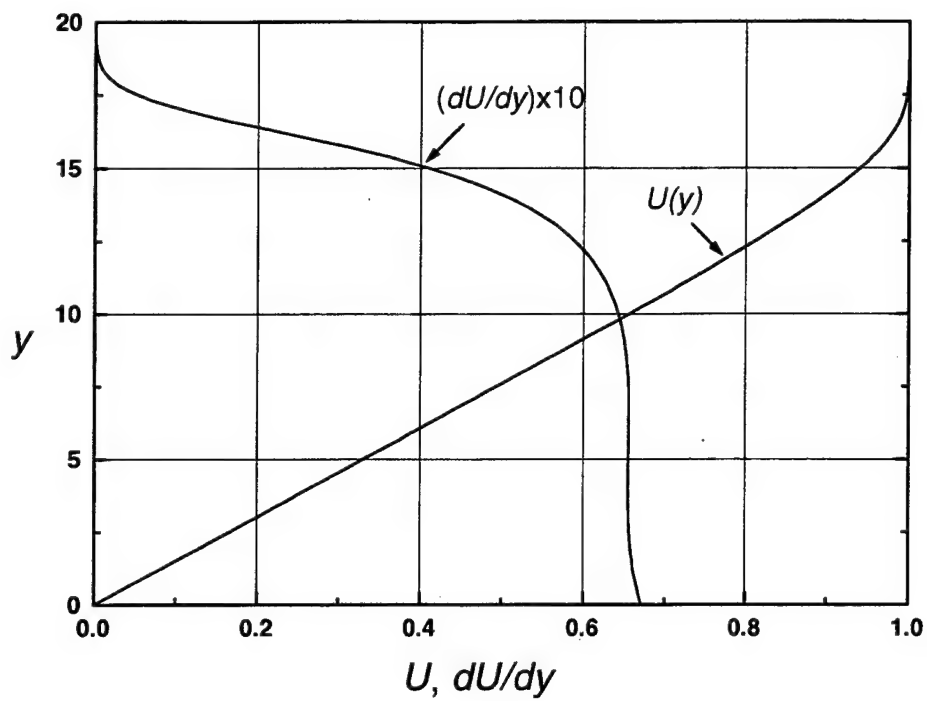
Fig. 3 Mean-flow velocity profiles $U(y)$, and dU/dy.
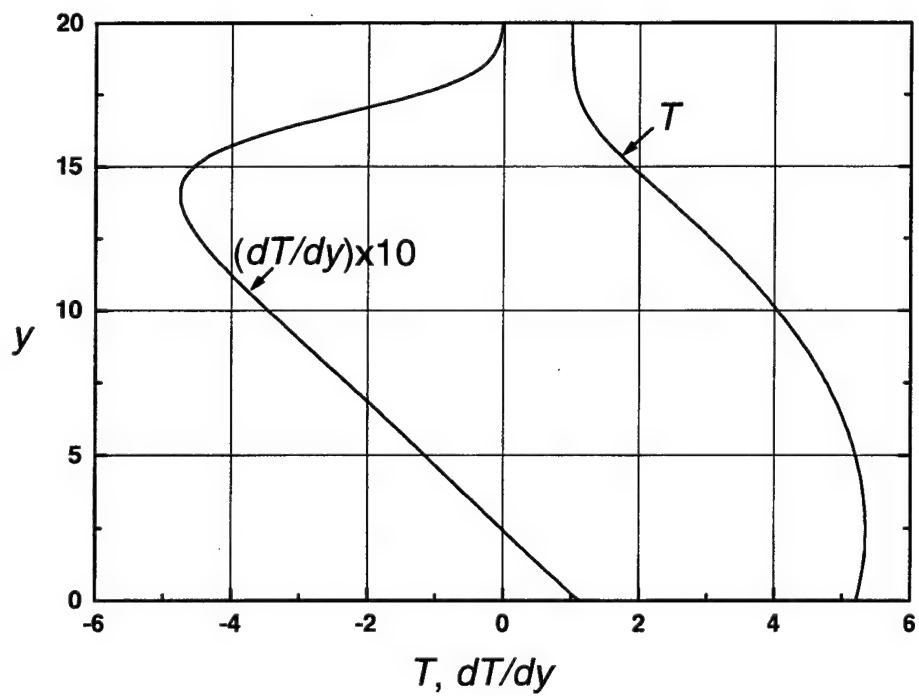
Fig. 4 Mean-flow temperature profiles $T(y)$, and dT/dy.

48
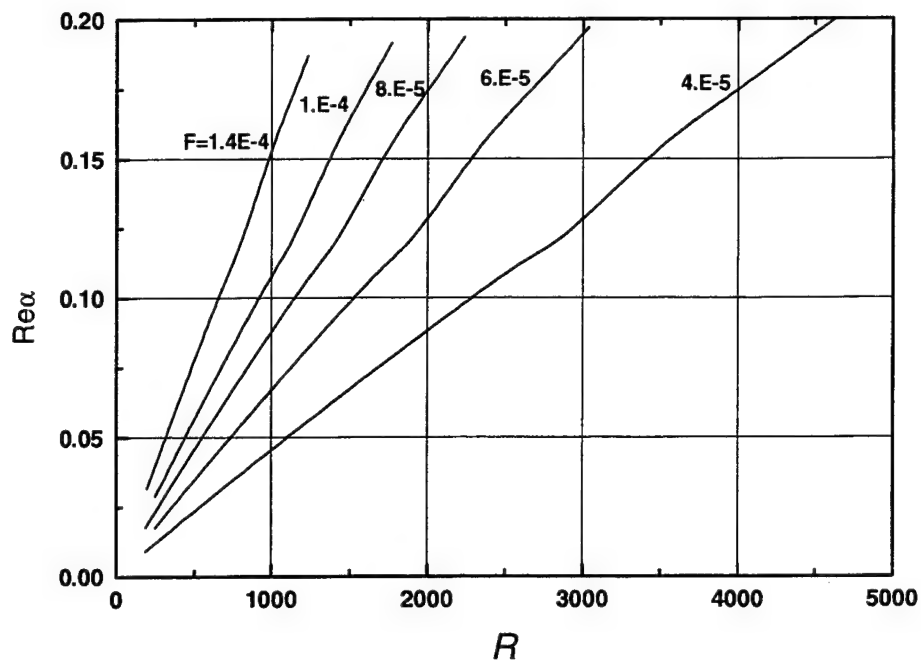
Fig. 5 Second-mode eigenvalues $\text{Re}(\alpha_2)$ as a function of Reynolds number at various frequencies.
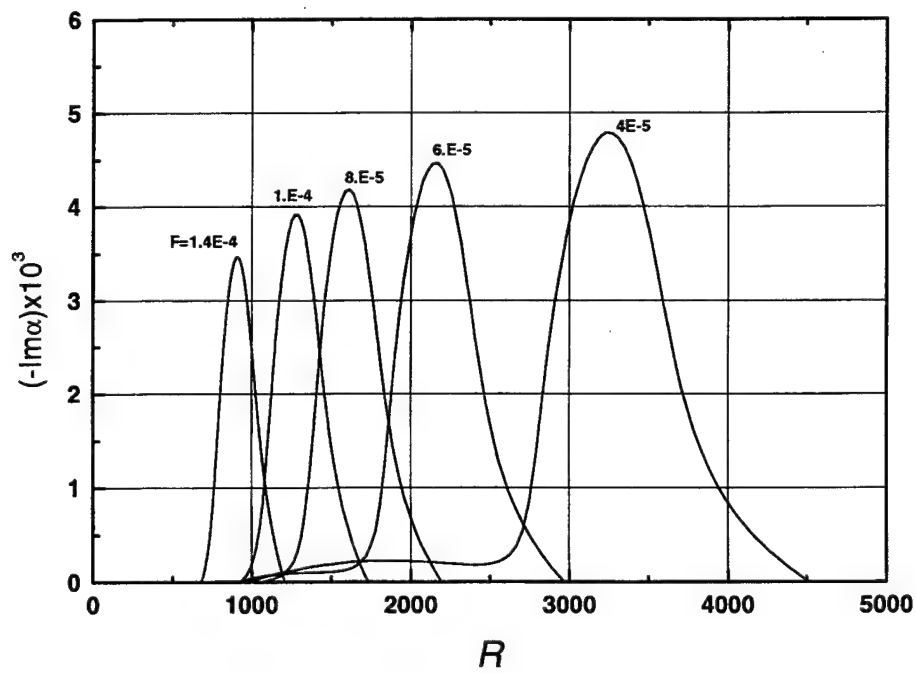

Fig. 6 Second-mode growth rate $-\text{Im}(\alpha_2)$ as a function of Reynolds number at various frequencies.
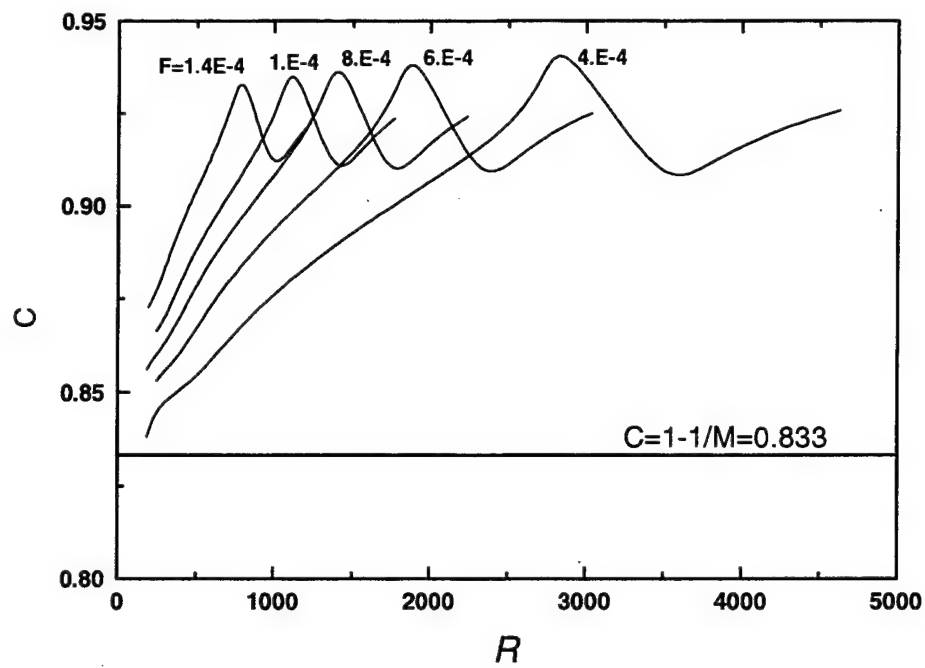
Fig. 7 Second-mode phase speed as a function of Reynolds number at various frequencies.
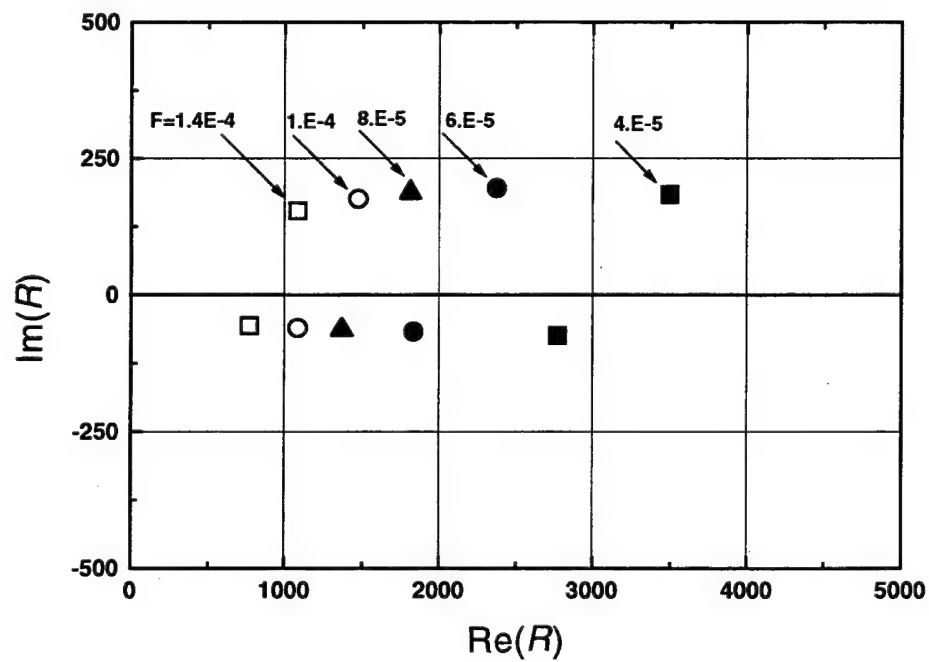
Fig. 8 Branch points in complex R-plane at various frequencies.

50
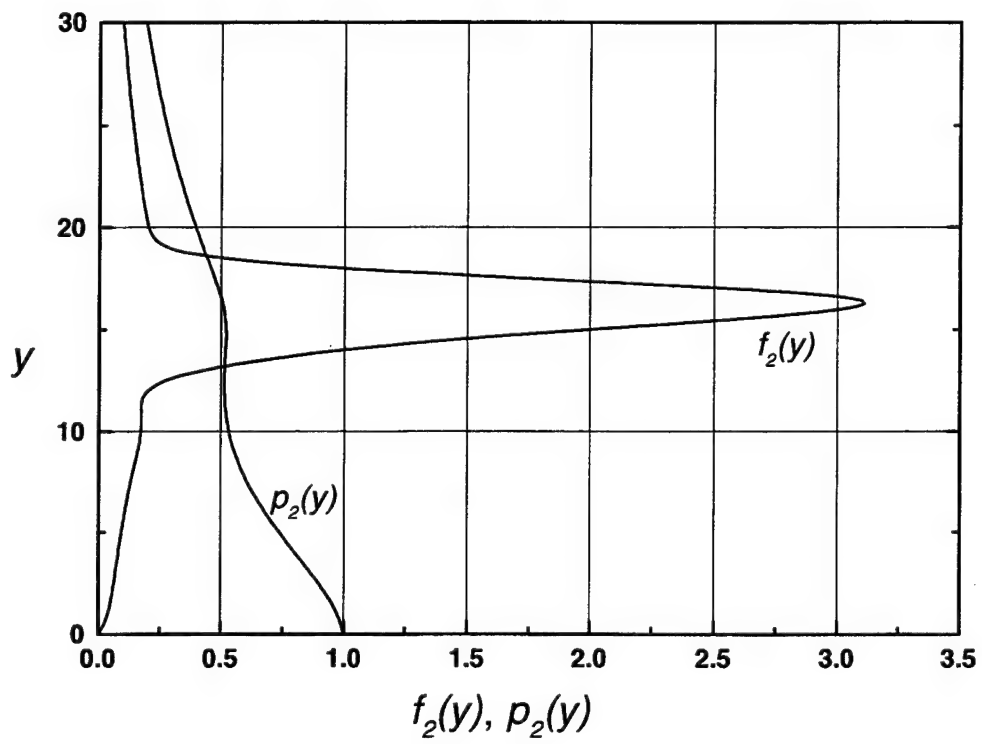
Fig. 9 Second-mode eigenfunctions for pressure $p_2(y)$ and streamwise mass flux $f_2(y)$ near lower neutral curve: $R = 1000$, $F = 8. \times 10^{-5}$.
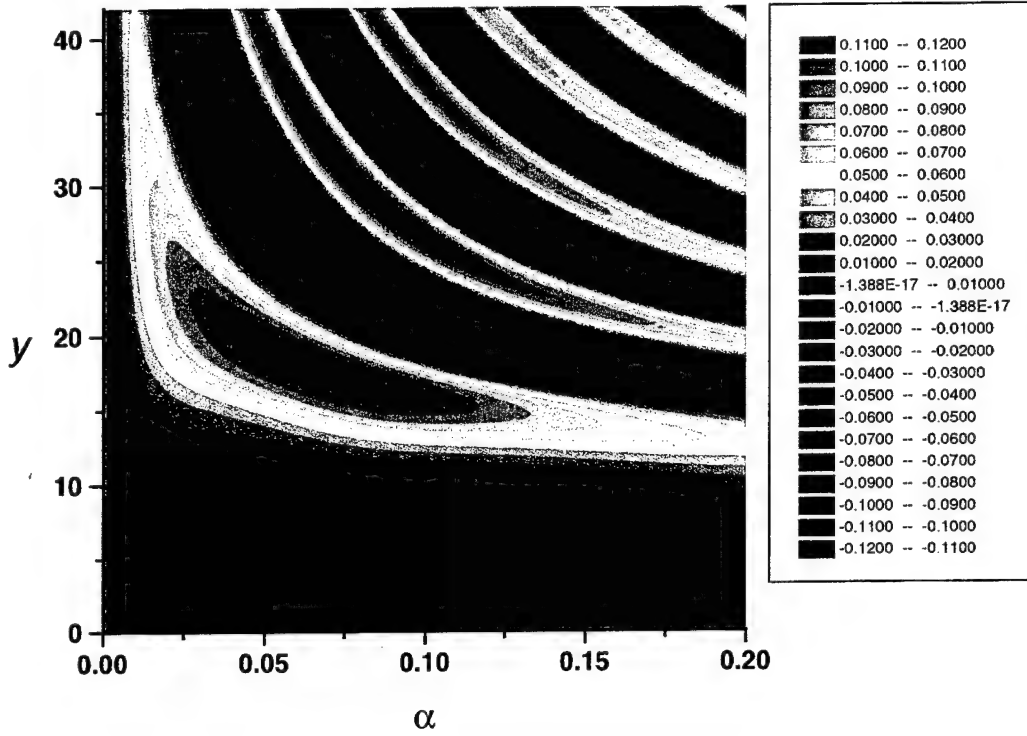
Fig. 10 Contours $\mathrm{Re}(p_w(y,\alpha_w)) = const$ for wall-induced disturbances; $R = 1000$.
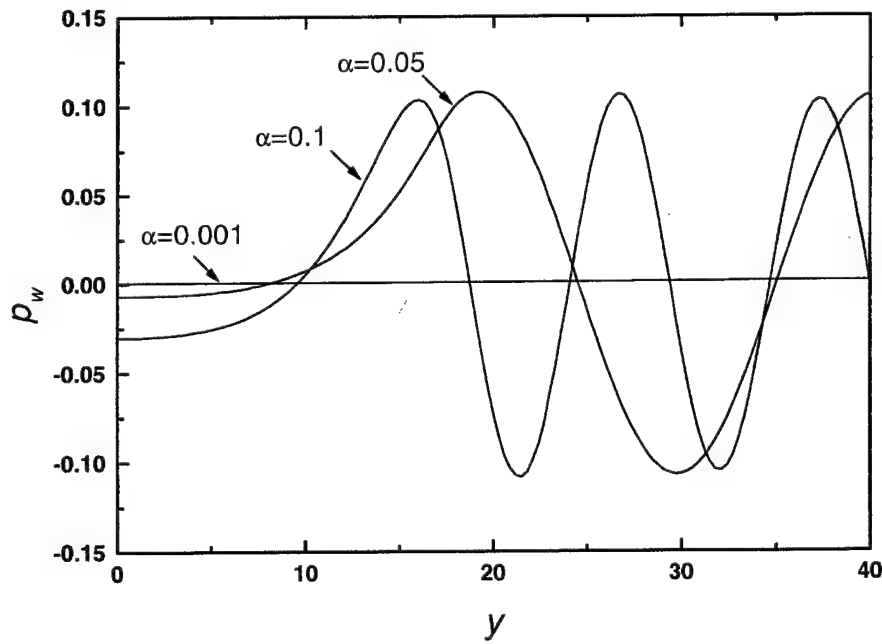

Fig. 11 Distributions $\mathrm{Re}(p_w(y))$ for wall-induced perturbation at various wavenumbers $\alpha = \alpha_w$; $R = 1000$.
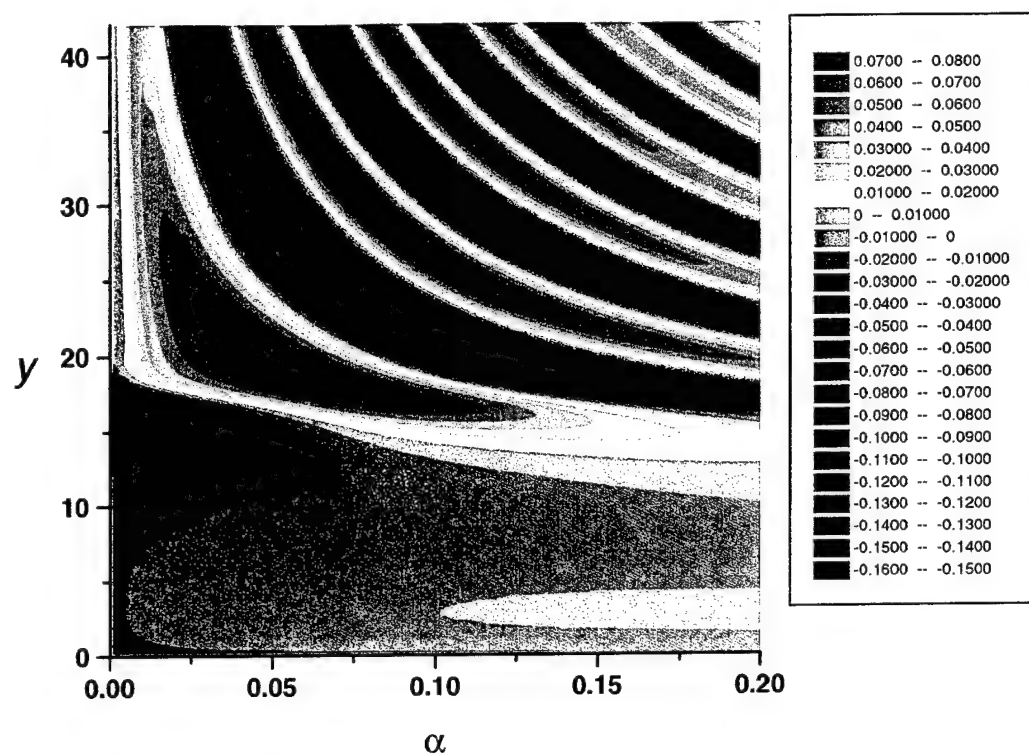
Fig. 12 Contours $\text{Re}(f_w(y,\alpha_w)) = const$ for wall-induced disturbace; $R = 1000$.
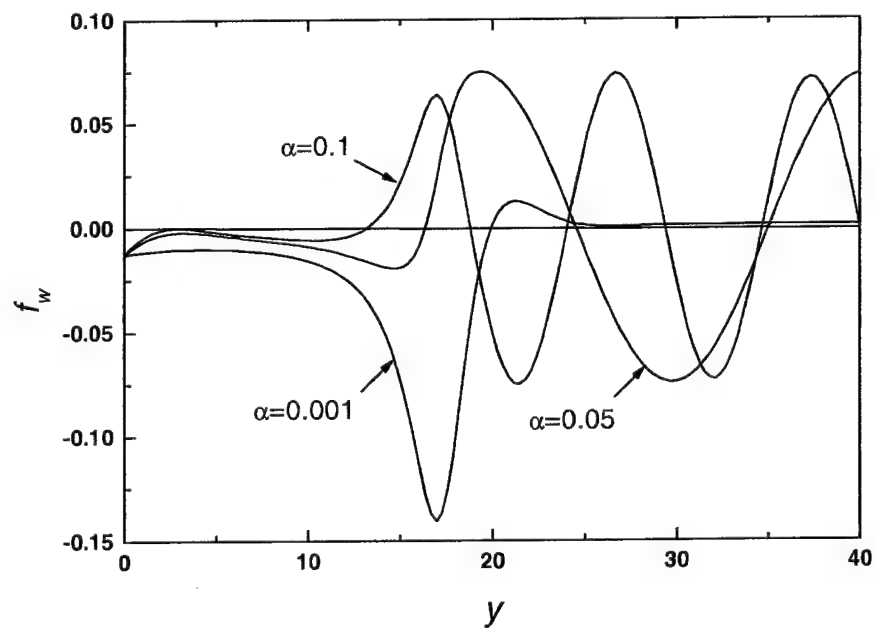

Fig. 13 Mass-flux distributions $\text{Re}(f_w(y))$ for wall-induced perturbation at various wavenumbers $\alpha = \alpha_w$; $R = 1000$.
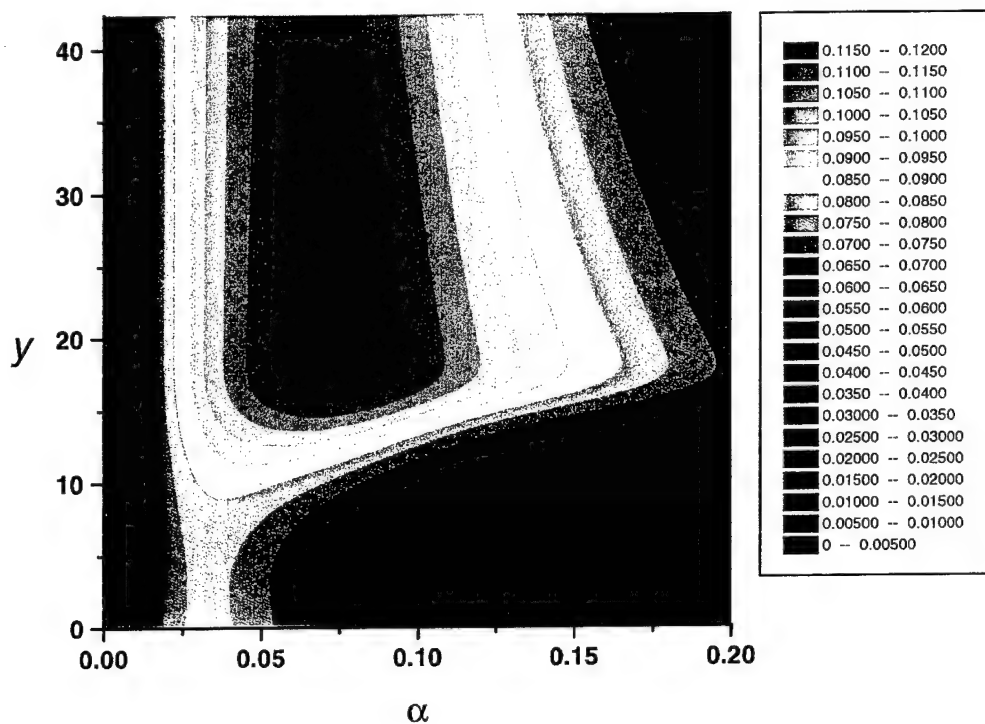
Fig. 14 Pressure amplitude contours $\left| p_w(y,\alpha) \right| = const$; $R = 1000$.
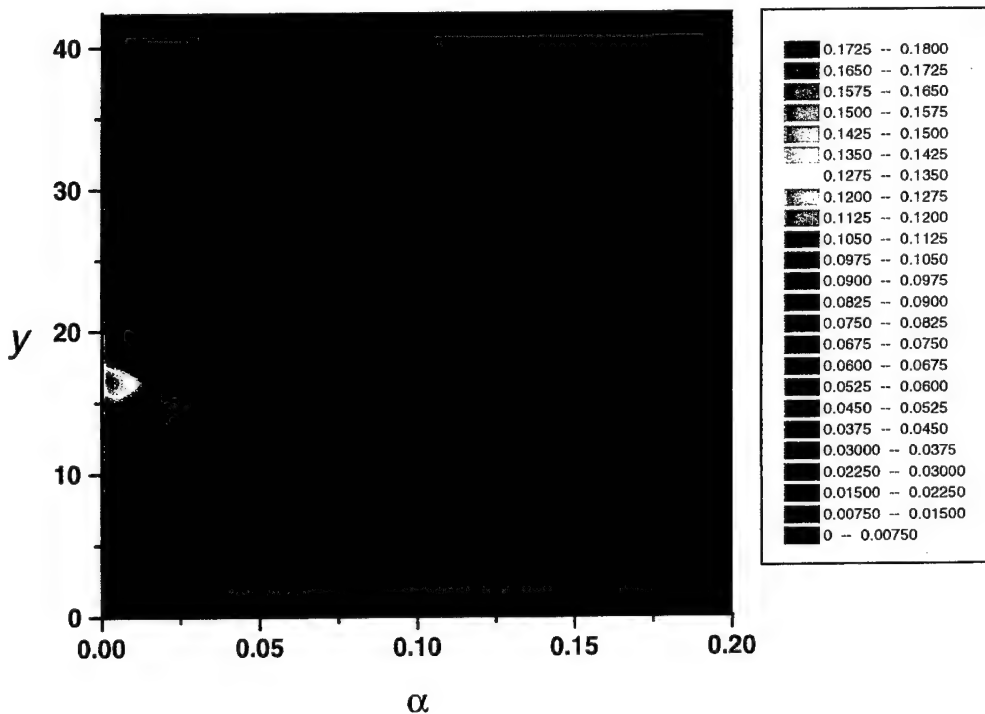

Fig. 15 Mass-flux amplitude contours $\left| f_w(y,\alpha) \right| = const$; $R = 1000$.
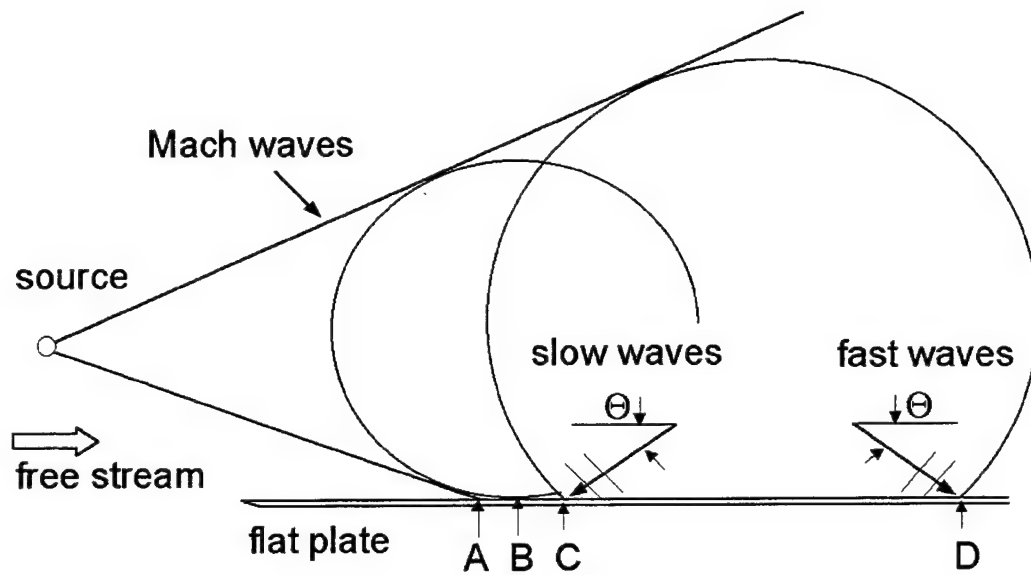
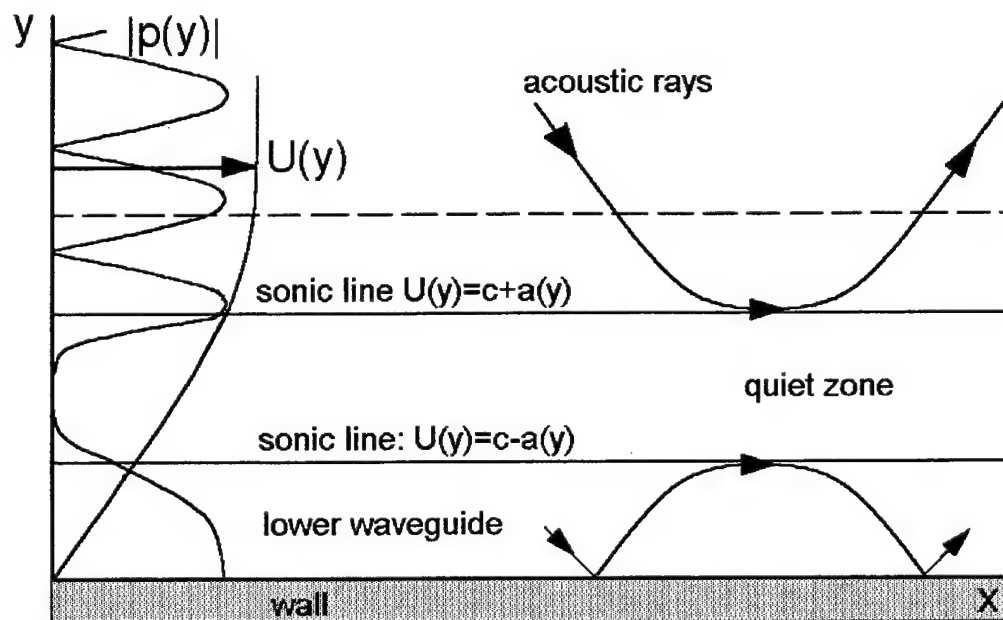Fig. 16 Acoustic waves from cylindrical source.

Fig. 17 Scheme of the acoustic wave-boundary layer interaction.

Fig. 18 Contours of pressure amplitude $\left|p_a(y,\Theta)\right| = const$ for slow waves; $R = 1000$, $F = 8.\times 10^{-5}$.

Fig. 19 Distributions $\left|p_a(y,\Theta)\right|$ at various incidence angles for slow waves, $R = 1000$, $F = 8.\times 10^{-5}$.

Fig. 20 Contours of mass-flux amplitude $\left|f_a(y,\Theta)\right| = const$ for slow waves; $R = 1000$, $F = 8.\times10^{-5}$.

Fig. 21 Distributions $\left|f_a(y,\Theta)\right|$ at various incidence angles for slow waves $R = 1000$, $F = 8.\times10^{-5}$.

57
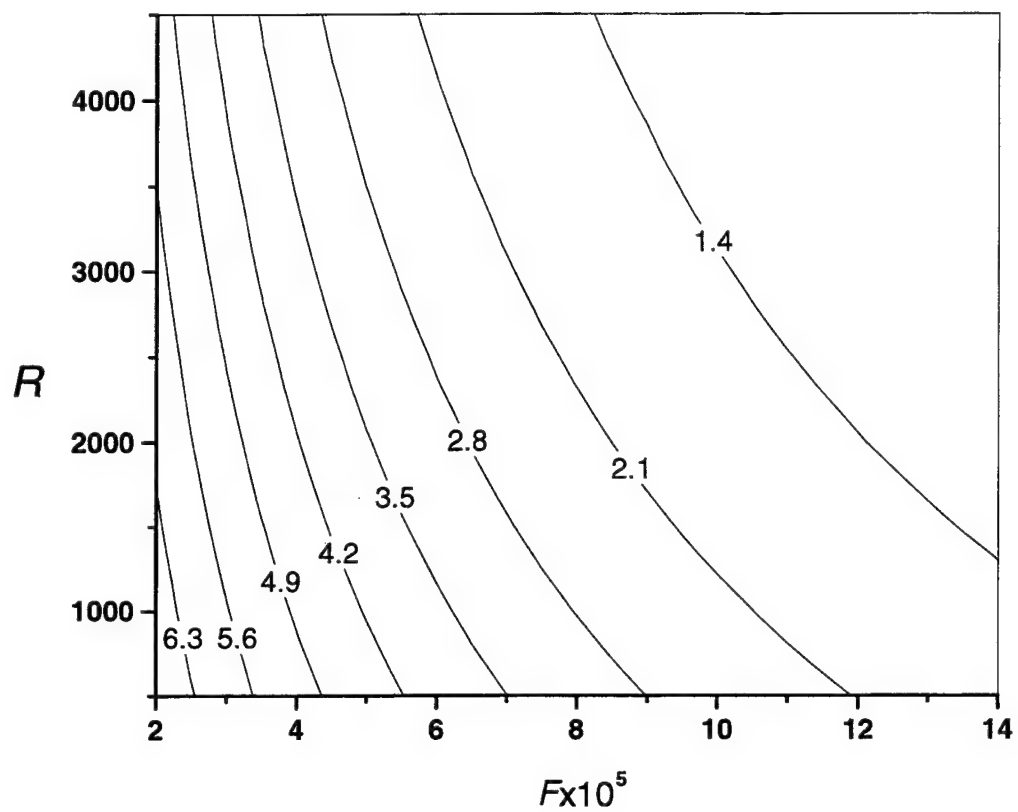
Fig. 22 Contours $\max_{y}\left|f_a(y, R, F)\right| = const$ for slow waves at $\Theta = 40°$.
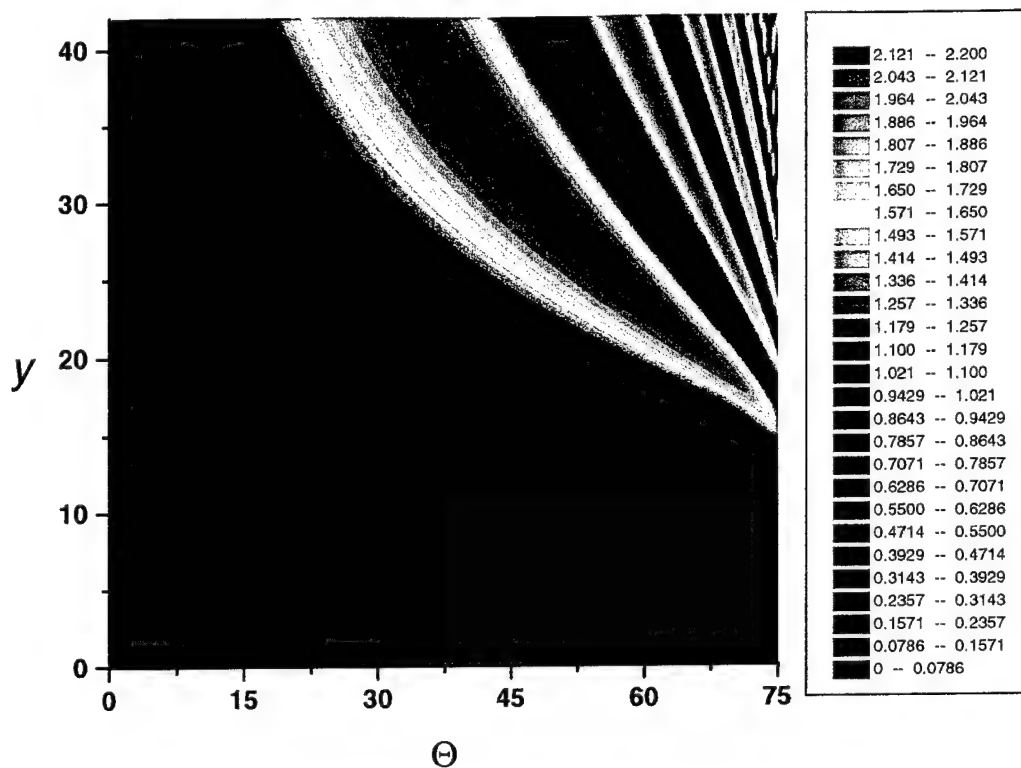
Fig. 23 Contours of pressure amplitude $\left|p_a(y,\Theta)\right| = const$ for fast waves; $R = 1000$, $F = 8.\times 10^{-5}$.
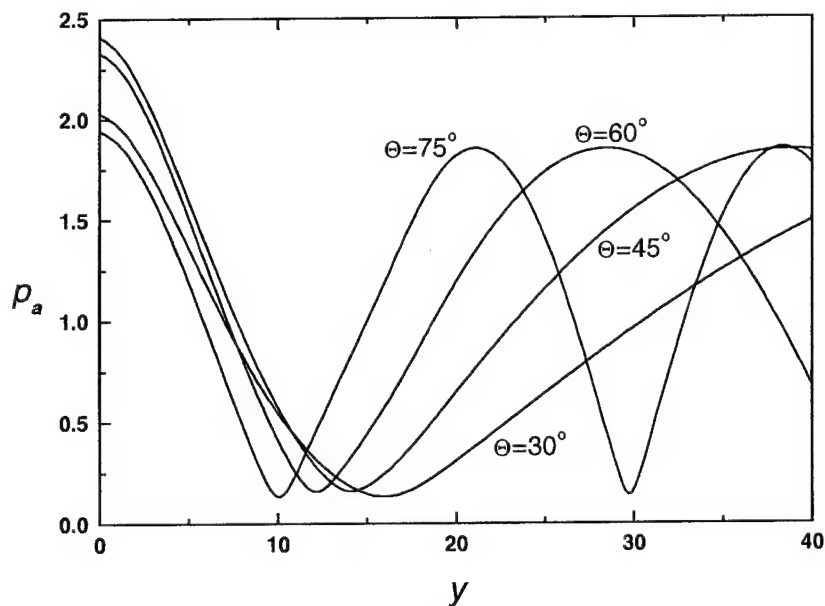
Fig. 24 Distributions $\left|p_a(y,\Theta)\right|$ at various incidence angles for fast waves, $R = 1000$, $F = 8.\times 10^{-5}$.

59
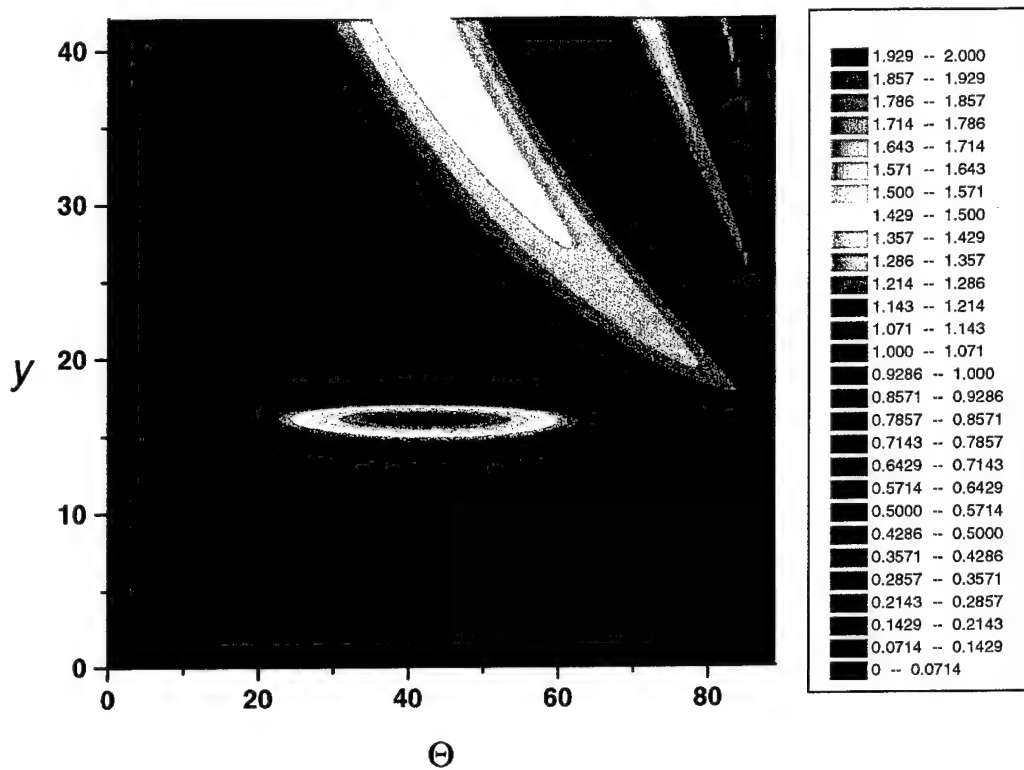
Fig. 25 Contours of mass-flux amplitude $\left|f_a(y,\Theta)\right| = const$ for fast waves; $R = 1000$, $F = 8.\times10^{-5}$.
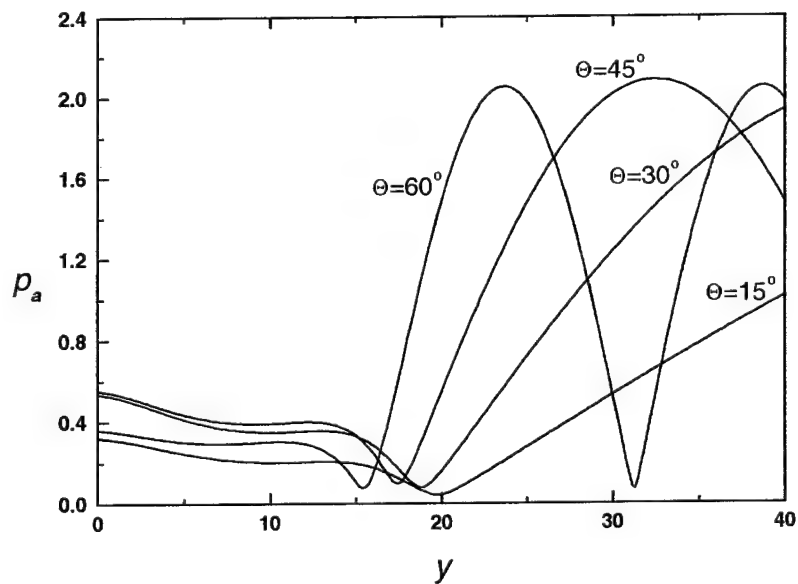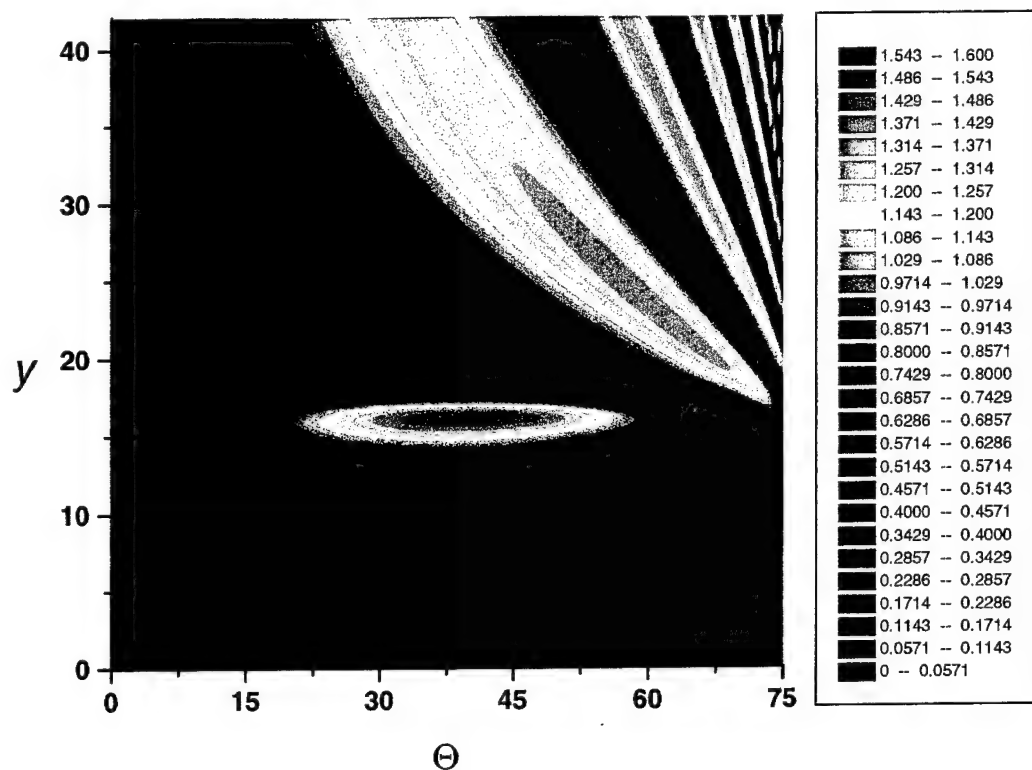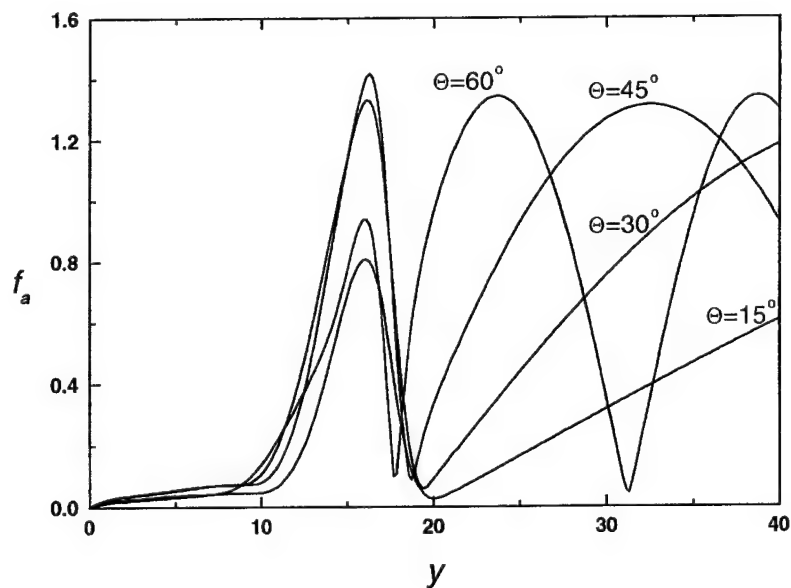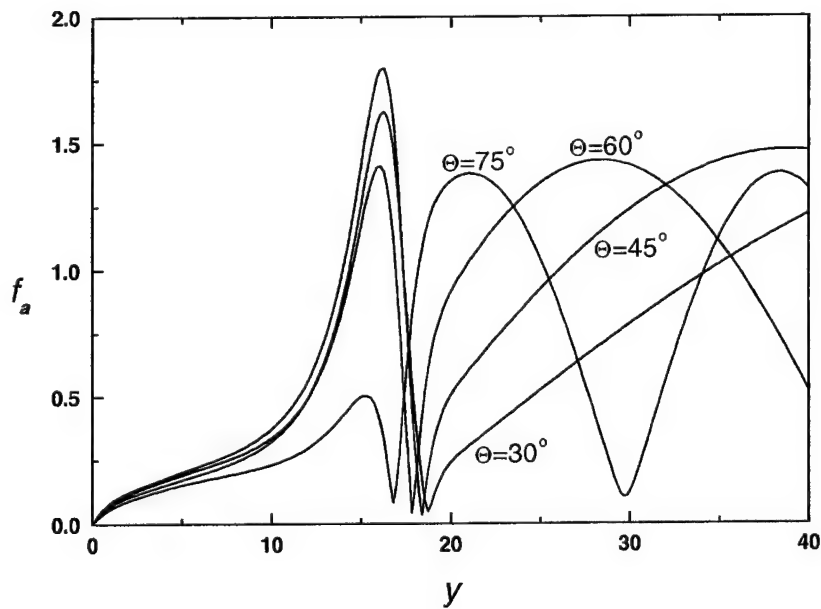

Fig. 26 Mass-flux amplitude distributions $\left|f_a(y,\Theta)\right|$ at various incidence angles for fast waves; $R = 1000$, $F = 8.\times10^{-5}$.

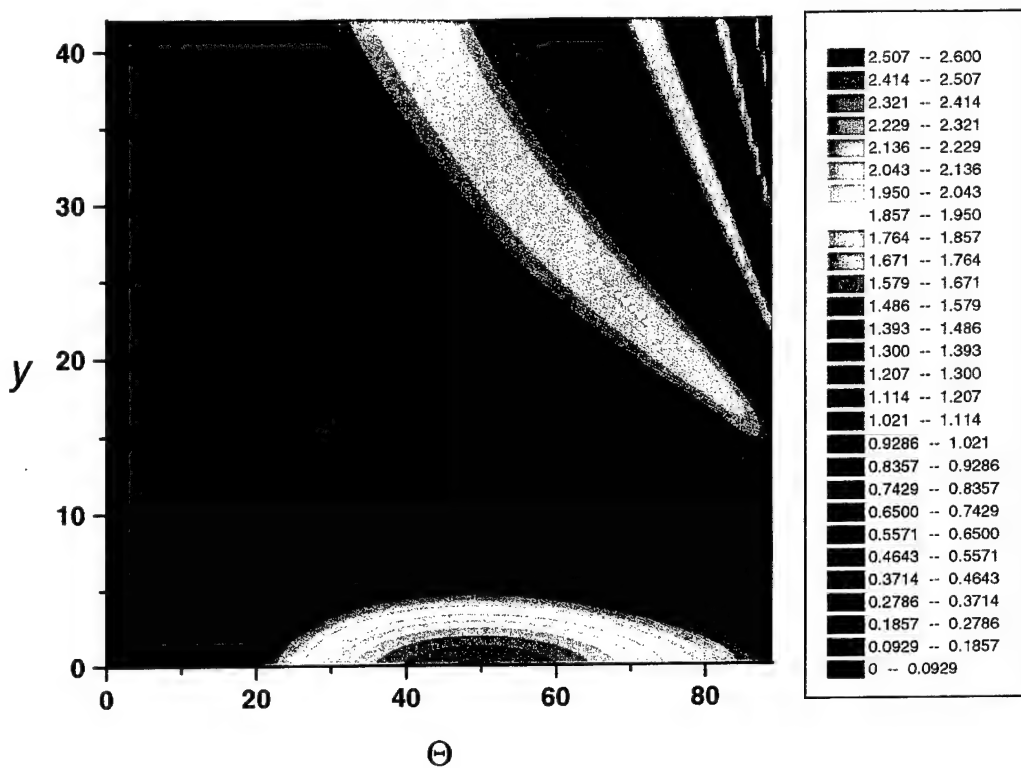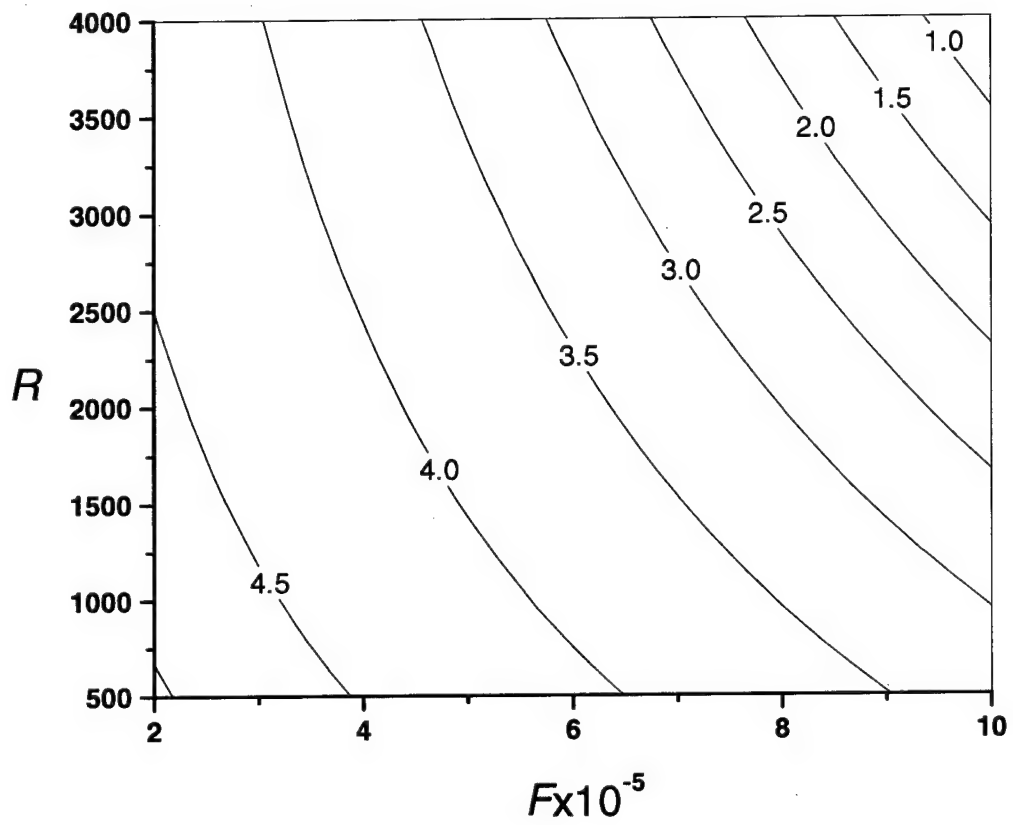Fig. 27 Contours $\max_{y}|f_a(y, R, F)| = const$ for fast waves at $\Theta = 45°$.

Fig. 28a Distributed receptivity function for slow acoustic waves; $F = 4. \times 10^{-5}$.

■	2.132 -- 2.600
	1.748 -- 2.132
	1.433 -- 1.748
	1.175 -- 1.433
	0.9632 -- 1.175
	0.7897 -- 0.9632
	0.6475 -- 0.7897
	0.5309 -- 0.6475
	0.4352 -- 0.5309
	0.3568 -- 0.4352
	0.2926 -- 0.3568
	0.2399 -- 0.2926
	0.1967 -- 0.2399
	0.1612 -- 0.1967
	0.1322 -- 0.1612
	0.1084 -- 0.1322
	0.0889 -- 0.1084
	0.0729 -- 0.0889
	0.0597 -- 0.0729
	0.0490 -- 0.0597
	0.0402 -- 0.0490
	0.0329 -- 0.0402
	0.02699 -- 0.0329
	0.02213 -- 0.02699
	0.01814 -- 0.02213
	0.01488 -- 0.01814
	0.01220 -- 0.01488
	0.01000 -- 0.01220

Fig. 28b Contours $G_{p,dis}(\Theta, R) = const$ for slow acoustic waves; $F = 4. \times 10^{-5}$.

62

Fig. 29a Distributed receptivity function for slow acoustic waves; $F = 6. \times 10^{-5}$.

■	1.860 – 2.200
■	1.573 – 1.860
■	1.330 – 1.573
▨	1.124 – 1.330
▨	0.9504 – 1.124
▨	0.8035 – 0.9504
▨	0.6793 – 0.8035
□	0.5743 – 0.6793
▨	0.4856 – 0.5743
▨	0.4105 – 0.4856
■	0.3471 – 0.4105
■	0.2935 – 0.3471
■	0.2481 – 0.2935
■	0.2098 – 0.2481
■	0.1773 – 0.2098
■	0.1499 – 0.1773
■	0.1268 – 0.1499
■	0.1072 – 0.1268
■	0.0906 – 0.1072
■	0.0766 – 0.0906
■	0.0648 – 0.0766
■	0.0548 – 0.0648
■	0.0463 – 0.0548
■	0.0391 – 0.0463
■	0.0331 – 0.0391
■	0.02798 – 0.0331
■	0.02366 – 0.02798
■	0.02000 – 0.02366

Fig. 29b Contours $G_{p,dis}(\Theta, R) = const$ for slow acoustic waves; $F = 6. \times 10^{-5}$.

Fig. 30a Distributed receptivity function for slow acoustic waves; $F = 8. \times 10^{-5}$.
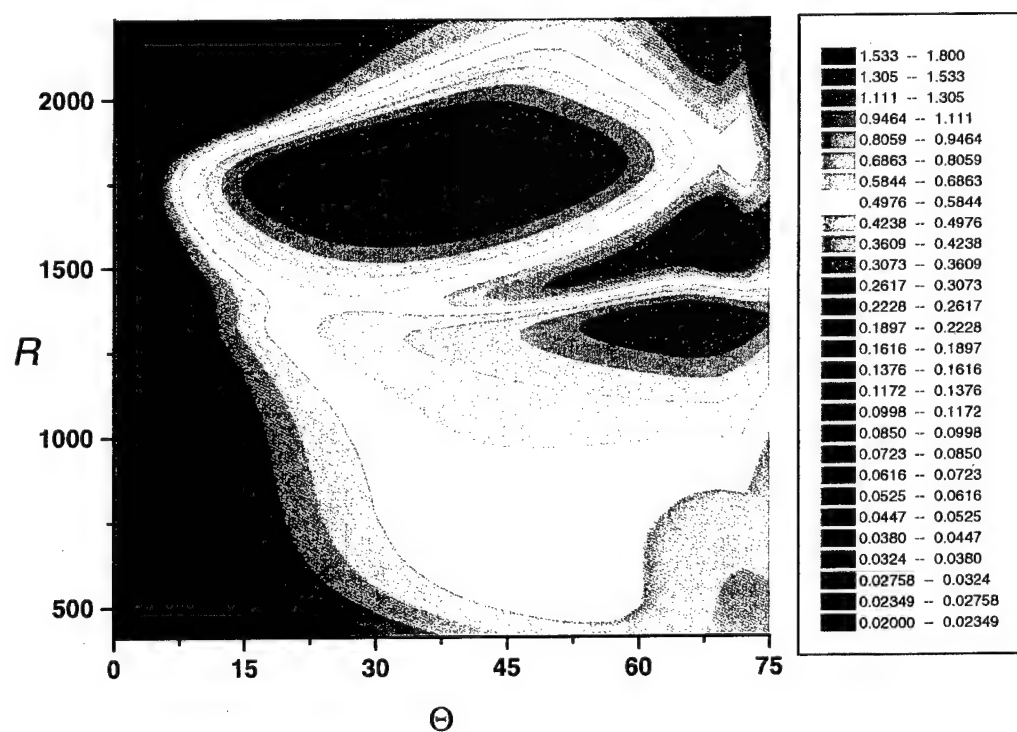
Fig. 30b Contours $G_{p,dis}(\Theta, R) = const$ for slow acoustic waves; $F = 8. \times 10^{-5}$.
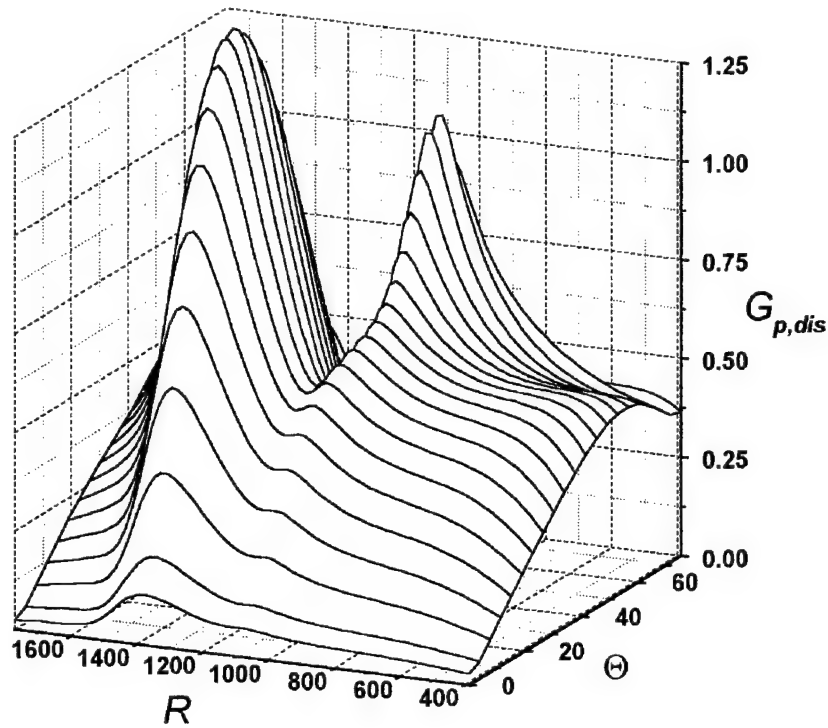
Fig. 31a Distributed receptivity function for slow acoustic waves; $F = 10^{-4}$.

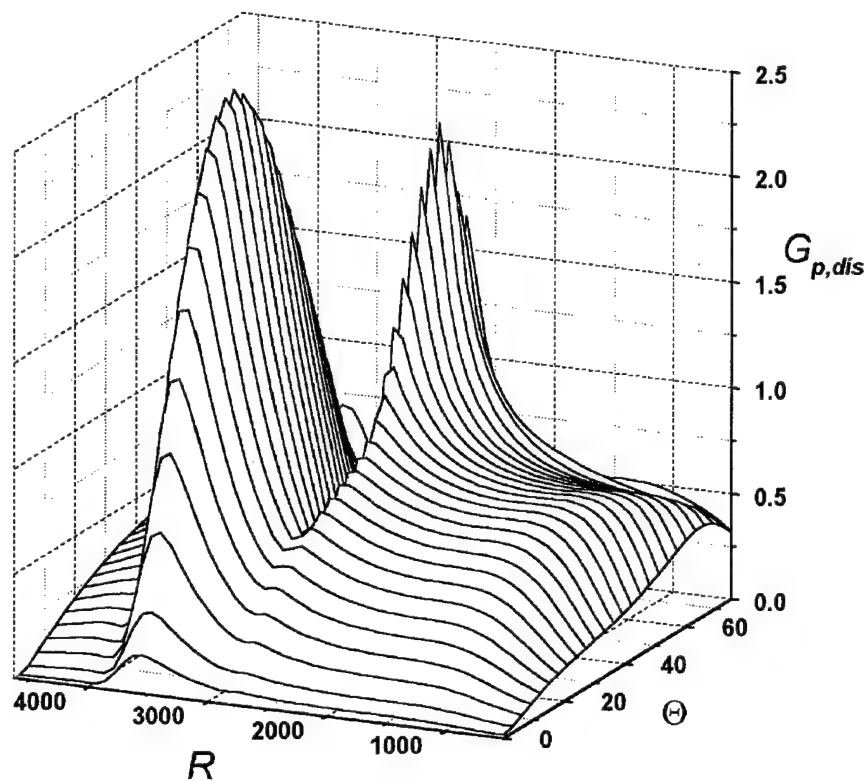Fig. 31b Contours $G_{p,dis}(\Theta, R) = const$ for slow acoustic waves; $F = 10^{-4}$.

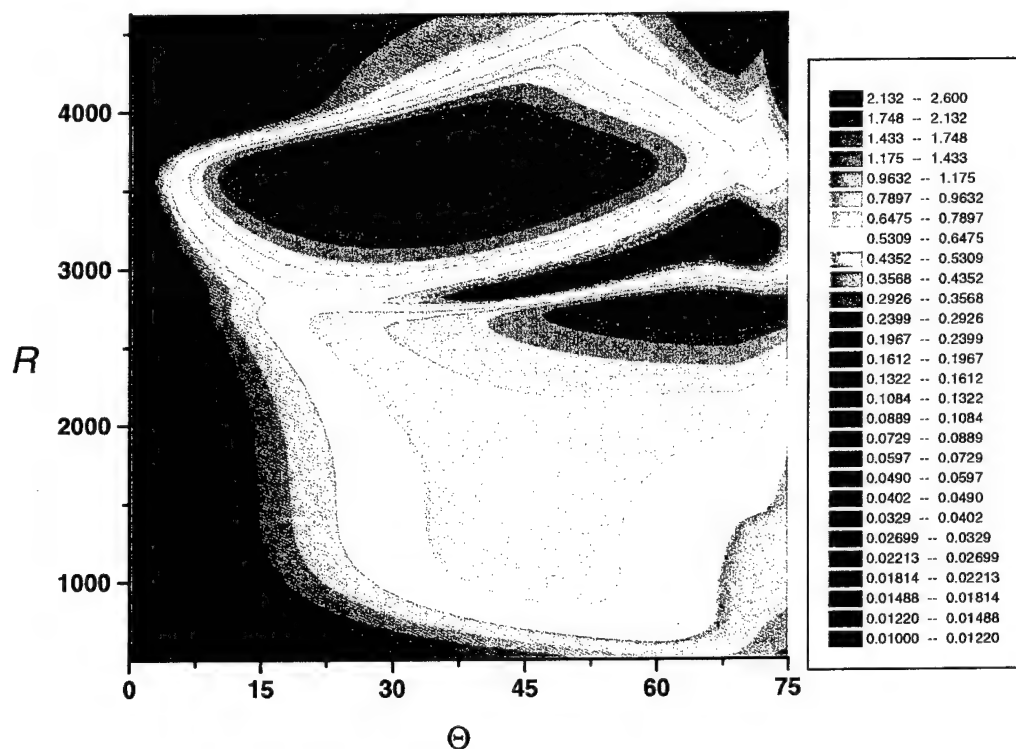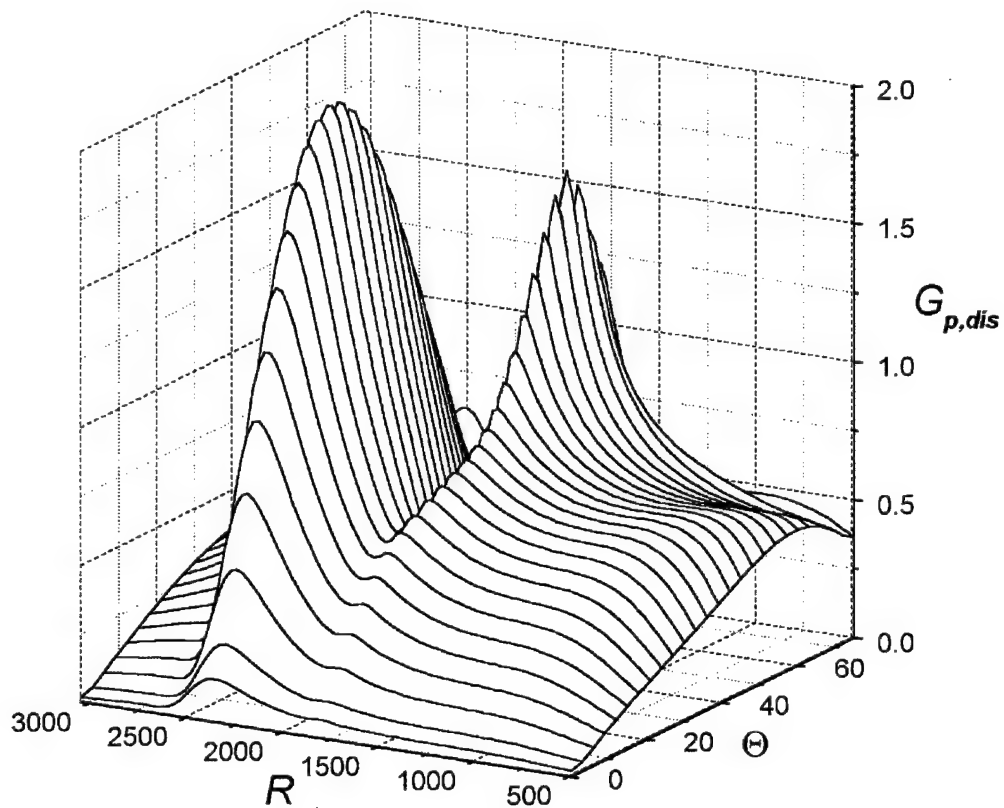Fig. 32a Distributed receptivity function for fast acoustic waves; $F = 4. \times 10^{-5}$.

Fig. 32b Contours $G_{p,dis}(\Theta, R) = const$ for fast acoustic waves; $F = 4. \times 10^{-5}$.

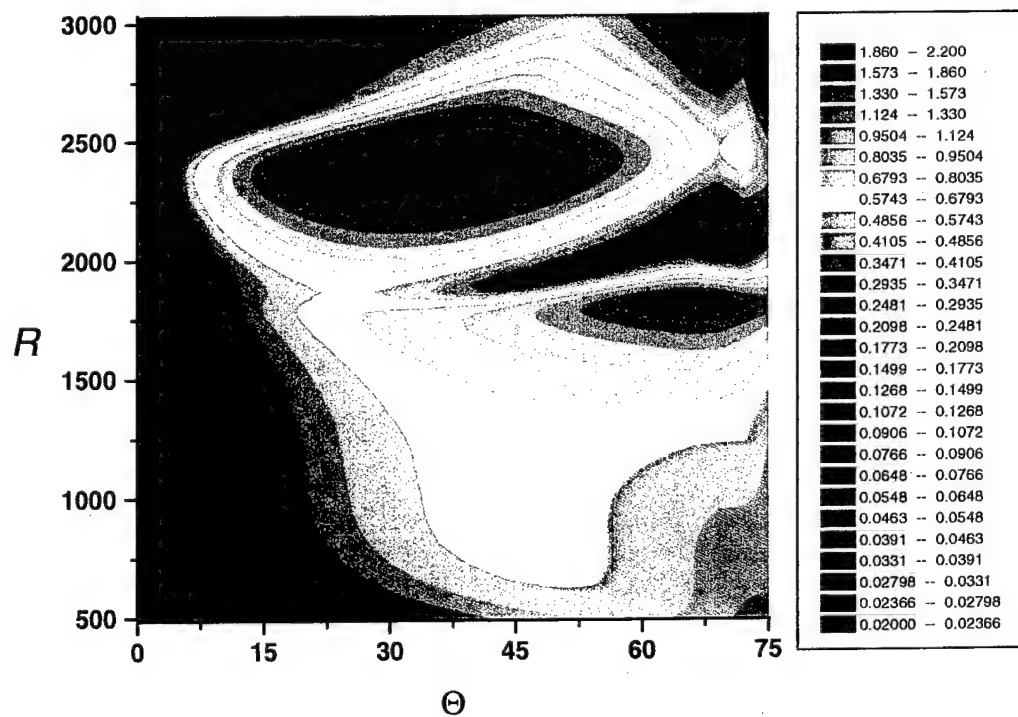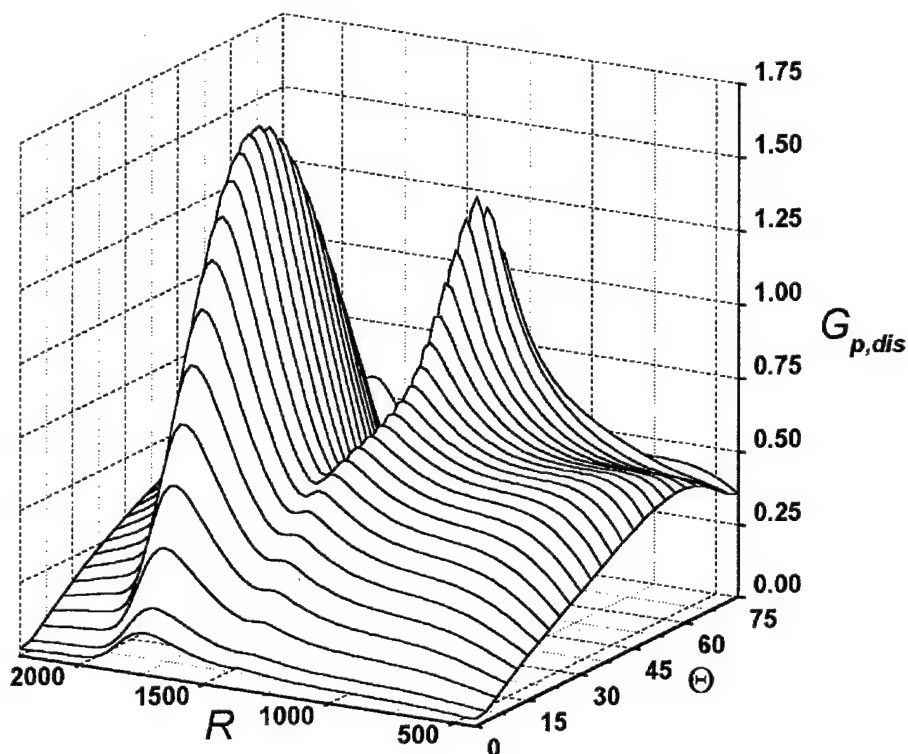Fig. 33a Distributed receptivity function for fast acoustic waves; $F = 6. \times 10^{-5}$.

Fig. 33b Contours $G_{p,dis}(\Theta, R) = const$ for fast acoustic waves; $F = 6. \times 10^{-5}$.
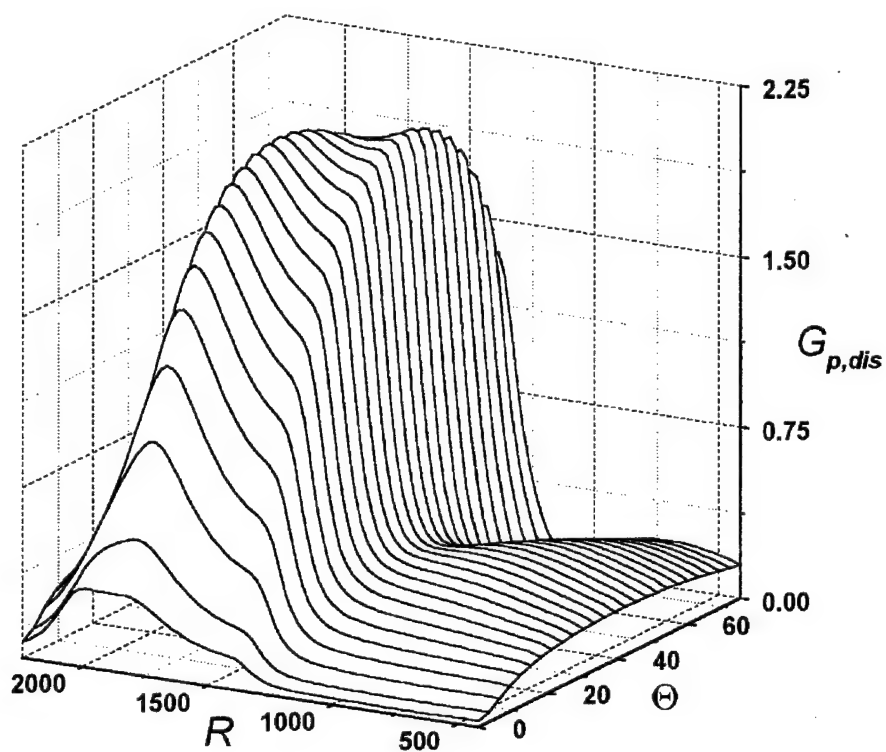
67

Fig. 34a Distributed receptivity function for fast acoustic waves; $F = 8. \times 10^{-5}$.

|	
■	1.815 -- 2.200
■	1.497 -- 1.815
▨	1.234 -- 1.497
▨	1.018 -- 1.234
▨	0.8397 -- 1.018
▨	0.6926 -- 0.8397
▨	0.5712 -- 0.6926
	0.4711 -- 0.5712
▨	0.3886 -- 0.4711
▨	0.3205 -- 0.3886
■	0.2644 -- 0.3205
■	0.2180 -- 0.2644
■	0.1798 -- 0.2180
■	0.1483 -- 0.1798
■	0.1223 -- 0.1483
■	0.1009 -- 0.1223
■	0.0832 -- 0.1009
■	0.0686 -- 0.0832
■	0.0566 -- 0.0686
■	0.0467 -- 0.0566
■	0.0385 -- 0.0467
■	0.0318 -- 0.0385
■	0.02620 -- 0.0318
■	0.02161 -- 0.02620
■	0.01782 -- 0.02161
■	0.01470 -- 0.01782
■	0.01212 -- 0.01470
■	0.01000 -- 0.01212

Fig. 34b Contours $G_{p,dis}(\Theta, R) = const$ for fast acoustic waves; $F = 8. \times 10^{-5}$.

68

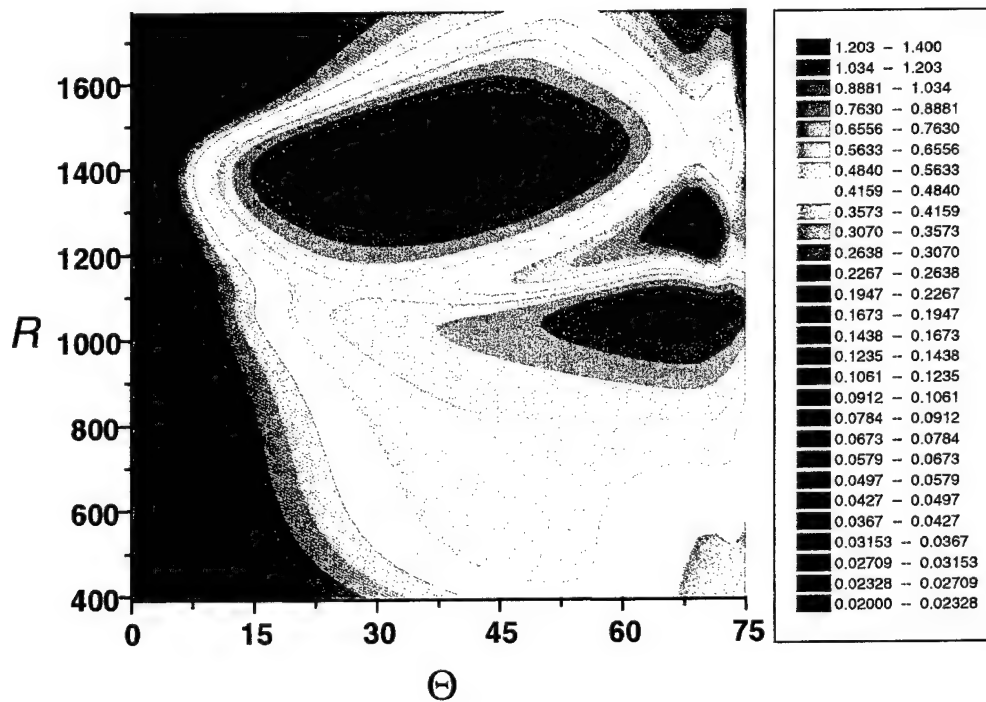Fig. 35a Distributed receptivity function for fast acoustic waves; $F = 10^{-4}$.
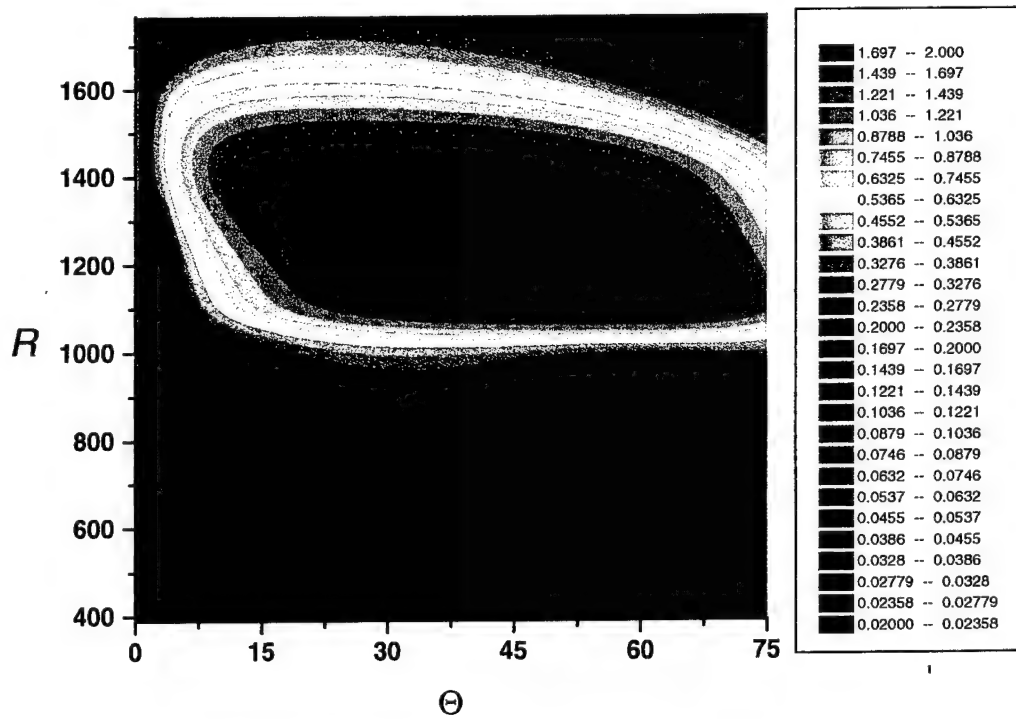
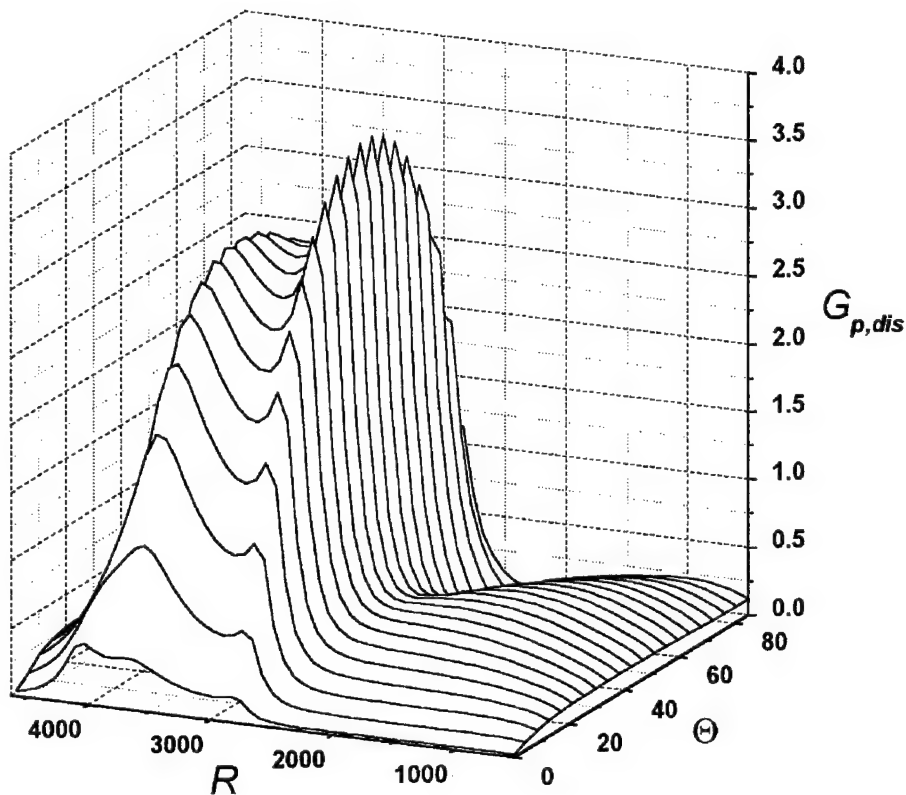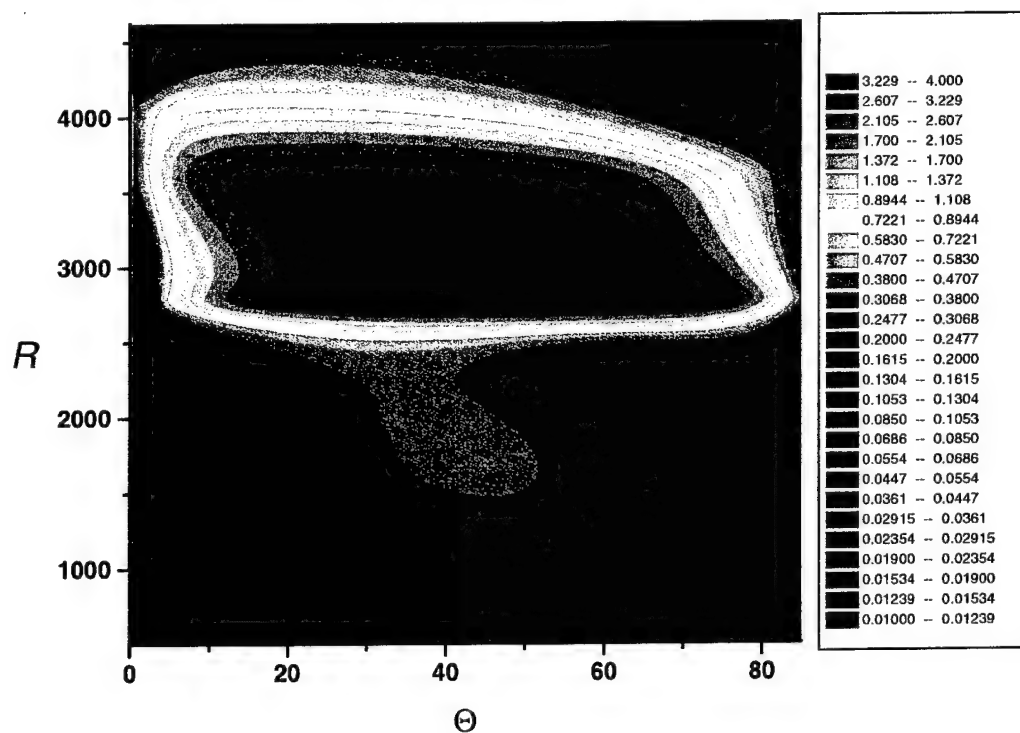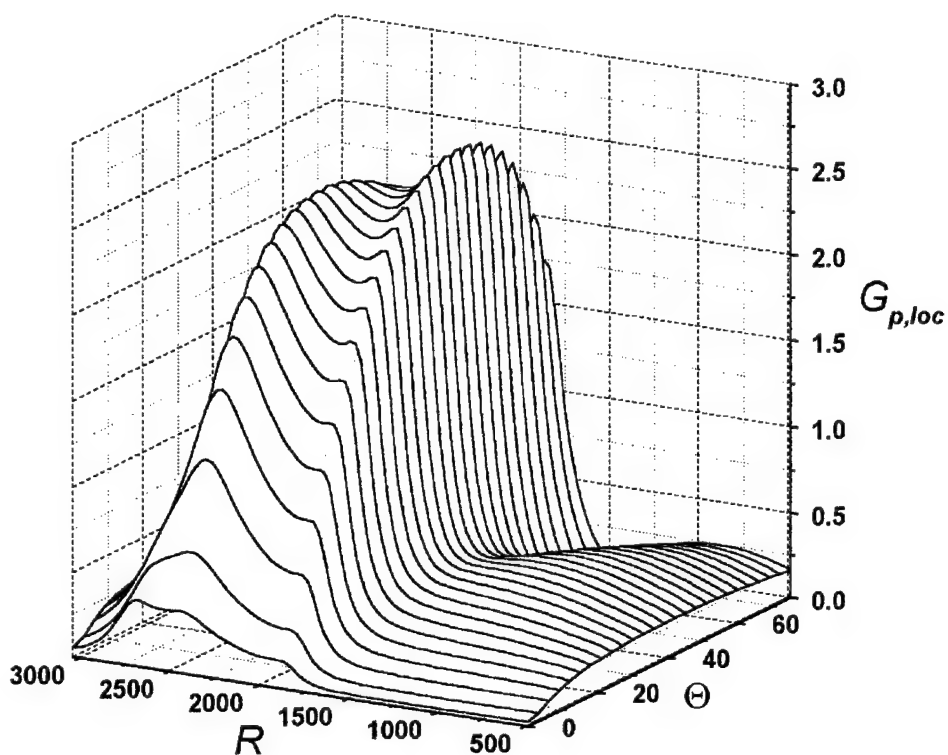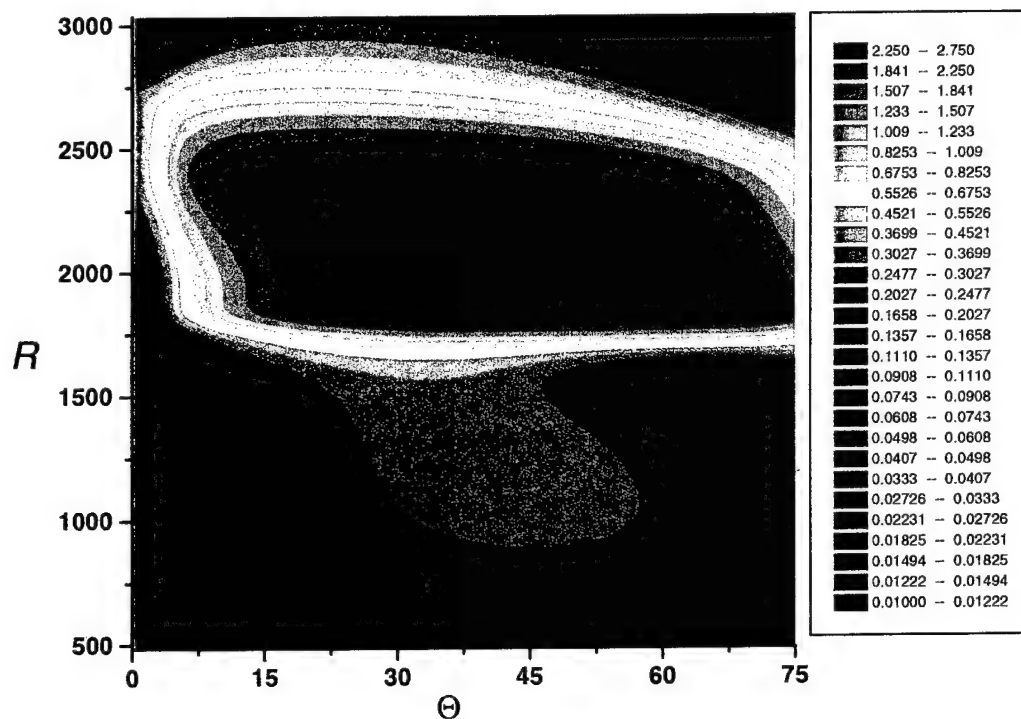Fig. 35b Contours $G_{p,dis}(\Theta, R) = const$ for fast acoustic waves; $F = 10^{-4}$.

Fig. 36a Local receptivity function for slow acoustic waves; $F = 4. \times 10^{-5}$.

0.00400	-- 0.00500
0.00321	-- 0.00400
0.002569	-- 0.00321
0.002058	-- 0.002569
0.001648	-- 0.002058
0.001320	-- 0.001648
0.001057	-- 0.001320
8.469E-4	-- 0.001057
6.783E-4	-- 8.469E-4
5.433E-4	-- 6.783E-4
4.352E-4	-- 5.433E-4
3.486E-4	-- 4.352E-4
2.792E-4	-- 3.486E-4
2.236E-4	-- 2.792E-4
1.791E-4	-- 2.236E-4
1.435E-4	-- 1.791E-4
1.149E-4	-- 1.435E-4
9.203E-5	-- 1.149E-4
7.371E-5	-- 9.203E-5
5.904E-5	-- 7.371E-5
4.729E-5	-- 5.904E-5
3.787E-5	-- 4.729E-5
3.034E-5	-- 3.787E-5
2.43E-5	-- 3.034E-5
1.946E-5	-- 2.43E-5
1.559E-5	-- 1.946E-5
1.249E-5	-- 1.559E-5
1E-5	-- 1.249E-5

Fig. 36b Contours $G_{p,loc}(\Theta, R) = const$ for slow acoustic waves; $F = 4. \times 10^{-5}$.

70
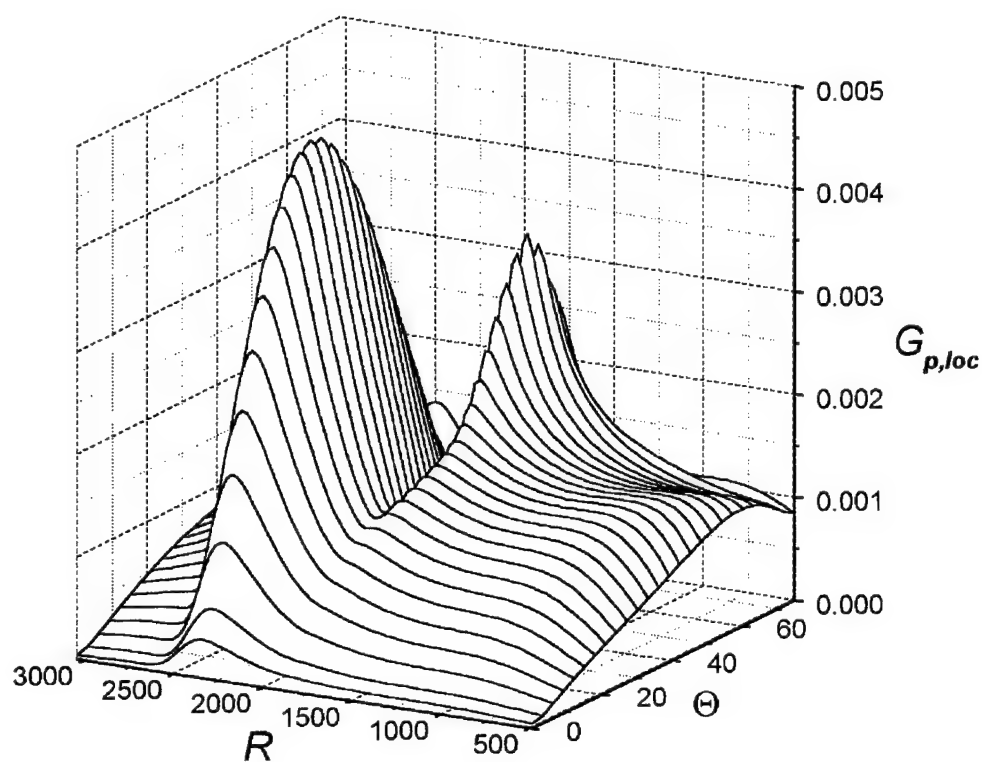
Fig. 37a Local receptivity function for slow acoustic waves; $F = 6. \times 10^{-5}$.
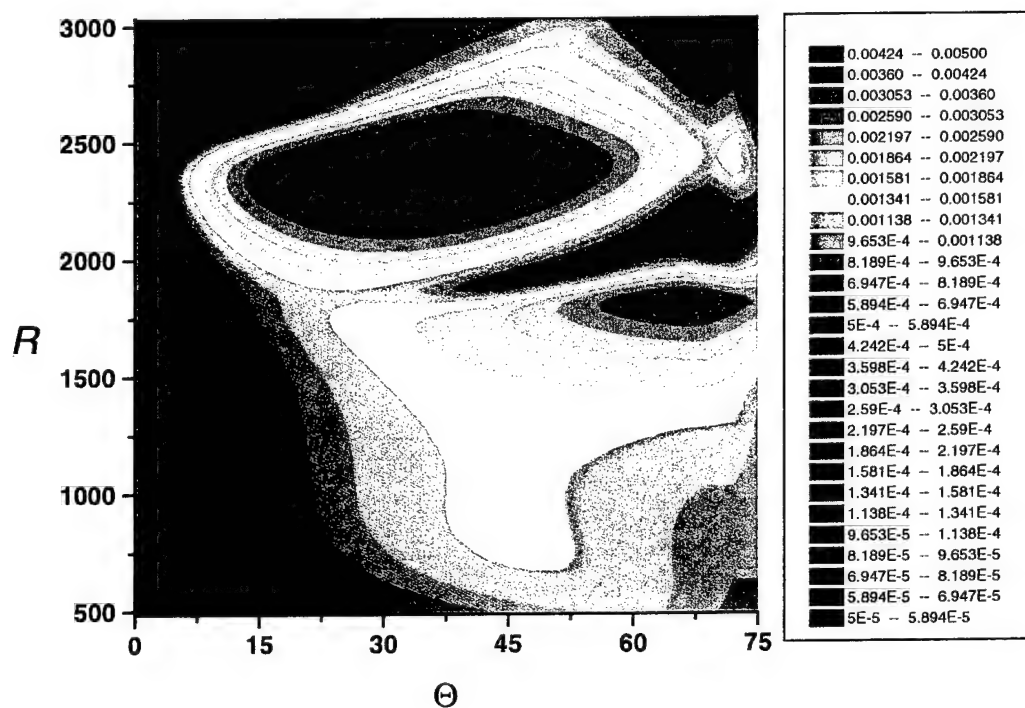
Fig. 37b Contours $G_{p,loc}(\Theta, R) = const$ for slow acoustic waves; $F = 6. \times 10^{-5}$.
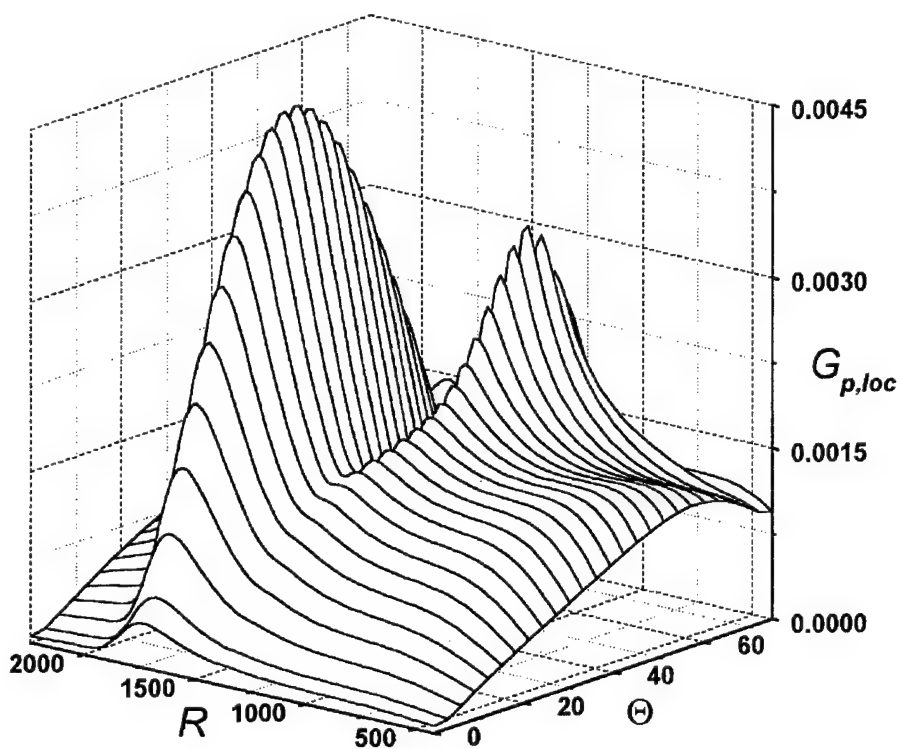
Fig. 38a Local receptivity function for slow acoustic waves; $F = 8. \times 10^{-5}$.
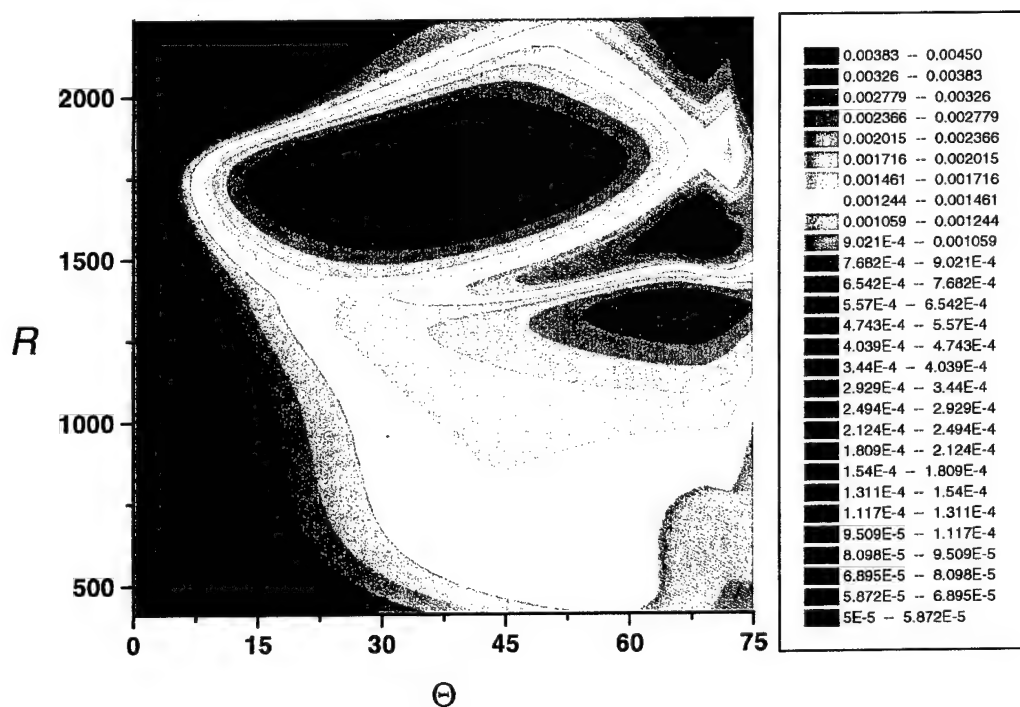
Fig. 38b Contours $G_{p,loc}(\Theta, R) = const$ for slow acoustic waves; $F = 8. \times 10^{-5}$.

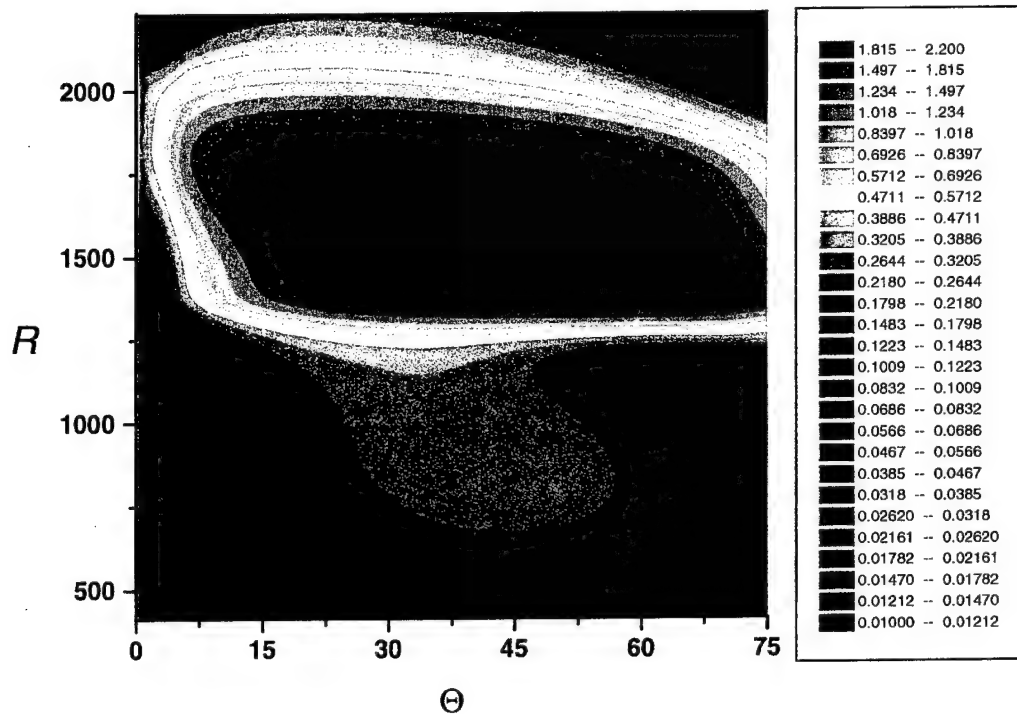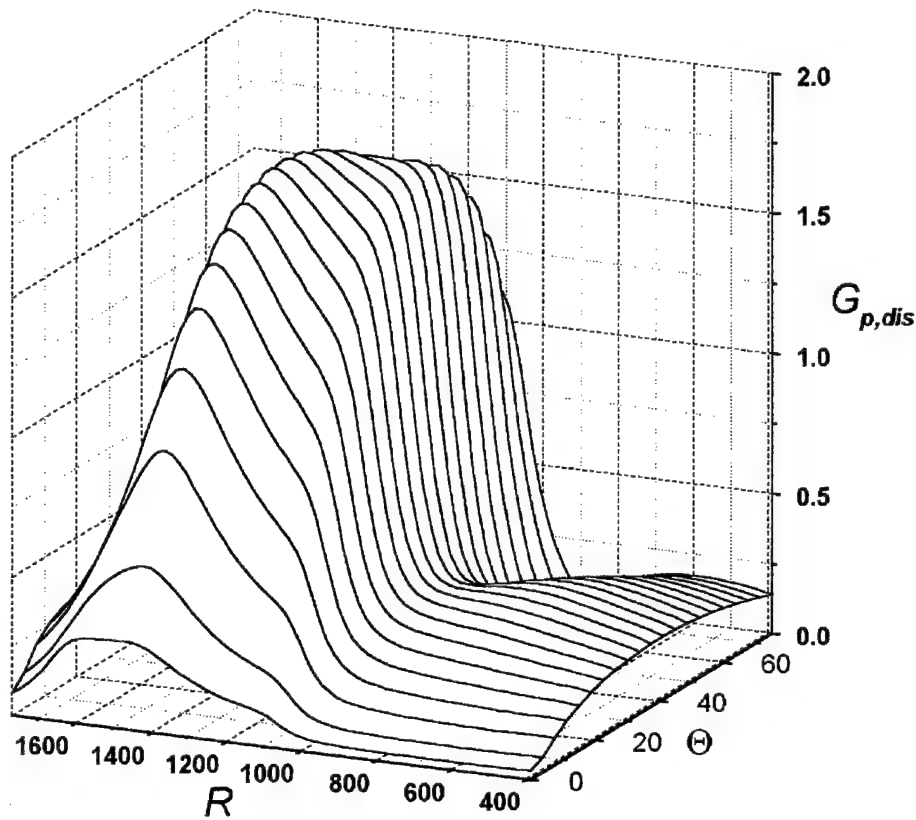Fig. 39a Local receptivity function for slow acoustic waves; $F = 10^{-4}$.

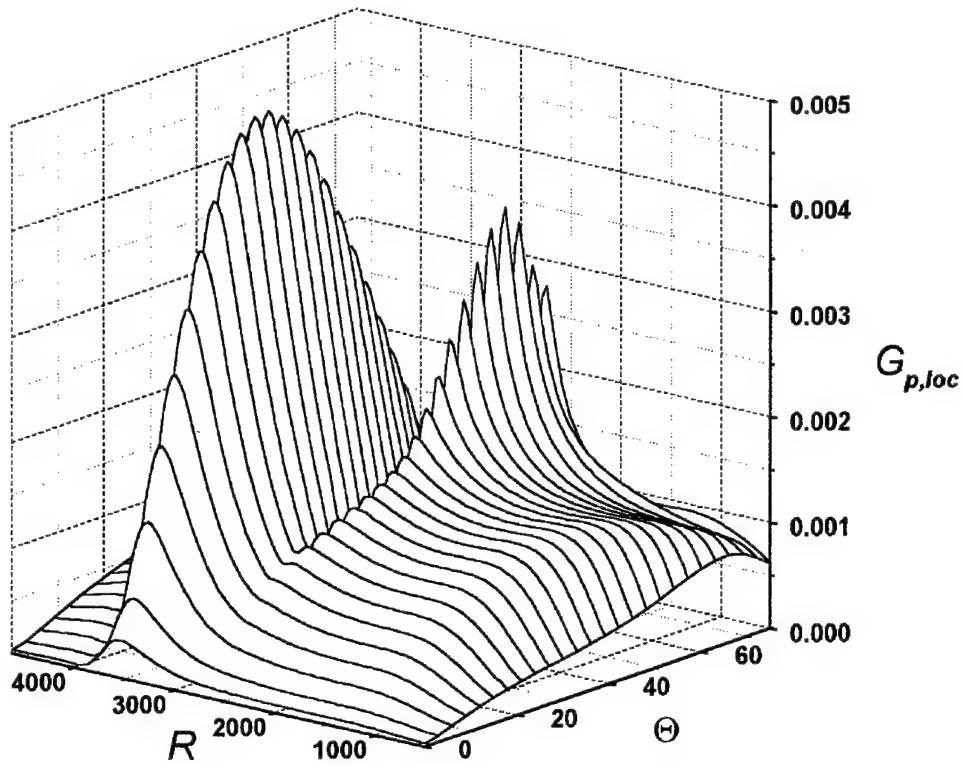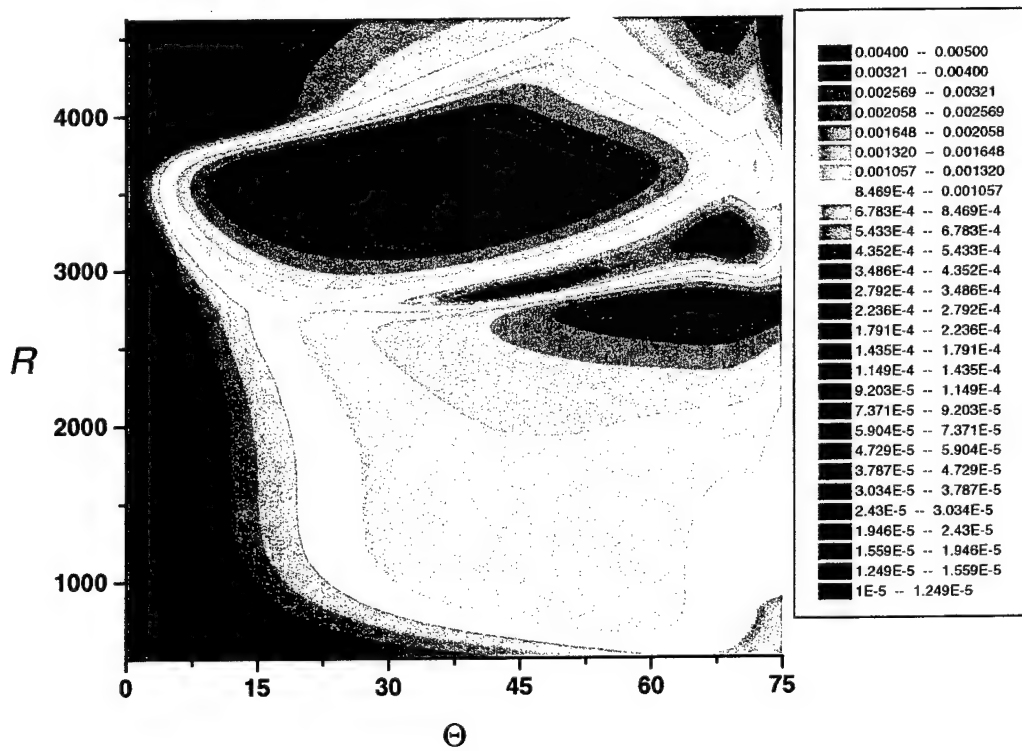|	
	0.00383 -- 0.00450
	0.00326 -- 0.00383
	0.002779 -- 0.00326
	0.002366 -- 0.002779
	0.002015 -- 0.002366
	0.001716 -- 0.002015
	0.001461 -- 0.001716
	0.001244 -- 0.001461
	0.001059 -- 0.001244
	9.021E-4 -- 0.001059
	7.682E-4 -- 9.021E-4
	6.542E-4 -- 7.682E-4
	5.57E-4 -- 6.542E-4
	4.743E-4 -- 5.57E-4
	4.039E-4 -- 4.743E-4
	3.44E-4 -- 4.039E-4
	2.929E-4 -- 3.44E-4
	2.494E-4 -- 2.929E-4
	2.124E-4 -- 2.494E-4
	1.809E-4 -- 2.124E-4
	1.54E-4 -- 1.809E-4
	1.311E-4 -- 1.54E-4
	1.117E-4 -- 1.311E-4
	9.509E-5 -- 1.117E-4
	8.098E-5 -- 9.509E-5
	6.895E-5 -- 8.098E-5
	5.872E-5 -- 6.895E-5
	5E-5 -- 5.872E-5

Fig. 39b Contours $G_{p,loc}(\Theta, R) = const$ for slow acoustic waves; $F = 10^{-4}$.

73

Fig. 40a Local receptivity function for fast acoustic waves; $F = 4. \times 10^{-5}$.

0.00474	-- 0.00576
0.00390	-- 0.00474
0.00321	-- 0.00390
0.002637	-- 0.00321
0.002169	-- 0.002637
0.001784	-- 0.002169
0.001468	-- 0.001784
0.001207	-- 0.001468
9.933E-4	-- 0.001207
8.171E-4	-- 9.933E-4
6.722E-4	-- 8.171E-4
5.529E-4	-- 6.722E-4
4.548E-4	-- 5.529E-4
3.742E-4	-- 4.548E-4
3.078E-4	-- 3.742E-4
2.532E-4	-- 3.078E-4
2.083E-4	-- 2.532E-4
1.713E-4	-- 2.083E-4
1.409E-4	-- 1.713E-4
1.159E-4	-- 1.409E-4
9.538E-5	-- 1.159E-4
7.846E-5	-- 9.538E-5
6.454E-5	-- 7.846E-5
5.309E-5	-- 6.454E-5
4.368E-5	-- 5.309E-5
3.593E-5	-- 4.368E-5
2.956E-5	-- 3.593E-5
2.431E-5	-- 2.956E-5
2E-5	-- 2.431E-5

Fig. 40b Contours $G_{p,loc}(\Theta, R) = const$ for fast acoustic waves; $F = 4. \times 10^{-5}$.

Fig. 41a Local receptivity function for fast acoustic waves; $F = 6.\times10^{-5}$.

|	
	0.00582 -- 0.00700
	0.00484 -- 0.00582
	0.00403 -- 0.00484
	0.00335 -- 0.00403
	0.002783 -- 0.00335
	0.002314 -- 0.002783
	0.001925 -- 0.002314
	0.001600 -- 0.001925
	0.001331 -- 0.001600
	0.001107 -- 0.001331
	9.202E-4 -- 0.001107
	7.652E-4 -- 9.202E-4
	6.363E-4 -- 7.652E-4
	5.292E-4 -- 6.363E-4
	4.4E-4 -- 5.292E-4
	3.659E-4 -- 4.4E-4
	3.043E-4 -- 3.659E-4
	2.53E-4 -- 3.043E-4
	2.104E-4 -- 2.53E-4
	1.75E-4 -- 2.104E-4
	1.455E-4 -- 1.75E-4
	1.21E-4 -- 1.455E-4
	1.006E-4 -- 1.21E-4
	8.366E-5 -- 1.006E-4
	6.956E-5 -- 8.366E-5
	5.785E-5 -- 6.956E-5
	4.81E-5 -- 5.785E-5
	4E-5 -- 4.81E-5

Fig. 41b Contours $G_{p,loc}(\Theta, R) = const$ for fast acoustic waves; $F = 6.\times10^{-5}$.

Fig. 42a Local receptivity function $G_{p,loc}(\Theta, R)$ for fast acoustic waves; $F = 8. \times 10^{-5}$.

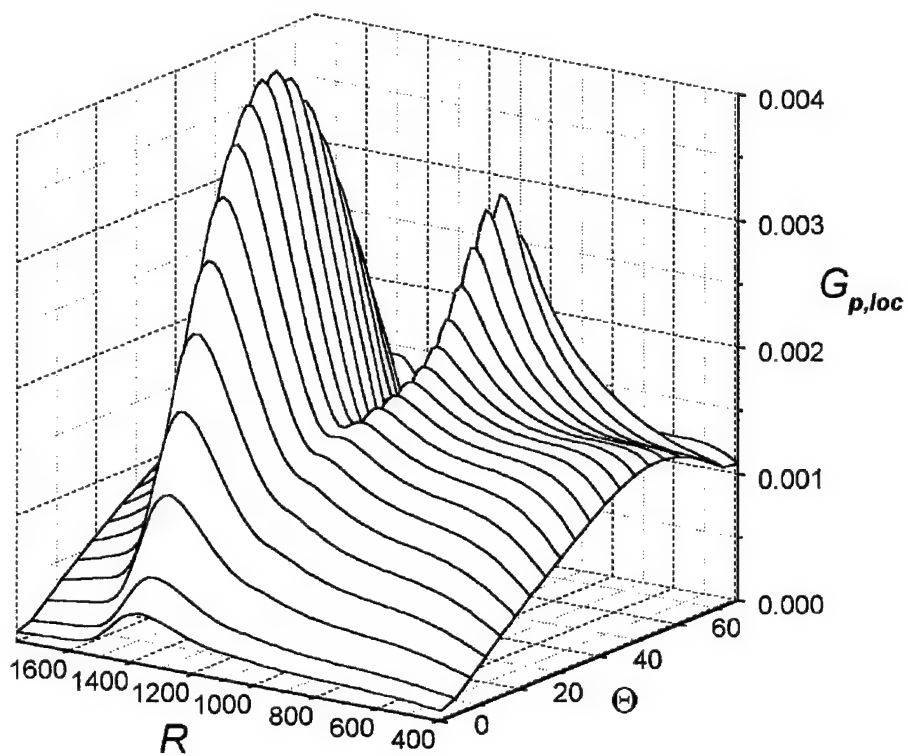Fig. 42b Contours $G_{p,loc}(\Theta, R) = const$ for fast acoustic waves; $F = 8. \times 10^{-5}$.

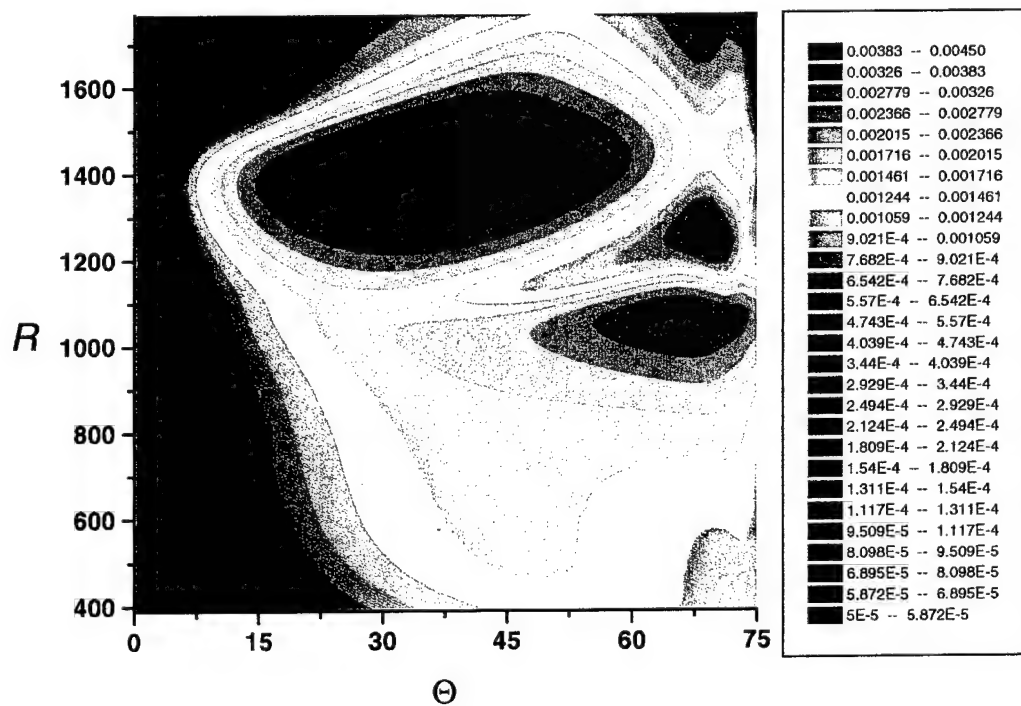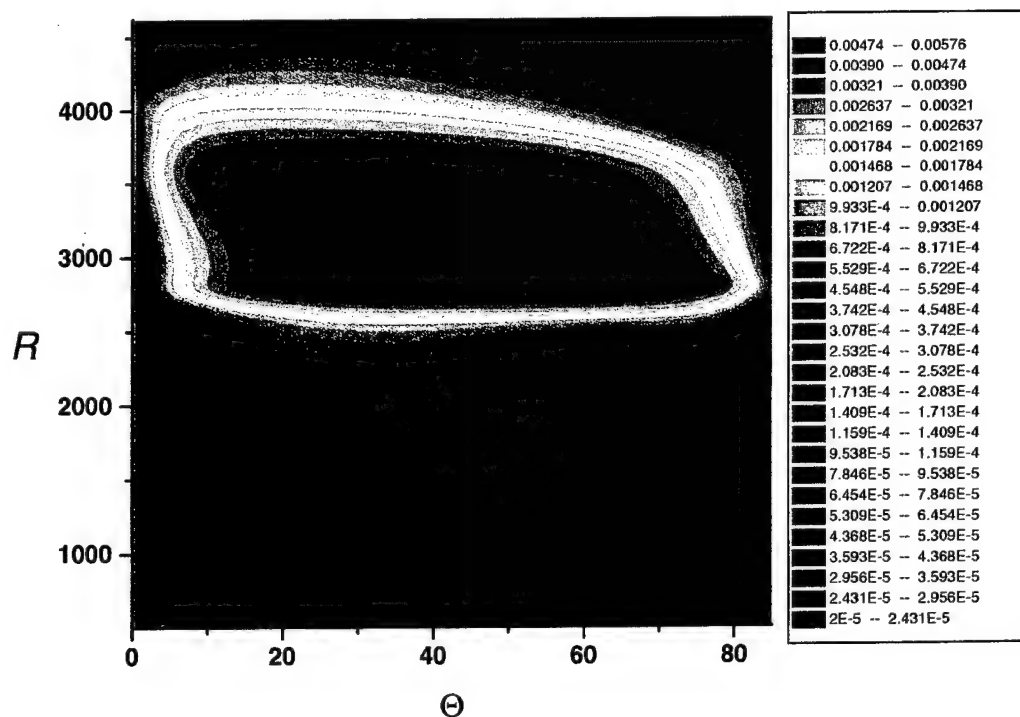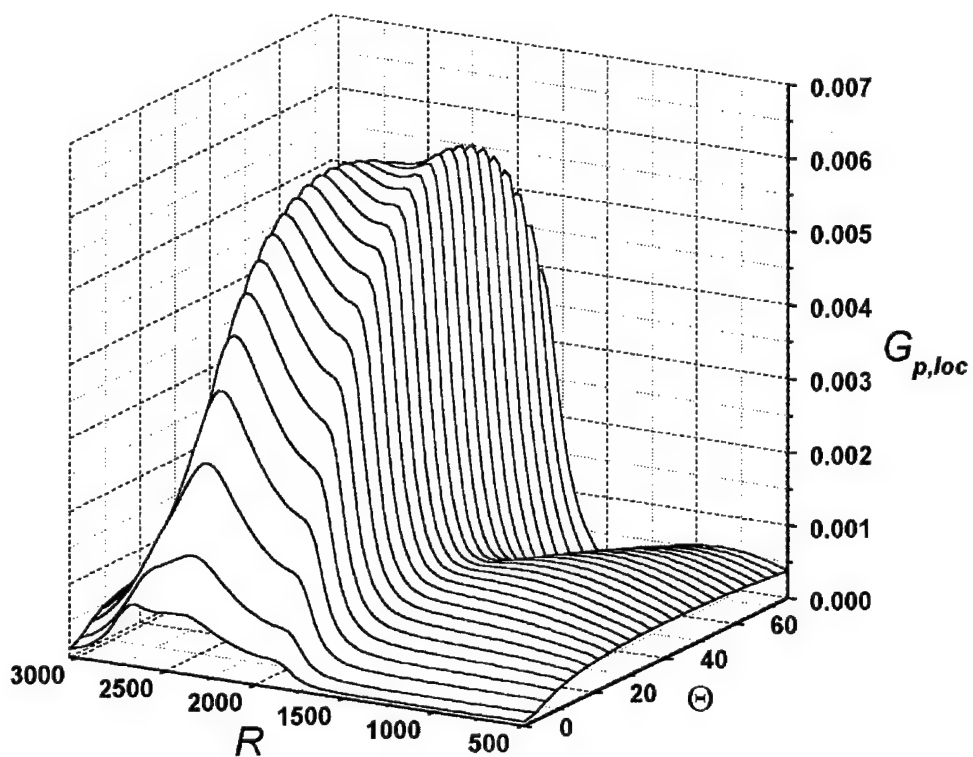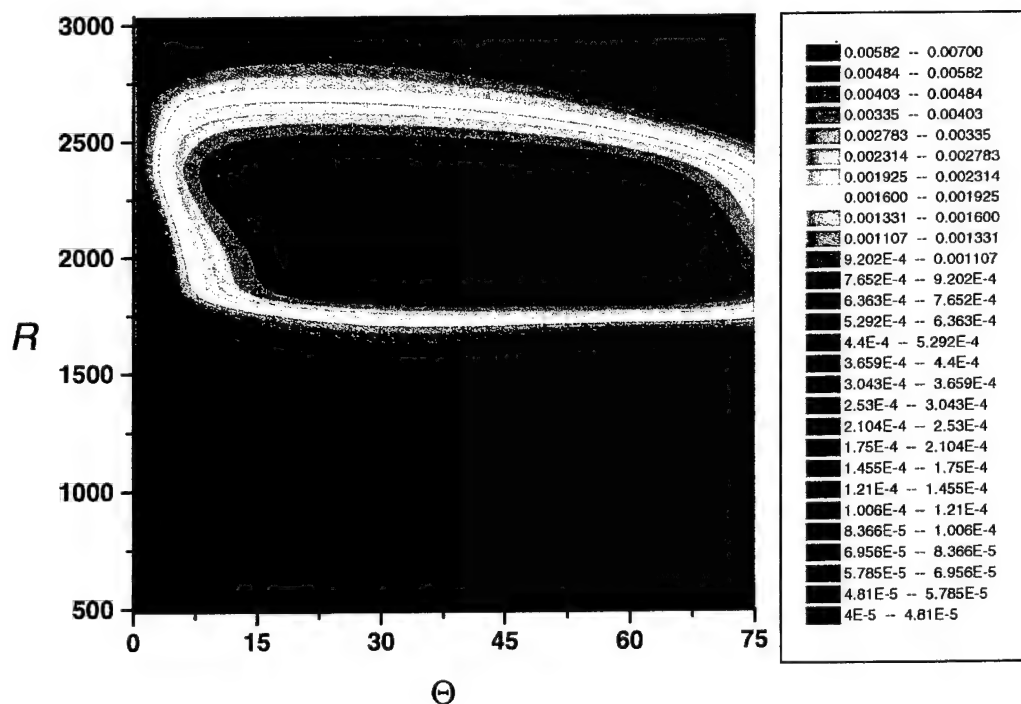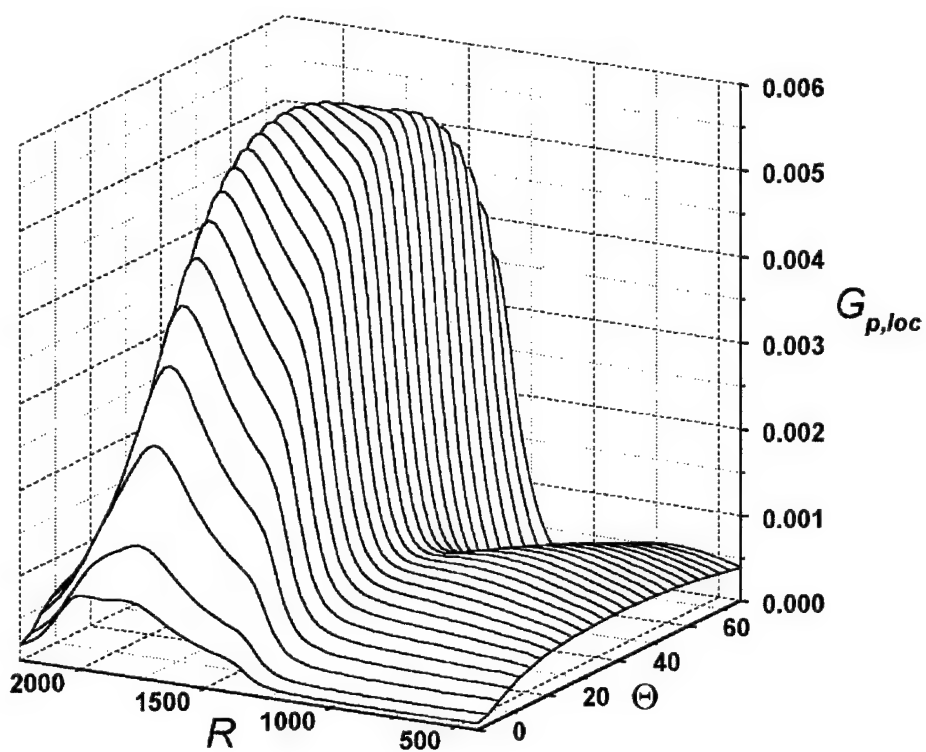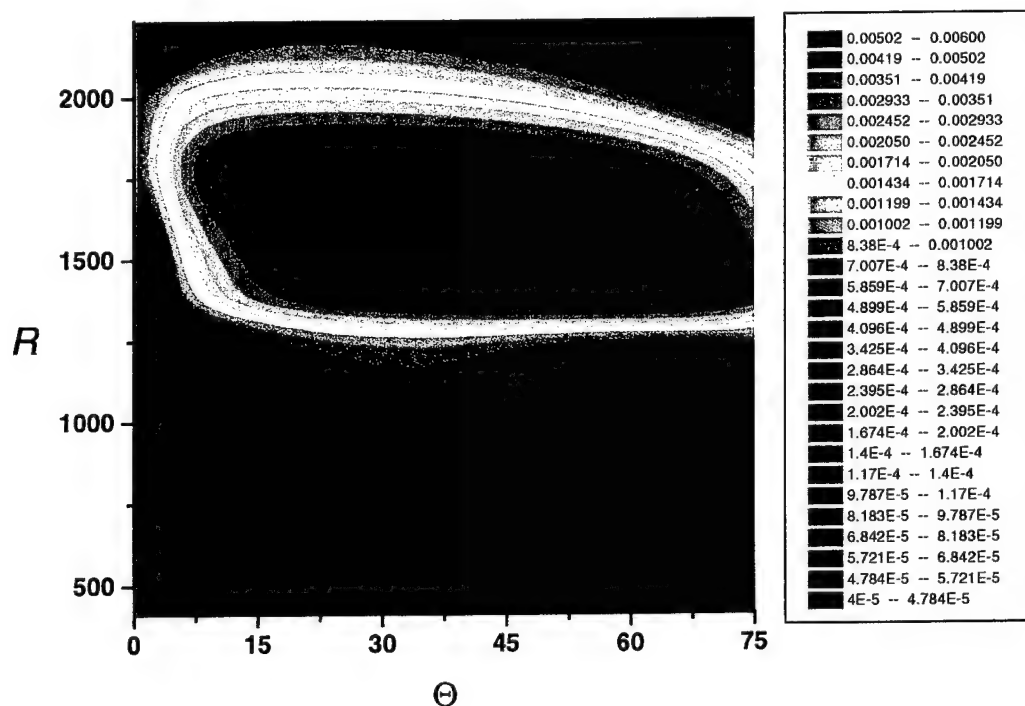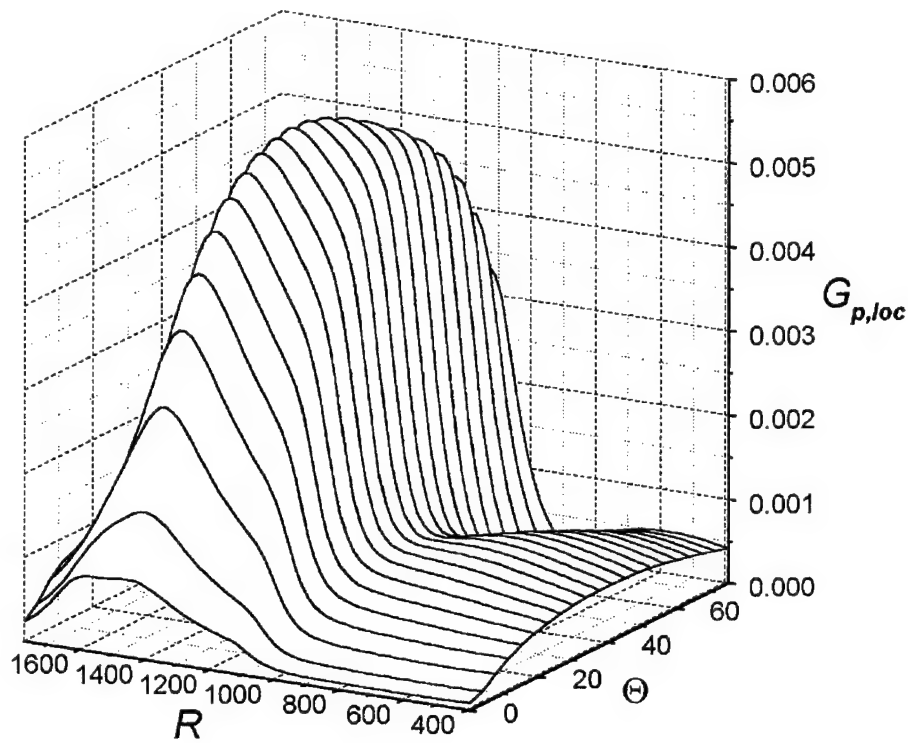Fig. 43a Local receptivity function for fast acoustic waves; $F = 10^{-4}$.

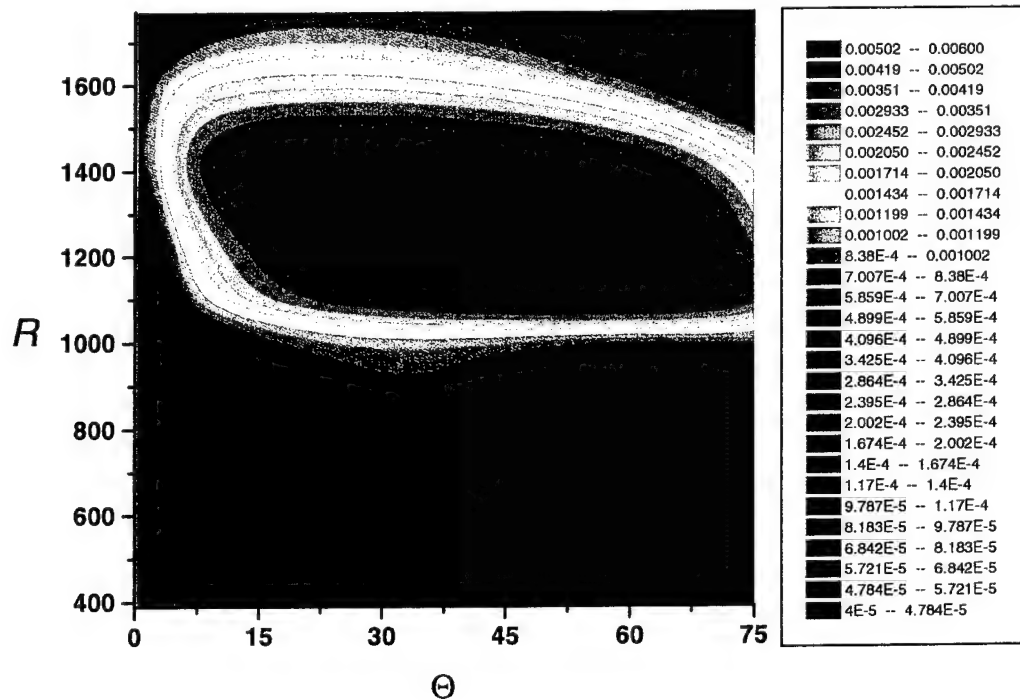|	
■	0.00502 -- 0.00600
■	0.00419 -- 0.00502
■	0.00351 -- 0.00419
▨	0.002933 -- 0.00351
▨	0.002452 -- 0.002933
▨	0.002050 -- 0.002452
▨	0.001714 -- 0.002050
□	0.001434 -- 0.001714
▨	0.001199 -- 0.001434
▨	0.001002 -- 0.001199
■	8.38E-4 -- 0.001002
■	7.007E-4 -- 8.38E-4
■	5.859E-4 -- 7.007E-4
■	4.899E-4 -- 5.859E-4
■	4.096E-4 -- 4.899E-4
■	3.425E-4 -- 4.096E-4
■	2.864E-4 -- 3.425E-4
■	2.395E-4 -- 2.864E-4
■	2.002E-4 -- 2.395E-4
■	1.674E-4 -- 2.002E-4
■	1.4E-4 -- 1.674E-4
■	1.17E-4 -- 1.4E-4
■	9.787E-5 -- 1.17E-4
■	8.183E-5 -- 9.787E-5
■	6.842E-5 -- 8.183E-5
■	5.721E-5 -- 6.842E-5
■	4.784E-5 -- 5.721E-5
■	4E-5 -- 4.784E-5

Fig. 43b Contours $G_{p,loc}(\Theta, R) = const$ for fast acoustic waves; $F = 10^{-4}$.

77

Appendix

Non-zero elements of Matrix $H_0 = (a_{jl})$, $j=1,...,8$, $l=1,...8$ in Eq. (2.9):

$$a_{12} = a_{56} = a_{78} = 1$$

$$a_{21} = \alpha^2 + \beta^2 + R\frac{i\Omega}{\mu T}$$

$$a_{22} = -\frac{D\mu}{\mu}$$

$$a_{23} = -i\alpha(m+1)\frac{DT}{T} - i\alpha\frac{D\mu}{\mu} + R\frac{DU}{\mu T}$$

$$a_{24} = R\frac{i\alpha}{\mu} - (m+1)\gamma M^2\alpha\Omega$$

$$a_{25} = \alpha(m+1)\frac{\Omega}{T} - \frac{D(\mu'DU)}{\mu}$$

$$a_{26} = -\frac{\mu'DU}{\mu}$$

$$a_{31} = -i\alpha$$

$$a_{33} = \frac{DT}{T}$$

$$a_{34} = -i\gamma M^2\Omega$$

$$a_{35} = i\frac{\Omega}{T}$$

$$a_{37} = -i\beta$$

$$a_{41} = -i\chi\alpha\left(r\frac{DT}{T} + 2\frac{D\mu}{\mu}\right)$$

$$a_{42} = -i\chi\alpha$$

$$a_{43} = \chi\left(-\alpha^2 - \beta^2 - R\frac{i\Omega}{\mu T} + r\frac{D^2T}{T} + r\frac{D\mu DT}{\mu T}\right)$$

$$a_{44} = -i\chi r\gamma M^2\left[\alpha DU + \beta DW + \Omega\left(\frac{DT}{T} + \frac{D\mu}{\mu}\right)\right]$$

$$a_{45} = i\chi\left[(\alpha DU + \beta DW)\left(\frac{r}{T} + \frac{\mu'}{\mu}\right) + r\frac{\Omega D\mu}{\mu T}\right]$$

$$a_{46} = i\chi r\frac{\Omega}{T}$$

$$a_{47} = -i\chi\beta\left(r\frac{DT}{T} + 2\frac{D\mu}{\mu}\right)$$

$$a_{48} = -i\chi\beta$$

$$a_{62} = -2(\gamma - 1)M^2 \Pr DU$$

$$a_{63} = -2i(\gamma - 1)M^2 \Pr(\alpha DU + \beta DW) + \Pr R \frac{DT}{\mu T}$$

$$a_{64} = -i(\gamma - 1)M^2 \Pr R \frac{\Omega}{\mu}$$

$$a_{65} = \alpha^2 + \beta^2 + i \Pr R \frac{\Omega}{\mu T} - (\gamma - 1)M^2 \Pr \mu' \frac{(DU)^2 + (DW)^2}{\mu} - \frac{D^2\mu}{\mu}$$

$$a_{66} = -2\frac{D\mu}{\mu}$$

$$a_{68} = -2(\gamma - 1)M^2 \Pr DW$$

$$a_{83} = -i\beta(m+1)\frac{DT}{T} - i\beta \frac{D\mu}{\mu} + R\frac{DW}{\mu T}$$

$$a_{84} = R\frac{i\beta}{\mu} - (m+1)\gamma M^2 \beta \Omega$$

$$a_{85} = \beta(m+1)\frac{\Omega}{T} - \frac{D(\mu' DW)}{\mu}$$

$$a_{86} = -\frac{\mu' DW}{\mu}$$

$$a_{87} = \alpha^2 + \beta^2 + R\frac{i\Omega}{\mu T}$$

$$a_{88} = -\frac{D\mu}{\mu}$$

Here

$$\mu' = \frac{d\mu}{dT}, \ DF = \frac{\partial F}{\partial y}, \ \Omega = \alpha U + \beta W - \omega, \ \chi = \frac{1}{\dfrac{R}{\mu} + ir\gamma M^2 \Omega};$$

$$r = \frac{2}{3}(k+2), \ m = \frac{2}{3}(k-1),$$

where $k = 0$ corresponds to Stokes hypothesis;
$U(x_1, y)$ and $W(x_1, y)$ is x and z-component of the laminar mean flow on a swept wing;
$T(x_1, y)$ is mean-flow temperature;
$\mu = \mu(T)$ is nondimensional dynamic viscosity, $D\mu = \mu' DT$.

Non-zero elements of the nonlinear interaction matrix

$G(y, x_1, \vec{q}; \alpha_w, \beta_w, \alpha_a, \beta_a, \omega) = (g_{jl})$, $j = 1, ..., 8$, $l = 1, ..., 8$, in Eq. (2.8a):

$$g_{21} = \frac{iR}{\mu T}[(\alpha_a + \alpha_w)q_1 + \beta_a q_7 + T\Omega_a \rho]$$

$$g_{22} = \frac{R}{\mu T} q_3$$

$$g_{23} = \frac{R}{\mu T}(q_2 + TDU\rho)$$

$$g_{24} = \gamma M^2 \frac{R}{\mu T}[i(\alpha_w U + \beta_w W)q_1 + DUq_3]$$

$$g_{25} = -\frac{R}{\mu T^2}[i(\alpha_w U + \beta_w W)q_1 + DUq_3]$$

$$g_{27} = i\beta_w \frac{R}{\mu T} q_1$$

$$g_{31} = -i\alpha_w T\rho$$

$$g_{33} = \frac{1}{T}\left(i\gamma M^2 \Omega_{aw} q_3 - \frac{DT}{T} q_5 + q_6\right)$$

$$g_{34} = i\gamma M^2(-\alpha_a q_1 - \beta_a q_7 + T\Omega_{aw}\rho)$$

$$g_{35} = \frac{i}{T}(\alpha_a q_1 + \beta_a q_7) - i\Omega_{aw}\rho - \frac{DT}{T^2} q_3$$

$$g_{36} = \frac{1}{T} q_3$$

$$g_{37} = -i\beta_w T\rho$$

$$g_{41} = i\frac{\alpha_a - \alpha_w}{T} q_3$$

$$g_{43} = -\frac{1}{T}\left\{i(\alpha_a - \alpha_w)q_1 + 2\frac{DT}{T} q_3 + i(\beta_a - \beta_w)q_7 + iT[(\alpha_a - \alpha_w)U + (\beta_a - \beta_w)W - \omega]\rho\right\}$$

$$g_{44} = \frac{i\gamma M^2}{T}[(\alpha_a - \alpha_w)U + (\beta_a - \beta_w)W - \omega]q_3$$

$$g_{45} = -\frac{i}{T^2}[(\alpha_a - \alpha_w)U + (\beta_a - \beta_w)W - \omega]q_3$$

$$g_{47} = \frac{i}{T}(\beta_a - \beta_w)q_3$$

$$g_{61} = i\alpha_w \Pr \frac{R}{\mu T}[q_5 - (\gamma - 1)M^2 Tq_4]$$

$$g_{63} = \Pr \frac{R}{\mu T}[q_6 + TDT\rho + i(\gamma - 1)M^2\Omega_{aw}q_3]$$

$$g_{64} = \Pr \frac{RM^2}{\mu T}\{\gamma[i(\alpha_w U + \beta_w W)q_5 + DTq_3] - i(\gamma - 1)T(\alpha_a q_1 + \beta_a q_7)\}$$

$$g_{65} = \Pr \frac{R}{\mu T}\left\{i\alpha_a q_1 + i\beta_a q_7 + iT\Omega_a\rho - \frac{1}{T}[i(\alpha_w U + \beta_w W)q_5 + DTq_3]\right\}$$

$$g_{66} = \Pr \frac{R}{\mu T}q_3$$

$$g_{67} = i\beta_w \Pr \frac{R}{\mu T}[q_5 - (\gamma - 1)M^2 Tq_4]$$

$$g_{81} = i\alpha_w \frac{R}{\mu T}q_7$$

$$g_{83} = \frac{R}{\mu T}(q_8 + TDW\rho)$$

$$g_{84} = \gamma M^2 \frac{R}{\mu T}[i(\alpha_w U + \beta_w W)q_7 + DWq_3]$$

$$g_{85} = -\frac{R}{\mu T^2}[i(\alpha_w U + \beta_w W)q_7 + DWq_3]$$

$$g_{87} = \frac{iR}{\mu T}[\alpha_a q_1 + (\beta_a + \beta_w)q_7 + T\Omega_a\rho]$$

$$g_{88} = \frac{R}{\mu T}q_3$$

Here $\vec{q} = \vec{F}_w(y)$ is vector-function of the wall-induced disturbance,

$$\Omega_a = \alpha_a U + \beta_a W - \omega, \quad \Omega_{aw} = (\alpha_a + \alpha_w)U + (\beta_a + \beta_w)W - \omega,$$

$$\rho = \frac{1}{T}\left(\gamma M^2 q_4 - \frac{1}{T}q_5\right) \text{ is density of the wall-induced disturbance.}$$